JAHRESBERICHT
2002

Laboratorium für Festkörperphysik
der
Eidgenössischen Technischen Hochschule
Zürich

VORWORT

The laboratory for solid state physics at ETH Zurich looks back at another successful year. Several research results from various groups have attracted international attention. It is a pleasure to thank all the scientists involved, who devoted their time and energy to fundamental research in solid state physics. Special thanks go to our technical and administrative stuff as well as the technical support provided by the physics department. These people managed to support the scientific projects through their expert help in spite of budget cuts and reduced resources within ETH Zurich. While technical support for research projects is presently still very good, being one of the trademarks of ETH Zurich, a further decline of the internal financial support could jeopardize this quality, which is so important for cutting edge science in condensed matter physics and is. On the scientific side, the financial support by the Schulleitung of ETH Zurich, the Schweizerischer Nationalfonds and other external sources is gratefully acknowledged.

We congratulate a former collaborator of our institute, Dr. Wolfgang Weber, for being chosen as a Professor by the University of Strasbourg.

The scientific staff of the laboratory for solid state physics is intensively involved in most teaching matters offered by the physics department. This encompasses beginners and advanced lectures for physics students as well as physics lectures for basically all other departments at ETH Zurich. In addition, lab courses are strongly supported and coached by members of the laboratory of solid state physics.

This yearly report appears in a new form. The mini CD is meant to offer a comfortable means to get access to the scientific projects and at the same time reduce the amount of paper distributed. We hope that it will serve its purpose and is well received by the community.

Zürich, im März 2002

Der Vorsteher

Klaus Ensslin

Prof. Dr. K. Ensslin

Contents

1 Physics of new materials **9**

1.1 Organic molecular crystals . . . 11

1.1.1 Growth, electrical transport and crystal structure of Tetracene and Pentacene single crystals . 11

1.1.2 Transport properties of field-induced charge in organic molecular crystals . . . 11

1.1.3 Symmetric-gate ambipolar field effect in an organic Mott Insulator . . . 12

1.1.4 Iodine intercalation in pentacene thin films . . . 12

1.1.5 Space-charge current with coplanar electrodes . . . 13

1.2 Silicon-germanium heterostructures . . . 13

1.2.1 SiGe modulation doped heterostructures . . . 13

1.2.2 Silicon-germanium nano-islands . . . 14

1.3 Superconducting magnesium-diboride and related compounds . . . 14

1.3.1 Crystal growth of MgB_2 and Mg-B-N phase diagram at high pressure . . . 14

1.3.2 Structural properties of MgB_2 . . . 15

1.3.3 Peak effect and disorder-induced phase transition in MgB_2 . . . 15

1.3.4 Librational modes in new magnesium nitridoboride . . . 16

1.4 Wide gap semiconductor GaN . . . 17

1.4.1 GaN high pressure crystal growth . . . 17

1.4.2 Al-doping and mixed crystals . . . 17

2 Optical and magneto-optical spectroscopy **19**

2.1 Magneto-optical study of the superconducting gap in MgB_2 single crystals . . . 21

2.2 Spectroscopic indications of polaronic carriers in quasi-one-dimensional conductors . . . 22

2.3 Charge dynamics of the Heusler alloy Fe_2TiSn . . . 24

3 Physics of mesoscopic structures, semiconductor nanostructures **25**

3.1 Kondo effect in quantum rings . . . 27

3.2 Bouncing states in quantum dots . . . 27

3.3 Stability of spin states in quantum dots . . . 29

3.4 Lateral superlattices on parabolic quantum wells . . . 29

3.5 Charging of ErAs islands in an AlGaAs heterostructure . . . 31

3.6 Low-temperature scanning gate experiments on semiconductor nanostructures . . . 32
3.7 Phase sensitive measurements on a four-terminal ring . . . 32
3.8 Topology of the nuclear pore complex . . . 33

4 Condensed matter at low temperatures 35
4.1 Physical properties of hexaborides . . . 37
4.1.1 ^{11}B-NMR studies of YbB_6 . . . 37
4.1.2 Pressure studies of CaB_6 and $Eu_{1-x}Ca_xB_6$ . . . 37
4.1.3 Electronic transport in EuB_6 and related hexaborides . . . 38
4.1.4 4f-5d Excitations in europium hexaboride . . . 39
4.1.5 Work function and surface relaxation in lanthanum hexaboride . . . 39
4.2 Superconductivity . . . 40
4.2.1 Anomalous low-temperature thermal conductivity of MgB_2 . . . 40
4.2.2 Temperature dependence of the upper critical field of type-II superconductors from isothermal magnetisation data . . . 41
4.3 Structural and physical properties of quasicrystals . . . 41
4.3.1 Structural phase transitions in decagonal Al-Co-Ni quasicrystals . . . 41
4.3.2 Inhomogeneous magnetism in decagonal $Al_{69.8}Pd_{12.1}Mn_{18.1}$ . . . 42
4.4 Physics of low-dimensional systems . . . 43
4.4.1 A low-dimensional spin $S = 1/2$ system at the quantum critical limit: $Na_2V_3O_7$ . . . 43
4.4.2 Universal behavior of spin-mediated energy transport in $S = 1/2$ chain cuprates . . . 44
4.5 Electron holography . . . 45
4.5.1 Electron holography investigations on gas-phase condensed Fe nanoparticles . . . 45
4.6 Morphologies of complex structures . . . 46
4.6.1 Morphologies . . . 46
4.6.2 Phase Field Simulations . . . 46
4.6.3 3D Reconstruction . . . 46
4.6.4 Dendrite Tip Velocity . . . 46
4.7 Application-oriented thin film research . . . 47
4.7.1 Epitaxial IV-VI narrow gap semiconductor layers for infrared devices . . . 47
4.7.2 Compound semiconductor thin film solar cells . . . 47

5 Magnetism, Electron Spectroscopy 51
5.1 Magnetism . . . 53
5.1.1 The stripe phase of ultrathin Fe films imaged with SEMPA . . . 53
5.1.2 The stripe phase of ultrathin Fe films imaged at Swiss Light Source . . . 53
5.1.3 XYZ-Fine Positioning and Scanning Stage for Photoemission Microscope . . . 53
5.2 Electron Spectroscopy . . . 54
5.2.1 Electronic excitations and lack of magnetic ordering in the icosahedral quasicrystal $Al_{70}Pd_{20}Mn_{10}$ 54

5.2.2 Debye temperature of the pentagonal surface of the icosahedral quasicrystal $Al_{70}Pd_{20}Mn_{10}$. 55
5.2.3 Structural transitions at the surface of the decagonal quasicrystal $Al_{70}Co_{15}Ni_{15}$ 55
5.2.4 Structure of Gd_2O_3 films on GaAs(100) and GaN(0001) 56

6 Publikationen **57**

7 Vorträge **65**

Chapter 1

Physics of new materials

Head
Prof. Dr. Bertram Batlogg

Academic Staff
Dr. Christoph Bergemann
Simon Haas
Markus Brühwiler
Claudia Goldmann
Kurt Pernstich

Technical Staff
Kurt Mattenberger
Hans Peter Staub

Academic Guests
Dr. Tatsuo Hasegawa, Hokkaido University, Japan
Dr. Jun-ichi Takeya, CRIEPI, Tokyo, Japan

Administrative Staff
Chiara Alexander
Gabriela Strahm

High pressure materials synthesis group

Head
Dr. Janusz Karpinski

Academic Staff
Dr. Sergei Kazakov
Jan Jun
Manuel Angst
Peter Geiser

Academic Guests
Dr. Andrej Mironov, Moscow State University
Dr. Roman Puzniak, Polish Academy of Sciences

Silicon heterostructures

Head
Dr. Hans von Känel

Academic Staff
Matthias Kummer
Benjamin Rössner

Academic Guests
Dr. Monica Bollani, University di Milano ”Bicocca”
Dr. Giovanni Isella, Politecnico di Milano
Armando Rastelli, Universita di Pavia

1.1 Organic molecular crystals

1.1.1 Growth, electrical transport and crystal structure of Tetracene and Pentacene single crystals

S. Haas, K. Mattenberger, H. P. Staub, B. Batlogg

Pentacene (Pc) and Tetracene (Tc) crystals are grown by vapor-phase transport. In order to get ultra-thin platelets as needed for the fabrication of FETs (for details see Goldmann et al.), the growing conditions have been optimized towards lower flow-rate and temperature. From analysis under the polarization microscope one can consider these crystals as highly single crystalline. Measurements of Tc-FET devices (see Fig.1.1) show a clear field effect, but a high threashold voltage (10 to 20 Volts).

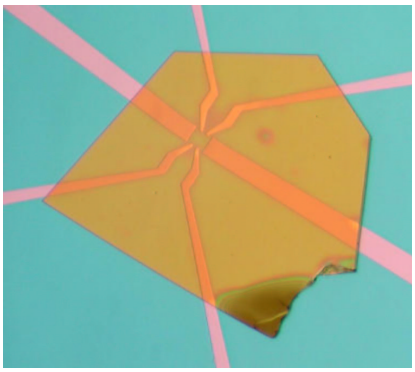

Figure 1.1: Tetracene crystal on pre-structured SiO_2. For details, see 1.1.2

Larger crystals are preferred to study bulk properties of Tc. To this end different growing conditions were explored. The key variables are: temperature, temperature gradient, transport gas and gas flow rate. Significant improvements in handling the delicate crystals results from using metal tips as artificial seeds, preventing the electrostatic charging of the crystals. The crystals are analyzed optically by photoluminescence spectroscopy and electrically by space-charge-limited-current (SCLC) measurements. Spatially resolved photoluminecence can reveal inhomogeneities on the micrometer-scale in the crystals. A critical sensitivity to Au contact deposition was noted in SCLC measurements and reproducibility could be enhanced. Hole mobilities in Tetracene reach 6×10^{-2} cm^2/Vs, and trap densities are in the order of $10^{14}/cm^{-3}$.

In collaboration with Theo Siegrist (Bell Labs), a phase transition in Pentacene was found at a temperature of about 380 K. The high temperature phase is monoclinic whereas the room temperature phase is triclinic. In the higher symmetry, the two Pc molecules within the unit cell are not independent anymore. This phase transition explains the degradation of the smooth surfaces of the freshly grown crystals during cooling to room temperature.

1.1.2 Transport properties of field-induced charge in organic molecular crystals

C. Goldmann, J. Takeya, B. Batlogg

in collaboration with Dr. B. Ketterer (PSI Villigen), the group of Prof. R. Kleiner (Univ. of Tübingen), and the group of Prof. K. Ensslin (ETH Zurich)

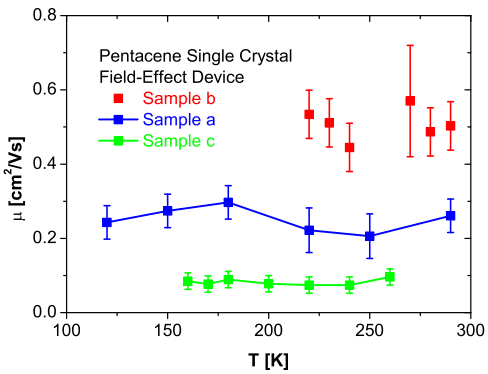

Figure 1.2: High temperature mobilities of three different Pentacene devices

The main problem of single crystal field-effect devices is damage to the crystal surface during the device fabrication. Therefore, we have developed a field-effect device which allows the attachment of the crystal onto prefabricated electrodes *at the end* of the fabrication process. The device consists of a thermally oxidized n^+-Si wafer (serving as gate plus insulator) on which Au electrodes are defined by means of electron beam lithography. Afterwards the surface is chemically treated to both reduce the influence of random charges in the dielectric and to improve the contact quality. Finally, a thin (2-5 μm) organic single crystal, grown by the vapor transport technique (described above), is placed on the substrate. With these devices we performed four-terminal measurements on Pentacene single-crystals in the temperature range of 30 - 290 K. Room-temperature mobilities were in the range of 0.1 to 0.5 cm^2/Vs and remained essentially unchanged down to approx. 150 K. The conductivity at a given gate voltage showed a crossover from a constant value at high temperatures to an activated behaviour at low temperatures (the latter is presumably due to shallow trapping).

1.1.3 Symmetric-gate ambipolar field effect in an organic Mott Insulator

T. Hasegawa, K. Mattenberger, J. Takeya, B. Batlogg

Field-effect doping was used to introduced charge into crystals of the quasi-one-dimensional Mott-Hubbard insulator (BEDT-TTF)(F2TCNQ). Vapor phase polymerization of organic diradicals (known as ”Parylene” coating) was utilized to deposit gate dielectric layers in the fabrication of field-effect device structures. The standard FET equations for unipolar devices were found to be inappropriate to describe the observed characteristics. Thus we derived and applied modified descriptions taking into account the symmetric-gate ambipolar FET structure. Fundamental features of the observed Mott insulator FET characteristics were well described in this model, though deviations become prominent at low temperatures, which can be ascribed to the interfacial potential effect.

1.1.4 Iodine intercalation in pentacene thin films

C. Bergemann, I. Schenker, K. Pernstich, A. Rashid, B. Batlogg

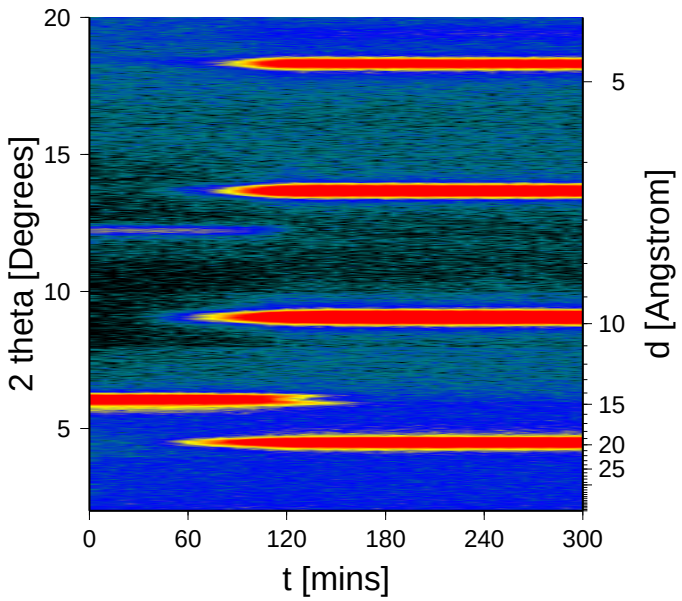

Figure 1.3: In situ X-ray diffraction on a pentacene thin film exposed to iodine vapour. The shift in peak position corresponds to a change of the c-axis layer spacing from 15.4 Å (pristine phase) to 19.4 Å (intercalated phase).

The biggest conceptual hurdle in addressing the transport properties of organic semiconductors is that it requires the measurement of “charge transport in the absence of charge”. One approach is to use bulk chemical doping of the crystal with intercalated charge donors, to control the band filling of the material in a series of (ideally) stoichiometric compounds.

We found that pentacene thin films are readily intercalated by iodine vapour. The electrical conductivity is drastically enhanced, with $\sim 0.1\,\mathrm{cm}^2/\mathrm{Vs}$ room temperature mobility and near-metallic low temperature behaviour. The intercalation process itself is also interesting from a structural point of view, since the intercalant markedly increases the interlayer spacing: Fig. 1.3 shows the results of an in situ X-ray diffraction experiment on a 50 nm thick pentacene thin film, evacuated to 2×10^{-4} mbars and then exposed to iodine vapour at room temperature. Over time, the peaks corresponding to the pristine phase disappear, and the intercalated phase becomes visible. At the transition, details of the peak structure reveal the elastic properties of the crystal structure of pentacene.

1.1.5 Space-charge current with coplanar electrodes

C. Bergemann

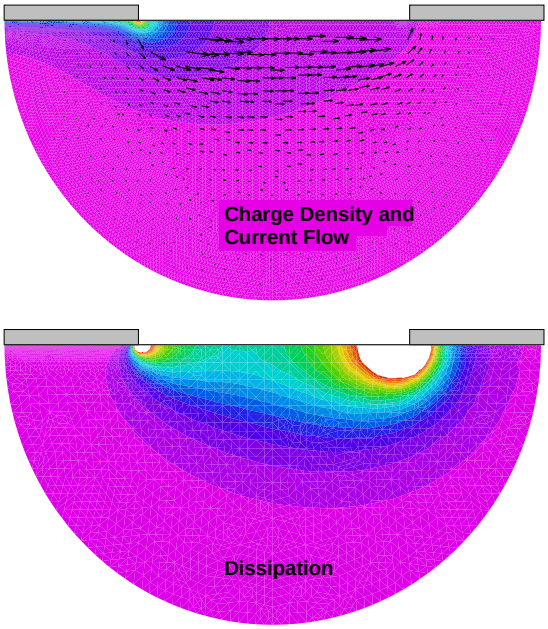

Figure 1.4: Space charge density, current flow, and dissipation in the coplanar geometry.

The current-voltage characteristics of organic semiconductors do not follow Ohm's law - instead, the current is controlled by the voltage-induced space charge, leading to a current response proportional to V^2, and to the carrier mobility. Measurement of the current-voltage characteristics has been used extensively for the determination of out-of-plane mobilities in thin films and flat samples; recently, attempts ahve been made to extend this technique to the measurement of the in-plane mobility, with coplanar contacts on top of the sample.

We have theoretically analysed the current distribution arising from an applied voltage in this new coplane geometry. The response to the voltage is governed by a non-linear, third order partial differential equation which we solved using finite element methods. Fig. 1.4 shows the charge density (in units of $\epsilon_r \epsilon_0 V/a^2$) and the current in the first panel, and the resulting dissipation (in units of $\mu \epsilon_r \epsilon_0 V^3/a^4$) in the second, where a is the contact separation. Our main result is that the dissipation diverges rapidly in the vicinity of both the charge-inducing and the charge-collecting contact, leading to sample damage often before the intrinsic mobility can be assessed.

1.2 Silicon-germanium heterostructures

1.2.1 SiGe modulation doped heterostructures

B. Rössner, H. von Känel, G. Isella, M. Kummer, E. Müller

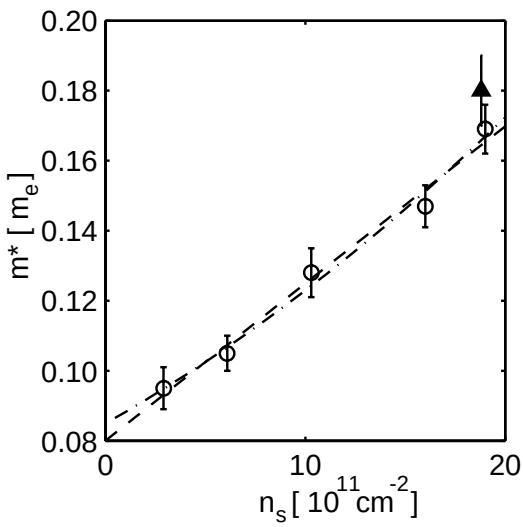

Figure 1.5: Effective mass of pure Ge channel p-MODs on a $Si_{0.3}Ge_{0.7}$ substrate. The mass increases with carrier density. Circles: single side doped, Triangle: double side doped

The growth of SiGe heterostructures with a pure Ge channel suffers from the need to combine high growth rate for buffer deposition and near monolayer precision for the electrically active structure. Usually a two-step technique is needed. The LEPECVD process which is especially suitable for growth of graded buffers was adapted to accomodate the precision requirements. P–Modulation Doped (p-MOD) heterostructures were grown without growth interruption using the LEPECVD process. The highest hole mobility achieved was 90.000 cm^2/Vs at 4.2 K. It set a new record for SiGe heterostructures.

The dispersion relation of the carriers in the Ge channel is especially interesting since it is influenced by strain, confinement and the close proximity of other bands, which leads to strong nonparabolicity. The effective hole mass as function of carrier density was investigated using temperature dependence of Shubnikov–de Haas oscillations. Figure 1.5 shows this relation. The results compare favourably with an analytic model, taking into account the effects of strain and band mixing due to the presence of a heterostructure. The mixing turns out to be energy dependent and thus gives rise to the nonparabolicity, since the different bands have different effective masses.

1.2.2 Silicon-germanium nano-islands

A. Rastelli, H. von Känel, M. Kummer

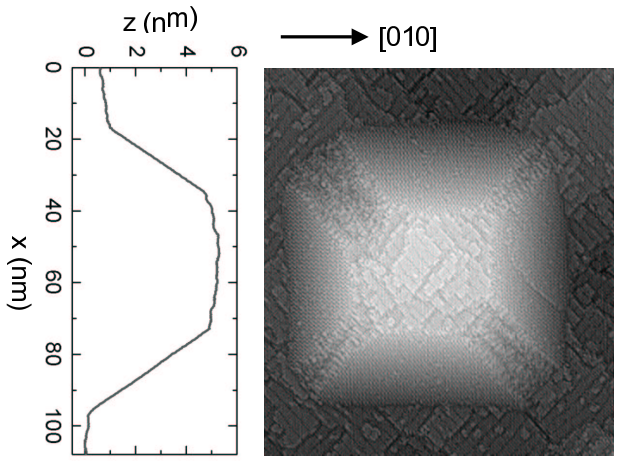

Figure 1.6: STM image of a T-pyramid (obtained by depositing $Si_{0.6}Ge_{0.4}$ on Si(001) at a substrate temperature of 600°C) and corresponding cross section, from an average of 30 line scans taken from left to right close to the middle of the island.

SiGe nanostructures were grown on Si(001) substrate by magnetron sputter epitaxy (MSE) and investigated by *in situ* scanning tunneling microscopy (STM). Three-dimensional islands form spontaneously during epitaxial growth as a way of relieving the elastic energy due to the lattice mismatch between the SiGe epilayer and the substrate (Stranski–Krastanow growth mode). This growth mode is commonly observed also for several compound semiconductor systems and is attracting much interest for potential application in nano- and opto-electronics, since it is a simple way to produce defect-free objects of nanometric size.

The mechanisms of island formation and evolution are still under debate. Their comprehension is important for obtaining structures with predictable properties. A recent model predicted that islands form as shallow unfacetted mounds (named prepyramids) and then undergo a morphological transition to partially $\{105\}$ facetted truncated pyramids with a rounded top (T-pyramids). In order to verify these predictions, SiGe layers with various thickness and composition were grown by MSE and studied at high resolution by STM. A statistical analysis of island shapes revealed that islands appear as prepyramids and that they transform into T-pyramids as their size increases beyond a critical value. Figure 1.9 shows that T-pyramids are bounded by $\{105\}$ facets and have a rounded top, in agreement with the model. The shallow top shrinks as the island size increases, so that large islands form in fully developed pyramids.

1.3 Superconducting magnesium-diboride and related compounds

1.3.1 Crystal growth of MgB_2 and Mg-B-N phase diagram at high pressure

J. Jun, S. Kazakov, J. Karpinski

MgB_2 recently attracted a lot of interest due to the anisotropic two-band electronic structure, leading to the presence of two distinct energy gaps. This causes unconventional properties, like the high critical temperature of 39 K and a temperature and field dependent anisotropy, which does not fit to the Ginsburg-Landau model with a constant anisotropy of the upper critical field. Anisotropic properties have to be studied on single crystals. We have grown MgB_2 single crystals at high pressure. In order to determine the conditions of crystal growth, a basic knowledge of phase relationship is necessary. The crystal growth process of MgB_2 is not a simple growth from a solution in molten magnesium. MgB_2 crystals are the products of a reaction in the ternary system Mg-B-N, where BN is a source of N:

$$4Mg + 8B + BN \rightarrow MgNB_9 + 3Mg \rightarrow$$
$$MgB_2 + BN + 6B + 3Mg \rightarrow 4MgB_2 + BN$$

The relatively large size and good quality of the single crystals allowed for detailed investigations of the intrinsic properties of MgB_2 with various methods. In the course of this work a new ternary nitride, $MgNB_9$ has been synthesized.

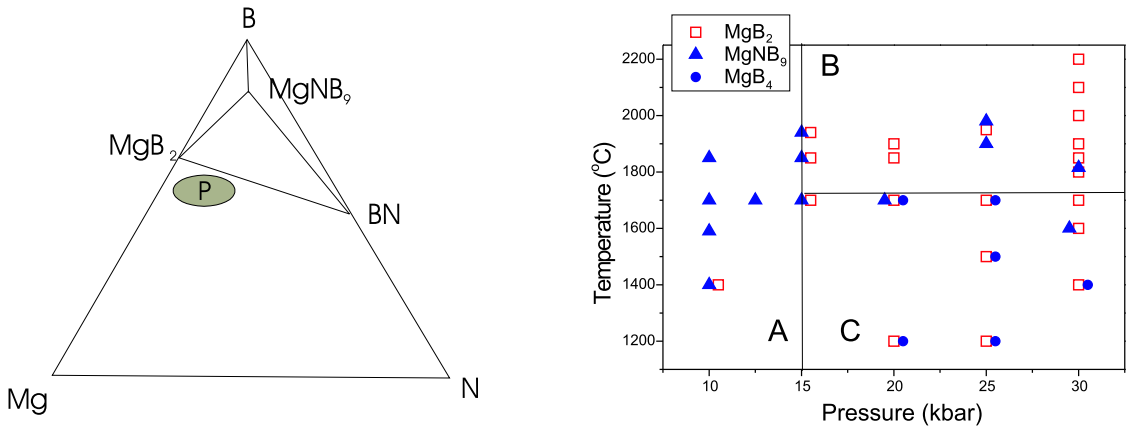

Figure 1.7: a) Ternary Mg-B-N system with compounds involved in the crystal growth of MgB_2. Field P corresponds to the composition of precursor used for crystal growth. b) P-T phase diagram of Mg-B-N system for a composition with excess Mg (Mg:B=1:1.2). Symbols show phases observed in the samples. MgB_2 single crystals have been grown in the region B.

1.3.2 Structural properties of MgB_2

S. Kazakov, J. Karpinski

in a collaboration with P. Bordet, CNRS Grenoble

The structure of several crystals has been investigated with an X-ray (Nonius Kappa CCD) diffractometer. The crystals had the form of platelets with dimensions between $0.12 \times 0.12 \times 0.03\,\mathrm{mm}^3$ and $0.4 \times 0.4 \times 0.06\,\mathrm{mm}^3$. The superconducting transition temperature of crystals from four different batches varied from $34.4\,\mathrm{K}$ to $38.8\,\mathrm{K}$. In all cases the R and R_w agreement factors were between 1.5 and $2\,\%$ indicating the good quality of refinement of the structural parameters. Unexpectedly, the structural parameters obtained for the four samples were all equal within two standard deviations. Their values are: $a = 3.085(1)\,\text{Å}$, $c = 3.518(2)\,\text{Å}$, anisotropic displacement parameters: U_{11}(Mg)$= 0.0045(1)\,\text{Å}^2$, U_{33}(Mg)$= 0.0048(2)\,\text{Å}^2$, U_{11}(B)$= 0.0034(2)\,\text{Å}^2$ and U_{33}(B)$= 0.0044(2)\,\text{Å}^2$. This agreement between structural data of the crystals from different batches indicates that the changes of T_c observed between crystals grown in different conditions cannot be attributed to detectable structural modifications. Refining the B atom occupancy lead to values equal to 1.00(1). However, we note that a minor substitution of boron by carbon or nitrogen from the heater or crucible would be almost impossible to detect with x-ray diffraction, because of the small contrast between these elements, and therefore cannot be excluded here. Electron energy loss spectroscopy and energy dispersive x-ray measurements did not show such impurities, therefore the differences in T_c have to be attributed to not yet defined defects or impurities.

1.3.3 Peak effect and disorder-induced phase transition in MgB_2

M. Angst, J. Karpinski

in a collaboration with R. Puzniak and A. Wisniewski, Institute of Physics PAS Warsaw

After investigating the anisotropic reversible properties of the superconducting state of MgB_2 single crystals, we used torque magnetometry to study their irreversible properties. Measurements of the torque as a function of the applied field revealed a sharp peak in the irreversible torque, located at about $0.85\,H_{c2}$ (see inset of Fig. 1.8). In other superconductors, for example $NbSe_2$, a similar peak effect was shown to be the signature of a disorder-driven phase transition out of the “Bragg glass” with it’s almost perfectly ordered vortex lattice into a highly disordered, amorphous

phase. In the vicinity of this transition, pronounced history dependencies of the critical current density are expected and were observed.

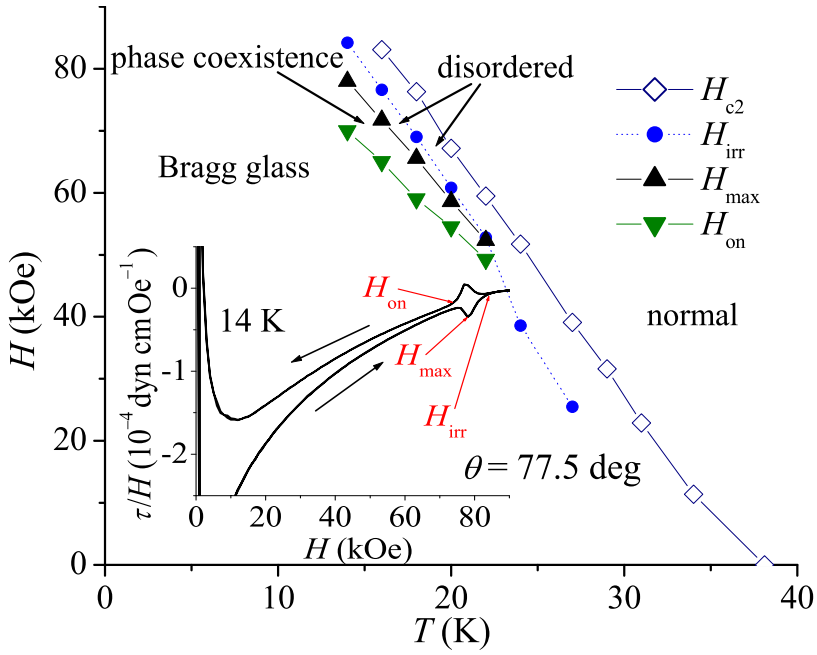

Figure 1.8: Phase diagram of MgB_2 single crystal at an angle of $77.5\,\mathrm{deg}$ between the c-axis of the crystal and the applied field: The temperature dependence of the characteristic fields H_{c2}, $H_{\max}$, and H_{on} is given. They mark boundaries between the normal state and the various phases of vortex matter. The irreversibility field H_{irr} is also shown. The inset shows an example torque τ/H vs H curve, measured at $14\,\mathrm{K}$ and $77.5\,\mathrm{deg}$.

In order to detect history effects in MgB_2, a study with "minor hysteresis loops" was performed. Pronounced variations of the (minor loop) hysteresis widths depending on starting conditions were indeed observed. The effects are compatible with and strongly indicative of the peak effect signifying the order-disorder transition in MgB_2.

The angular dependence of the transition field is similar to the $H_{c2}(\theta)$ dependence, whereas the evolution of the peak amplitude is more complicated. The resulting field-temperature phase diagram is presented, for an angle of $77.5\,\mathrm{deg}$ between the field and the c axis of the crystal, in the main panel of Fig. 1.8. In low fields, below the peak onset, the vortices are in the Bragg glass phase, whereas between the peak maximum and H_{c2} they are disordered. In the region between peak onset and maximum, the observed history effects indicate a coexistence of the Bragg glass and the disordered phase. The position of these features in the $H - T$ plane is not dissimilar to the case of $NbSe_2$. However, it is important to note that thermal fluctuations are much more important in MgB_2 – this (together with the lower sensitivity of the torque magnetometer in lower fields) is also the reason for the apparent end of onset and maximum lines at $22\,\mathrm{K}$. The increased importance of thermal fluctuations above this temperature is also indicated by the irreversibility line (where the two branches of the torque measured in increasing and decreasing field meet). Due to the increased thermal fluctuations, which are intermediate between conventional and cuprate superconductors, MgB_2 may be a good candidate for the observation of vortex lattice melting driven by thermal fluctuations in a non-cuprate superconductor.

1.3.4 Librational modes in new magnesium nitridoboride $MgNB_9$

M. Brühwiler, B. Batlogg, J. Jun, S. Kazakov, J. Karpinsky

Boron and its compounds are chemically and physically exciting materials. Notably boron carbide and boron nitride are widely used because of their outstanding properties, being either of mechanical, thermal, or physical nature. Boron has been used to form new types of alloys, particularly with aluminum and titanium. Furthermore, the discovery of

superconductivity in MgB_2 below $38\,\mathrm{K}$ has stimulated detailed studies of this particular boride. In the process of growing MgB_2 single crystals, a new compound $\mathrm{MgNB_9}$ was discovered and we investigated its electrical and thermal properties.

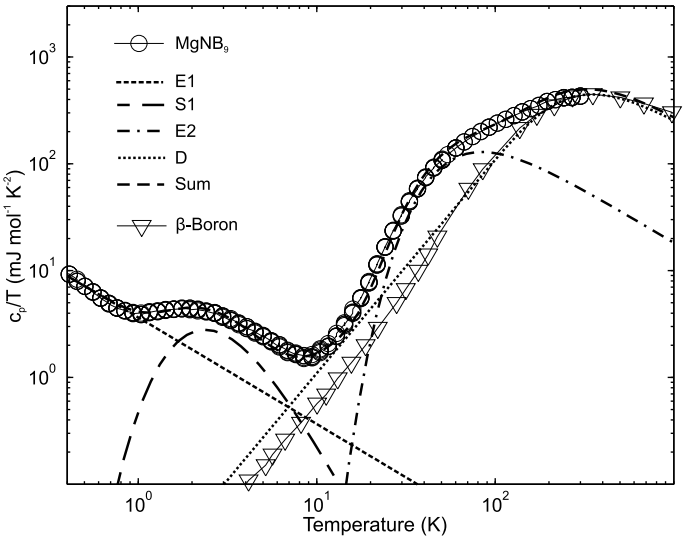

Figure 1.9: Temperature dependence of c_p/T. Shown are our data for $\mathrm{MgNB_9}$ and literature values for β-boron for comparison. The data are well described by the sum of two low-temperature modes (E1 and S1), a librational Einstein mode at $150\,\mathrm{cm}^{-1}$ (E2), and a Debye background (D) with $\Theta_\mathrm{D} = 1250\,\mathrm{K}$.

Electrical resistivity measurements indicate that $\mathrm{MgNB_9}$ is a semiconductor with an activation energy of approximately $150\,\mathrm{meV}$. The compound is composed of structural building blocks that are characteristic for various modifications of boron, and borides in general. It consists of B_6 octahedra connecting two layers of B_{12} icosahedra. Within the layer, the icosahedra are furthermore joined through the N atoms, each of which is bonded to three B_{12} units. A similar network, but consisting of B_{12} icosahedra only, constitutes elementary α-boron.

It has been shown by classical valence-force-field calculations that librational modes due to the inter-icosahedral bonding of such B_{12} cages exist in elementary α-rhombohedral boron. However, such librations are not easily measured by Raman spectroscopy, because of the small associated polarization. In specific heat measurements, on the other hand, such low-frequency, librational modes should be observable, since the Debye background lies at sufficiently high energies to uncover the signal.

We have measured the specific heat c_p of $\mathrm{MgNB_9}$ from $0.4\,\mathrm{K}$ to $300\,\mathrm{K}$ using an adiabatic relaxation technique. The data can be modeled by a sum of four contributions: A Debye part with $\Theta_\mathrm{D} = 1250\,\mathrm{K}$ dominates at highest temperatures, followed by a pronounced shoulder near $50\,\mathrm{K}$. This shoulder stems from an Einstein mode with $\lambda_\mathrm{E}^{-1} = 150\,\mathrm{cm}^{-1}$ $(4.5\,\mathrm{THz})$ and is attributed to librations of the connected B_{12} icosahedral clusters analogous to α-rhombohedral boron. The density of modes amounts to 0.4 modes per $2{\cdot}\mathrm{MgNB_9}$. The anomalous increase of c_p below about $20\,\mathrm{K}$ is ascribed to low frequency defect modes. One of them is modeled by a Schottky anomaly with $n = 3.8 \times 10^{-4}$ modes per $2{\cdot}\mathrm{MgNB_9}$ and $\nu_\mathrm{E} = 160\,\mathrm{GHz}$. The mode at lowest frequency is modeled by an Einstein oscillator with a density of $n = 8 \times 10^{-5}$ modes per $2{\cdot}\mathrm{MgNB_9}$. The characteristic Einstein frequency of this contribution cannot be determined from our data but lies below approximately $10\,\mathrm{GHz}$. In comparison to elementary boron and other boron compounds, the cluster librations in $\mathrm{MgNB_9}$ are most clearly detected, indicating the distinct nature of the B_{12} cluster unit in this structure.

1.4 Wide gap semiconductor GaN

P. Geiser, J. Jun, J. Karpinsky

1.4.1 GaN high pressure crystal growth

Through continuous optimization of the high nitrogen pressure solution growth (HNPSG) process the size of the GaN crystals could be increased to $3 \times 5\,\mathrm{mm}^2$ which represents a technical limit given by the volume of the high pressure chamber. A larger chamber is under construction.

1.4.2 Al-doping and mixed crystals

We succeeded in growing Aluminum doped GaN by using temperature gradients that are an order of magnitude larger than for standard growth (up to $80\,^\circ\mathrm{C}$). From comparative Laser Ablation - Inductive Charged Plasma - Mass

Spectroscopy (LA-ICP-MS) measurements the amount of incorporated Al is found to be higher than in undoped crystals. The total amount however, is comparably small as one can deduce from photoluminescence measurements showing a blueshift of a few meV at ambient temperatures.

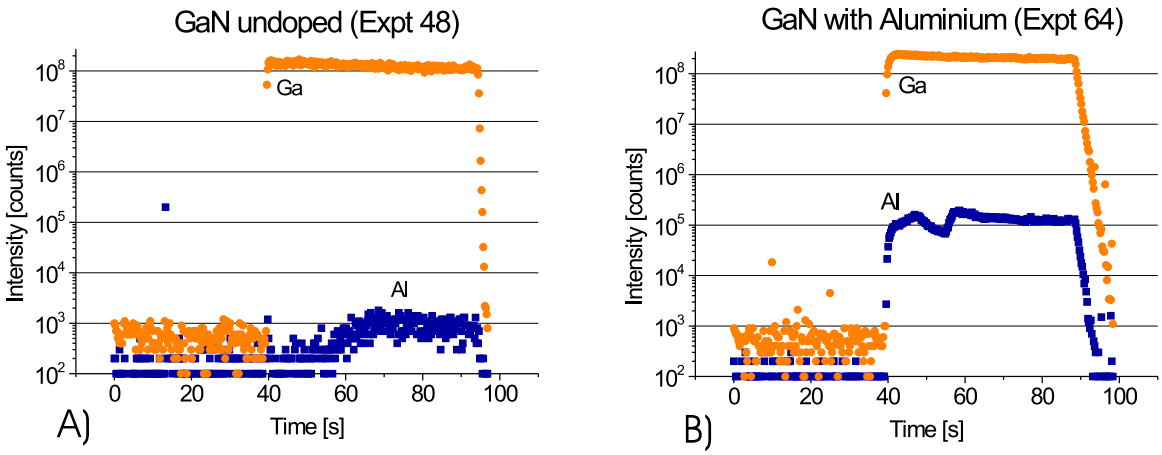

Figure 1.10: A) LA-ICP-MS intensity signal measured on a undoped GaN crystal. Only a trace amount of Al is found. B) LA-ICP-MS measurement on Al-doped GaN crystal. An increase of signal intensity of 2 orders of magnitude is found. The crystal shows some zonation over the depth profile.

Recently GaN has been reported to be a host for magnetic ions, transforming this material into a magnetic semiconductor of interest for spintronics. We have grown crystals with the intention to incorporate Gd and Mn. Under the conditions employed in our growth procedure, the amount of Gd and Mn substitution turned out to be very small: no traces of ferromagnetism could be detected, and only small concentrations of paramagnetic moments are present.

Chapter 2

Optical and magneto-optical spectroscopy

Head
Prof. Dr. L. Degiorgi

Academic Staff
S. Broderick G. Caimi A. Perucchi

Technical Staff
J. Müller

Academic Guests

Administrative Staff
I. Heer

2.1 Magneto-optical study of the superconducting gap in MgB_2 single crystals

A. Perucchi, L. Degiorgi, J. Jun, M. Angst and J. Karpinski

Since the discovery of superconductivity in MgB_2 with $T_c \sim 40\ K$, substantial experimental activity has been devoted to elucidate the nature of its superconducting state. The issue is to assess whether MgB_2 is one of the best-optimized Bardeen-Cooper-Schrieffer (BCS) materials or whether its superconducting properties stem from a novel pairing mechanism. The amplitude of the superconducting gap and its spectroscopic signature, as a function of temperature and magnetic field, are expected to depend on the driving mechanism.

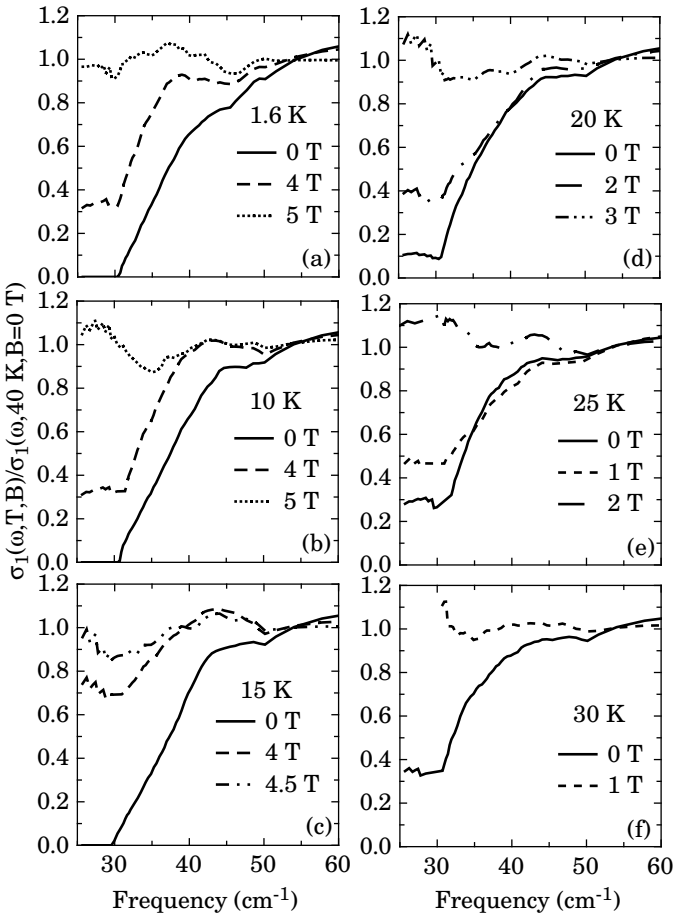

Figure 2.1: Magnetic field dependence ($H \parallel c$) of the conductivity ratio σ_{1s}/σ_{1n} at selected temperatures in the FIR spectral range. The normal state σ_{1n} corresponds to the measurement at $40\ K$ in zero field.

Infrared spectroscopy is a very promising and powerful method for the observation of the gap. Optical experiments, besides being contact-less techniques, offer the important advantage that the electromagnetic radiation penetrates deeply inside the bulk. We have presented infrared reflectivity data $R(\omega)$ on high quality *single* crystals of MgB_2 with well-characterized optical surfaces parallel to the basal-plane. The data were collected as a function of temperature ($1.5 - 300\ K$) and with varying magnetic field H ($0 - 7\ T$, in steps of 0.5 and 1 T) oriented along the c-axis with possible misalignment of less than 5^0. The corresponding real part $\sigma_1(\omega)$ of the optical conductivity is obtained through Kramers-Kronig transformation.

Figure 1 shows the magnetic field dependence of the ratio between the real part $\sigma_1(\omega)$ of the optical conductivity and its normal state value (at $40\ K$) at selected temperatures. Focusing first on the $0\ T$ data, we observe the strong depletion of $\sigma_1(\omega)$ for $T < T_c$. The conductivity is very small or even zero (i.e., as a consequence of the total reflection for $T \ll T_c$) below $30\ cm^{-1}$ and then increases monotonically at higher photon energies. We identify the frequency, where the onset of absorption (i.e., increase of $\sigma_1(\omega)$, Fig. 1) occurs, as the superconducting gap value. The resulting gap-ratio $2\Delta/k_BT_c \sim 1.2$ seems to confirm the trend of an optical superconducting gap in MgB_2 substantially below the estimate of the weak-coupling BCS theory. Another key aspect of this study is the possibility to exploit bulk sensitive and contact-less optical data in order to extract the upper critical field H_{c2} along the c-axis. The fields for which the normal state is recovered (i.e., the conductivity in Fig. 1 yields a ratio close to one) represent the optical counterpart of H_{c2} along the c-axis. These characteristic fields are shown in Fig. 2. While the temperature-grid considered here does not allow any conclusion about possible anomalous curvature of $H_{c2}(T)$ (particularly close to T_c), it is safe to say that our values of H_{c2} are compatible with the temperature dependence derived by Helfand and Werthamer (Fig. 2). It remains to be seen how one can reconcile an overall BCS-like H_{c2} with less conventional manifestations of the superconducting state, like the small gap value.

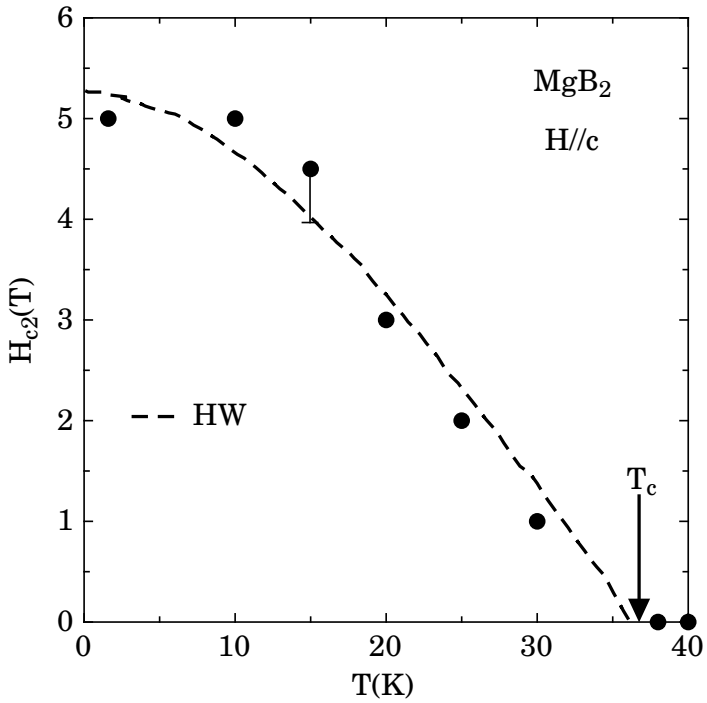

Figure 2.2: Temperature dependence of H_{c2} along the c-axis, evaluated from the optical experiment. The thick dashed line is compatible with calculations due to Helfand and Werthamer (HW).

2.2 Spectroscopic indications of polaronic carriers in quasi-one-dimensional conductors

L. Degiorgi, M. Grioni and L. Forro

The low-energy properties of a solid are determined by its elementary excitations. They can broadly be classified into quasiparticles, evolving continuously out of electrons when interactions are turned on, and collective modes, with no counterparts in non-interacting electron systems. Spectroscopic investigations are required for their accurate characterization. There are entire classes of materials whose spectroscopic results are poorly understood, like the cuprates and generally all quasi-one-dimensional (1D) materials. Despite the diversity in the physical properties of 1D materials, there are common features in the spectroscopic results, which clearly and consistently indicate deviations from the Fermi liquid scenario. The ARPES data have shown the absence of clear-cut Fermi surface crossings in the normal state and rather large gaps in the insulating phase of 1D systems characterized by a broken-symmetry ground state. Optical data are indicative of the important role played by the fluctuation effects with the opening of a pseudogap and a para-conductivity contribution and quasi-pinned mode in the normal state. It is believed that strong electron-electron or electron-phonon interactions are responsible for these unusual results.

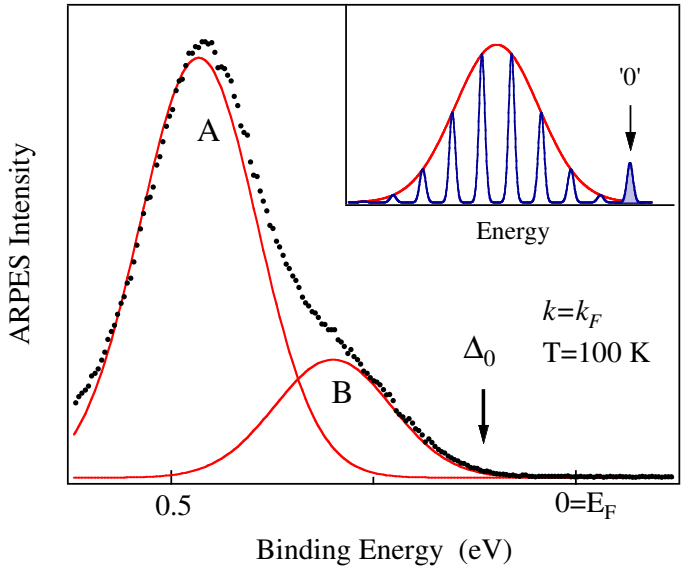

Figure 2.3: High resolution ARPES spectrum of $(TaSe_4)_2I$ at 100 K and $k = k_F$. Two Gaussian lines can fit the line shape. The extrapolation of the leading edge defines an energy gap of 0.12 eV. Inset: schematic spectral function of an electron coupled to a harmonic oscillator in the strong-coupling limit.

We have presented and discussed new ARPES and optical data on prototype 1D charge-density-wave (CDW) materials, like $(TaSe_4)_2I$ and $K_{0.3}MoO_3$. Figure 3 shows the ARPES spectrum measured at k_F and 100 K in the CDW phase of $(TaSe_4)_2I$, where the features are sharper. A similar study on $K_{0.3}MoO_3$ leads to comparable results. The line is almost independent of wave vector. It exhibits a main peak (A), and a distinct shoulder (B) at 0.3 eV. An excellent fit of the spectrum is achieved with two Gaussian lines with identical width. The weaker feature B has a maximum at $k = k_F$. They represent the parallel bands formed by bonding and anti-bonding combinations of 1D states on adjacent chains. Furthermore, we do observe signature of Fermi surface crossings in ARPES, but with exceedingly small intensity. Most of the spectral weight goes into an incoherent high-energy feature, which is shifted from band dispersion (Fig. 3). Within a scenario where the electron-phonon interaction clearly dominates, these observations are consistent with the formation of a polaron liquid, with masses $m^* \sim 10m_e$ derived from spectral weight analysis of the optical conductivity. Figure 4 shows indeed the optical conductivity, which has complex structure. Besides the peaks from a quasi-pinned collective mode and the CDW (pseudo)-gap, one can identify two distinct zero-frequency modes. They represent the collective contribution of sliding CDW segments, and the Drude response of uncondensed quasiparticles defining the Fermi surface, respectively. The spectral weight of the quasiparticles Drude term can be scaled with the total spectral weight up to the onset of the interband transitions, leading to the large effective mass of the polaronic quasiparticles. This suggests that the quasiparticles are heavily renormalized by strong electron-phonon interactions. At low temperature, the polaronic quasiparticles undergo a transition to a charge-density-wave state. The formation of heavy polarons with short coherence length seems to be a generic feature of 1D Peierls systems, a hypothesis which calls for an experimental verification in other related materials.

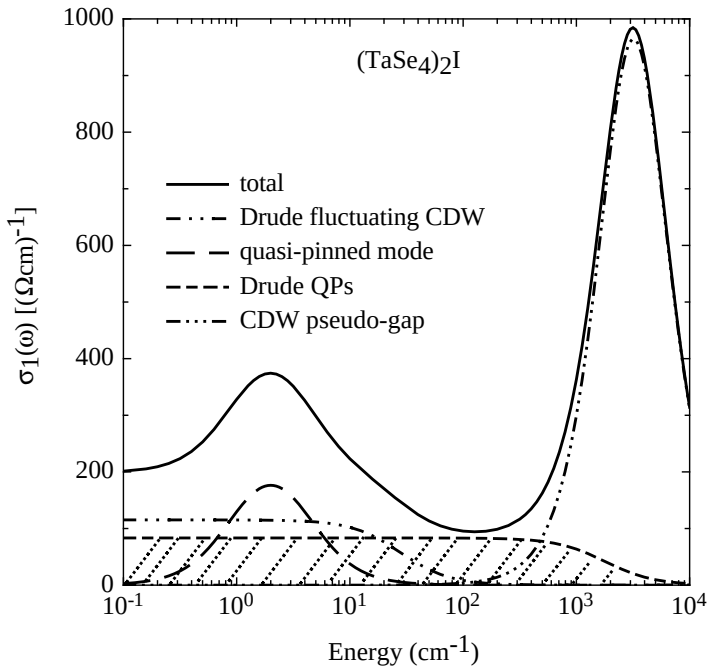

Figure 2.4: Optical conductivity of $(TaSe_4)_2I$ after the Lorentz-Drude model, based on the classical dispersion theory, reproducing the data at 270 K, along the chains direction. The components of the calculation are shown separately, and the quasiparticle (QP) weight is highlighted as a dashed surface.

2.3 Charge dynamics of the Heusler alloy Fe_2TiSn

L. Degiorgi, S. Dordevic and D. Basov

The title compound belongs to a large group of materials commonly referred to as Heusler alloys with general formula X_2YZ, where X and Y are transition metals and Z is a nonmagnetic element. These materials recently attracted a lot of attention in connection with possible d-electron heavy fermion (HF) behaviour, as first suggested for one member of this family, Fe_2VAl. However, careful measurements of the specific heat in high magnetic field have indicated that Schottky anomaly arising from magnetic clusters and not Kondo interaction might be dominant in these systems.

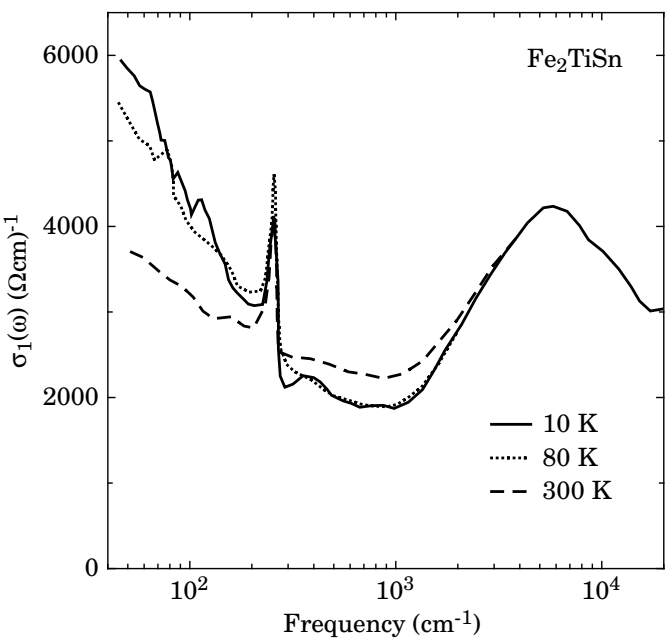

Figure 2.5: A narrow Drude mode and an interband transition at around 7000 cm^{-1} characterize the optical conductivity of Fe_2TiSn. The strong peak at 250 cm^{-1} is an optically active phonon mode.

Based on electrical resistivity and specific heat measurements, Fe_2TiSn has also been speculated to be a HF metal, even though the Sommerfeld γ-value of the specific heat is relatively small compared to conventional heavy fermion metals. Optical experiments are perfectly suited to settle down the issue. Figure 5 shows the real part of the optical conductivity, obtained by Kramers-Kronig transformations of the optical reflectivity measured over a very broad spectral range. The spectra are characterized by a Drude like mode with a width of about 120 cm^{-1} at 10 K and a broad peak centered on 7000 cm^{-1}. As temperature increases, the zero-energy peak broadens, whereas the peak at 7000 cm^{-1} displays almost no temperature dependence. The free-electron contribution to the optical conductivity of Fe_2TiSn appears therefore to be conventional Drude-like, with a small carrier density and relatively long mean free path. The interband transition at 7000 cm^{-1} can be interpreted as excitations across a pseudogap predicted in band-structure calculations. Our optical data do not support the notion that the Kondo interaction plays a dominant role in the charge dynamic of Fe_2TiSn. The analysis of the data, based on the phenomenological Lorentz-Drude model, shows that the scattering rate monotonically decreases with decreasing temperature, whereas the plasma frequency of the Drude component is essentially temperature independent. Such behaviour is typical of conventional metals and provides a strong argument against a heavy-fermion state in Fe_2TiSn. Indeed the hallmark of the latter state is a strong increase of m^* below a characteristic temperature (specific of each material). This is equivalent to a drastic reduction of the oscillator strength of the Drude component, which is not observed in our data. We find that the effective mass of the free carriers is essentially temperature independent. The apparent mass enhancement at low temperatures is due to Schottky anomaly arising from magnetic clusters. The latter effect can also explain the anomalous temperature dependence of specific heat and dc resistivity at low temperatures.

Chapter 3

Physics of mesoscopic structures, semiconductor nanostructures

Head
Prof. Dr. K. Ensslin

Academic Staff

A. Baumgartner	A. Dorn	C. Ellenberger
Dr. A. Franco-Obregon	A. Fuhrer	B. Grbic
Dr. T. Ihn	Dr. R. Jäggi	Dr. S. Kicin
Dr. R. Leturq	S. Lindemann	A. Pioda
V. Senz	Dr. R. Schleser	M. Sigrist
Dr. B. Simovic		

Technical Staff

C. Barengo	S. Schiesser	P. Studerus

Academic Guests
Prof. Wilhelm Zwerger, Univ. of Munich, Germany
Prof. Sergio Ulloa, Univ. of Ohio, USA

Administrative Staff
B. Abt

3.1 Kondo effect in quantum rings

A. Fuhrer, T. Ihn, and K. Ensslin, in collaboration with T. Heinzel (Uni. Freiburg), W. Wegscheider (Uni. Regensburg), M. Bichler (Walter-Schottky Insitute of the TU München)

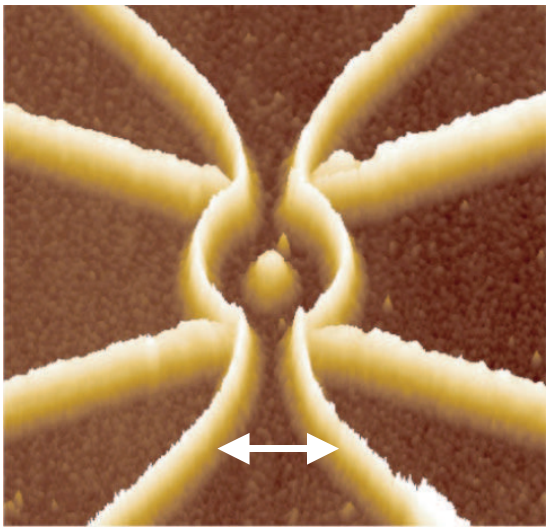

Figure 3.1: AFM micrograph of a quantum ring defined on the surface of an AlGaAs heterostructure. The white lines are oxidized areas below which the electron gas is depleted. The arrow marks a length of 300 nm.

Quantum rings have been fabricated by AFM-based nanolithography (see Fig. 3.1). In a magnetic field the Coulomb blockade maxima display a pronouced zig-zag dispersion which can be related to the single-particle energy spectrum of a perfect ring system. Quantum rings represent many-electron quantum dots whose energy spectrum can be understood on a quantitative basis. Mathematically speaking quantum rings are non-singly connected geometries. This is the reason why a magnetic field piercing the ring has such a pronounced influence on the dispersion of the states. In particular, we can distinguish between quantum levels, which have a well-defined angular momentum quantum number, and other states, which arise from a strong mixture of various different angular momenta. Many neighboring Coulomb maxima move pairwise as a function of magnetic field, they resemble so-called spin pairs. This corresponds to the situation where successive electron fill the same orbital state with opposite spin direction. This can be checked by analyzing the Zeeman splitting of orbital states in a parallel magnetic field (see below). One signature of spin effects in condensed matter in general is the Kondo effect, where an isolated spin is correlated with a surrounding electron cloud of opposite spin.

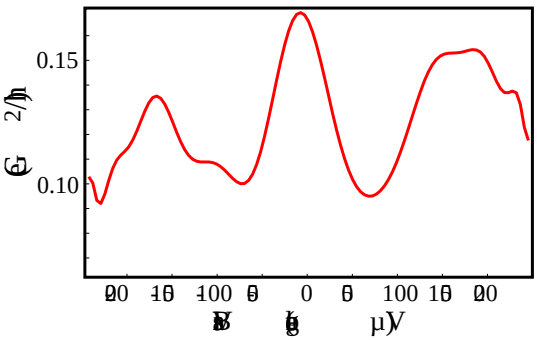

Figure 3.2: Differential conductance through the quantum ring in the Kondo regime as a function of bias. The maximum around zero bias is the so-called zero-bias anomaly.

Here we set out to explore the Kondo effect in a quantum ring. The so-called zero-bias anomaly (see Fig. 3.2) displays a pronounced maximum as a function of the applied bias across the ring. In the Coulomb blockade regime one rather expects a diode-like characteristic. The zero-bias-anomaly arises from transport through a level in the ring at the Fermi energy, which originates entirely from many-body correlations. In our quantum rings the observed zero-bias anomaly displays the magnetic field and temperature dependence expected for the Kondo effect. The special feature of the Kondo effect in a quantum ring is a periodic function of magnetic field. The reason for this observation is the fact that the Kondo temperature is an exponential function of the interaction strength as well as of the ring-lead coupling. Both quantities are flux-periodic which explains our observations at least on a phenomenological level. Not only orbital effects, but also spin effects in quantum rings can be understood on a quantitative basis.

3.2 Bouncing states in quantum dots

S. Lindemannn, T. Ihn, E. Bieri and K. Ensslin, in collaboration with T. Heinzel (Uni. Freiburg), G. Hackenbroich (Uni. Essen), D. Driscoll and A. Gossard (Univ. of California, Santa Barbara)

The position of Coulomb blockade (CB) resonances as a function of a gate voltage contains information on the energetic structure of the electron gas confined in a quantum dot. For a single current-carrying discrete state in the

dot, the line shape of the resonances is given by the convolution of a Lorentzian with the derivative of the thermally smeared Fermi function. The line width Γ of the Lorentzian is determined by the coupling of the resonant state to the leads. Within this model, the resonances are thus symmetric. However, various types of asymmetric Coulomb blockade resonances have been observed as well in the literature.

Here, we report on sequences of asymmetric peaks, in direct neighborhood to an approximately symmetric resonance at the center of the sequence. The steep flanks of these peaks face the symmetric resonance, and are governed by thermal smearing. In contrast the gently sloped flanks pointing away from the center peak are reasonably well approximated by a Lorentzian. This pattern is observed only in the regime where $\Delta \approx \Gamma \approx kT$ (Δ is the average single-particle energy level spacing in the quantum dot, kT denotes the thermal energy).

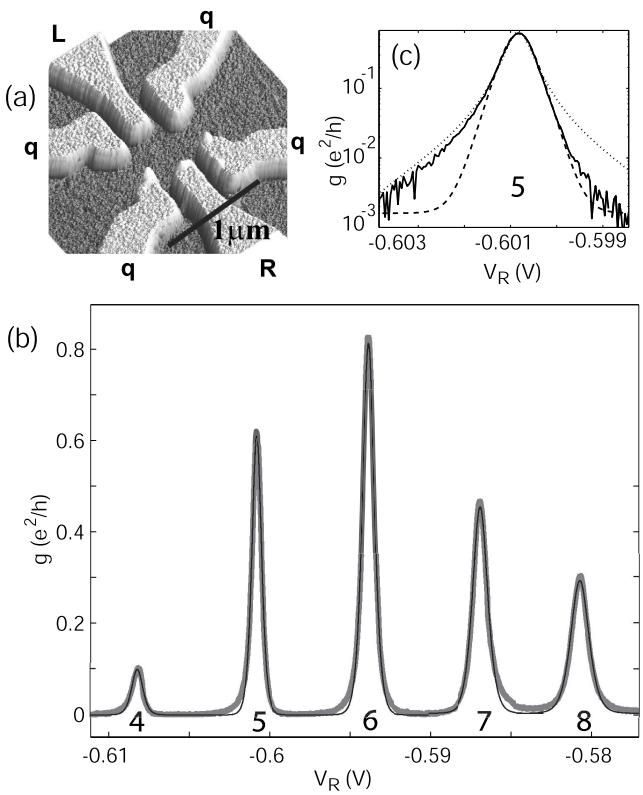

Figure 3.3: (a) The gate arrangement fabricated by electron beam lithography. The split gates labelled ”q” allow for adjustment of the tunnel barriers that couple the island to source and drain. The plunger gates ”L” and ”R” are used to tune the electrostatic potential of the dot. (b) Conductance through the quantum dot as a function of plunger gate voltage. The thin line is a fit of a thermally broadened lineshape to the measured CB resonances (semitransparent gray line). (c) Peak No. 5 on a logarithmic scale with a Lorentzian fit (dotted line) and a fit to a thermally broadened line shape (dashed line).

The quantum dot is defined by applying negative voltages to gate electrodes, Fig. 3.3 (a), on top of a Ga[Al]As heterostructure. The dot contains about 200 electrons. The experiments have been carried out in a dilution refrigerator with a base temperature of $60mK$.

Figure 3.3 (b) shows a series of CB resonances as a function of the right plunger gate voltage. The central and highest peak is No. 6. The other peaks are smaller and display asymmetric line shapes, with an amplitude and an asymmetry that decreases as the separation to peak No. 6 increases. This can be seen immediately by comparing the measurement to a fit assuming purely thermal broadening (thin line in Fig.3.3 (b)). As such fits are only appropriate in the limit $\Gamma \ll kT$, deviations occur in the tails of the symmetric peak as well. This requires nominally identical fit parameter for all resonances, which in this case is the temperature. The homogeneous part of the line shape, on the other hand, depends on the particular resonance.
The character of the peak asymmetry is investigated more closely in Figure 3.3 (c). It shows peak No. 5 on a logarithmic conductance scale. While the broad tail pointing away from the central peak (No. 6) is well described by a Lorentzian fit (dotted line), a thermal broadened line (dashed line) fits significantly better to the steep tail facing the central peak. This indicates that the asymmetric peaks have a gentle Lorentzian wing and a steep wing governed by thermal broadening.

We interpret these findings in terms of sparse dot states that couple particularly strongly to the leads. The wavefunctions of such states correspond to semiclassical electron trajectories that bounce back and forth between the entrance and the exit of the quantum dot. The developed picture can be generalized to explain qualitatively the occasional occurrence of asymmetric Coulomb blockade resonances in other experiments.

3.3 Stability of spin states in quantum dots

S. Lindemannn, T. Ihn, and K. Ensslin, in collaboration with T. Heinzel (Uni. Freiburg), W. Zwerger (Uni. Essen), D. Driscoll and A. Gossard (Univ. of California, Santa Barbara)

The energy spectrum of quantum dots in semiconductor nanostructures can be investigated by Coulomb blockade experiments. In quantum dots containing 50 or more electrons the energy spectrum has been analyzed primarily on a statistical basis and only in very exceptional cases (such as e.g. quantum rings) the energy spectrum can be understood in detail.

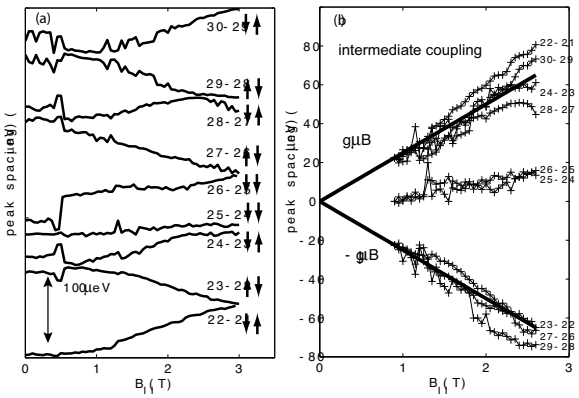

Figure 3.4: (a) Evolution of peak spacing with in-plane magnetic field. The peak spacing is extracted from the measured peak motion, converted into energy using the lever arm α and shifted together in arb. units. The peak spacing is in most cases flat up to a magnetic field of about 0.8 T. (b) Peak spacings are offset such that the lines cross at $B_{\|} = 0$ T.

In addition to the energy spectrum, the spin of the ground state of tunable quantum dots is of fundamental interest. In a picture of non-interacting electrons, each single-particle level is successively occupied by electrons with opposite spin according to the Pauli- principle. While the Hartree interaction term has no direct influence on the ground state spin, exchange effects favor the parallel alignment of spins and therefore tend to maximize the total spin of the ground state. The important parameter is the ratio of the interaction strength to the single-particle level spacing. In many-electron systems with more than 50 electrons, exchange effects involving electron spin can become comparable to the single particle level spacing Δ. This is the reason why spin pairs, i.e. the successive population with spin-up and spin-down electrons in the same orbital state are expected to occur rather seldomly.

Here we study quantum dots where interactions are comparatively strong. Conceptually, our measurements are based on the spectroscopy of the addition-spectrum of a quantum dot in the Coulomb-blockade regime. For magnetic fields $B_{\|}$ applied in the plane of the 2DEG we observe a pronounced shift of the Coulomb blockade peaks. The main contribution to this shift is due to the relative diamagnetic shift of energy levels in the dot which has a $B_{\|}^2$-dependence. This effect is the same for all conductance peaks. It can therefore be eliminated by analyzing peak separations rather than the absolute peak positions, if the reasonable assumption is made that the interaction energies are independent of $B_{\|}$. We find experimentally (see Fig.3.4 (b)) that for most conductance peaks in all coupling regimes the Coulomb peak separation is either constant or it changes linearly in $B_{\|}$. This can be explained on the basis of Zeeman splitting of the dot levels.

The Zeeman splitting for all magnetic fields investigated is much smaller than the Fermi energy in source and drain. We therefore expect that Zeeman effects in source and drain can be neglected and that both spin directions are available for tunneling through the dot at all magnetic fields. If differences of certain neighboring conductance peak positions display a linear magnetic field dependence we interpret such shifts as arising entirely from the Zeeman effect in the quantum dot.

3.4 Lateral superlattices on parabolic quantum wells

S. Lindemannn, T. Ihn, and K. Ensslin, in collaboration with T. Heinzel (Uni. Freiburg), S. Ulloa (Uni. Ohio), D. Driscoll and A. Gossard (Univ. of California, Santa Barbara)

Periodic lateral potentials imposed on two-dimensional electron gases (2DEG) have lead to the observation of classical as well as of quantum mechanical phenomena. Commensurability or Weiss oscillations were observed in the

magnetoresistance reflecting the commensurability of the lattice constant with the classical cyclotron diameter at the Fermi energy. This effect appears in magnetoresistance experiments as a $1/B$ periodic oscillation, where B is the magnetic field applied perpendicular to the sample surface. This periodicity arises from the fact that the classical cyclotron diameter at the Fermi level

$$2R_c = 2\frac{\hbar}{e}\frac{\sqrt{2\pi N_s}}{B},$$

is proportional to $1/B$. Here N_s is the two-dimensional carrier density. It was recognized early on that the effect can be explained in quasi-classical terms, namely by a guiding-center-drift resonance in the periodically modulated two-dimensional electron gas. The only quantum mechanical ingredient needed is the Fermi velocity of the electrons which is determined by the electron density.

Parabolic quantum wells (PQW) represent unique model systems where several electrical subbands can be controllably occupied in the growth direction. In contrast to two-dimensional electron gases, where the electron occupancy in the second subband is usually a small fraction (typically less than 10%) of the total electron density, the electron densities in the two lowest subbands in parabolic quantum wells can be similar within 30%. With carefully designed and fabricated back gate electrodes, one can control the electron density, the subband occupation, and the location of the electron distribution within the parabolic potential.

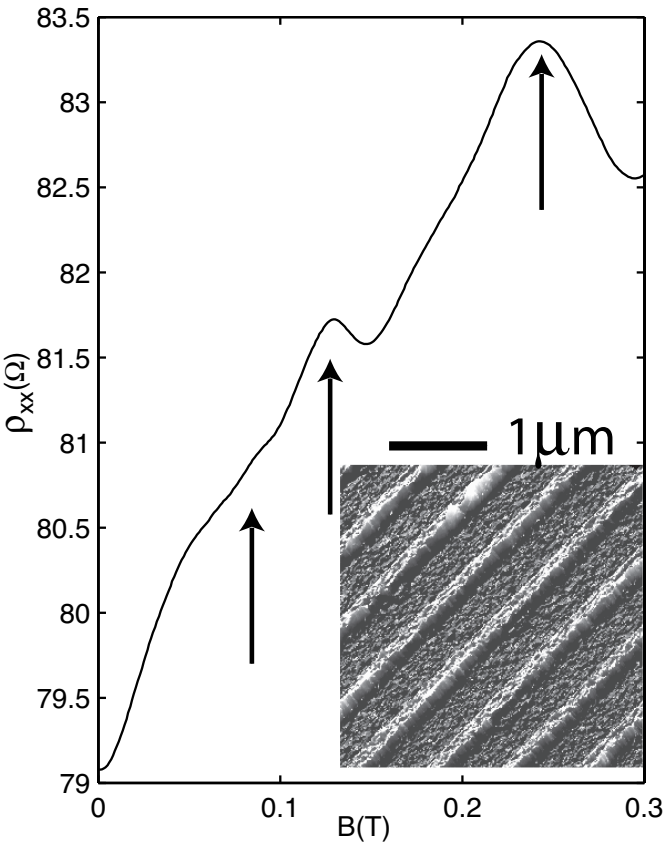

Figure 3.5: Magnetoresistance ρ_{xx} in the regime of one occupied subband. The arrows mark the positions of maxima calculated with the corresponding carrier densities as fitting parameters. The inset shows an image of the nanostructured front gate electrode.

Here we present experimental results obtained on a lateral superlattice (see inset of Fig.3.5) fabricated on a parabolic quantum well. In contrast to previous experiments on 2DEGs several electronic subbands are occupied in this case. For two occupied subbands carriers with two different Fermi velocities coexist at the Fermi energy. We set out to explore the consequences of this situation for commensurability oscillations which are predominately a classical effect, as discussed above. We find that two sets of commensurability oscillations occur in the magnetoresistance, each related to a specific subband, despite the presence of intersubband scattering. Moreover, this structure has the added flexibility that the amplitude of the lateral potential modulation can be tuned by a patterned front gate electrode, and the homogenous back gate used to tune the subband occupation. This control leads to a different ratio of the potential modulation and Fermi energy, which is the relevant parameter describing the magnetoresistance oscillations. Positive magnetoresistance measurements at higher fields allow for a separate determination of the potential modulation amplitude. We find that there is a regime of gate voltages where strain dominates the modulation amplitude. In this situation, the transport data exhibit commensurability maxima which can be identified with the third harmonic of the potential modulation.

Figure 3.5 shows a magnetoresistance trace obtained for constant back gate voltage $V_{bg} = 0$. Starting from zero magnetic field, we first observe an increase in the magnetoresistance related to the drift of the guiding center along the equipotentials of the modulation. This is then overcome by magnetic breakdown at a critical field, just before the well known commensurability oscillations begin to occur. At yet higher magnetic field a positive parabolic magnetoresistance is observed (not shown), which can also be used to extract the magnitude of the potential modulation.

3.5 Charging of ErAs islands in an AlGaAs heterostructure

A. Dorn, M. Peter, T. Ihn, and K. Ensslin, in collaboration with D. Driscoll and A. Gossard (Univ. of California, Santa Barbara)

The electronic potentials in semiconductor nanostructures can usually be tuned by nano-patterned top gate electrodes. It is often desirable to have an additional back gate electrode, because it allows to control the Fermi energy of the entire system. The fabrication of backgate electrodes usually incorporates a layer of low-temperature grown GaAs, which acts as an intermediate quasi-metallic layer with Schottky barriers to the surrounding semiconductor. In this realm we investigate a different barrier layer consisting of ErAs islands. The samples for this study were grown by molecular beam epitaxy. The two-dimensional electron gas is located 34nm below the surface at an AlGaAs/GaAs interface, separated from the metallic backgate (Si doped GaAs) by 1.3μm. Sandwiched in-between are 20 ErAs layers spaced by 25nm. ErAs can spontaneously form islands when deposited on GaAs. The morphology of the islands depends on the growth parameters. In our wafer sequences of 1.5ML of Er were deposited at 540 ^{o}C corresponding to an island size of roughly 5-6nm. High quality crystal overgrowth has been reported for ErAs layers below 3ML owing to the possibility of seeding between the islands. At 1.7K the 2DEG is well insulated from the BG (backgate) with resistances in the GOhm range up to breakdown voltages of about +6.5V on the BG, with the Hall bar and leads covering an area of about 0.5mm^2. In a simplified model the ErAs islands and the surrounding GaAs layers can be viewed as a semiconductor-metal-semiconductor contact where one diode is always in reverse bias. It is remarkable, that very similar breakdown characteristics (7-12V) have been observed in macroscopic ErSi2 Schottky contacts on n-type GaAs.

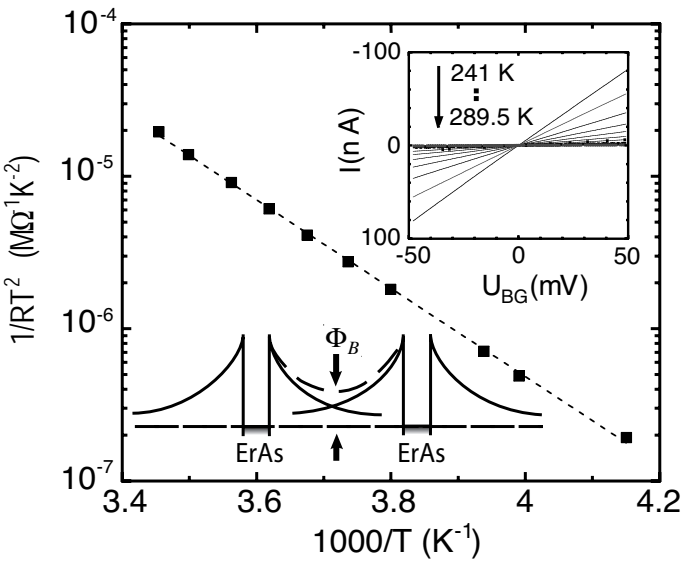

Figure 3.6: Arrhenius plot of the inverse resistance 2DEG/BG. Upper inset: U/I traces (raw data) used to determine the resistance. Lower Inset: illustration of the Schottky barrier minima between the islands that are predominantly probed by this method.

Temperature dependent voltage vs. current measurements from the BG into the 2DEG were performed to determine the effective barrier height of the ErAs island layers. Current-voltage sweeps between -50mV and +50mV were done from 1.7K to room temperature. The upper inset in Fig.3.6 shows the regime for temperatures below 240K, where significant changes in the resistance occur. Due to the small voltage range the slope is basically linear and the effective Schottky barrier height can be determined from an Arrhenius plot (Fig.3.6) facilitating the well-known relation for thermionic emission. Because the slopes of U/I-traces around 0V were used this method also yields the correct barrier height if the island layer is viewed as acting like two diodes in opposite bias. The obtained value of about 580 meV for the Schottky barrier height is in excellent agreement with values found in macroscopic Er-diodes on GaAs with low quality interfaces and across barriers formed by arrays of nanometer sized W-discs. Since transport is dominated by channels with low resistance this value is representative for the barrier minima in the overlap regions between the islands (lower inset Fig.3.6). If high voltages are applied to the BG, the ErAs islands are charged. This effect can be quantified by measuring the Hall electron density in the 2DEG at 0V BG, then setting the BG voltage to a higher value and measuring the electron density at 0V BG again. By scaling the onset value with the ratio of the distances 2DEG/ErAs-layer and BG/2DEG a value of about 1V is obtained which can be identified with the Schottky barrier height.

3.6 Low-temperature scanning gate experiments on semiconductor nanostructures

S. Kicin, A. Pioda, A. Baumgartner, T. Ihn, and K. Ensslin, in collaboration with D. Driscoll and A. Gossard (Univ. of California, Santa Barbara)

In spite of the metrological accuracy of quantum Hall plateaus, the microscopic details of the samples used in experiments are rather complex. Here we set out to explore the scattering potentials in a narrow Hall bar with a low temperature scanning gate set-up. We have locally investigated a 4 μm wide shallow two-dimensional electron gas realized in a Ga[Al]As heterostructure with a backgate. The conducting tip of a scanning force microscope was scanned at constant height and constant tip-sample voltage above the Hall bar structure at a temperature of 300 mK and in magnetic fields up to 9 T. Under these conditions the sample exhibits the quantum Hall effect in conventional magnetotransport measurements. Using the scanning tip as a local gate we mapped the change in longitudinal ($\Delta R_{xx}(\vec{r})$) and transverse resistance ($\Delta R_{xy}(\vec{r})$) as a function of tip position $\vec{r}$ at various magnetic fields B and backgate voltages U_{bg}.

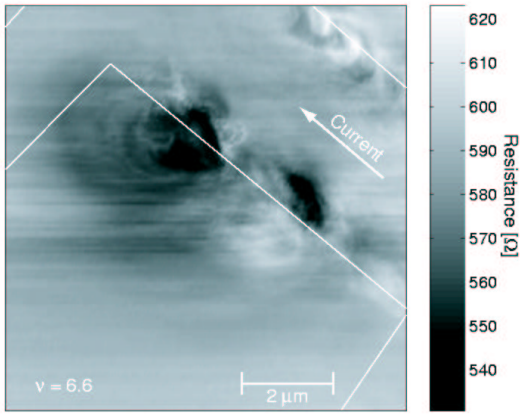

Figure 3.7: Scanning gate image of a region on the Hall bar (indicated by the white lines). The grey scale corresponds to the resistance change as the biased metallic tip is scanned across the electron gas.

Scanning gate images (see Fig.3.7) for an example, white lines show position of Hall bar) were taken in coarse steps of filling factors $\nu = hn_{\mathrm{s}}/(eB)$ (sheet electron density is $n_{\mathrm{s}} = 6 \times 10^{15}\,\mathrm{m}^{-2}$). Maps of resistance change, $\Delta R_{xx}(\vec{r})$ and $\Delta R_{xy}(\vec{r})$, taken at corresponding filling factors $\nu = 2n + \varepsilon$ (n=2,3; $|\varepsilon| < 1$) were found to be clearly correlated reflecting the general $1/B$-periodicity of the quantum Hall effect. Measurements at different backgate voltages fit into this general picture. At even filling factors $\nu = 2n$ we found $\Delta R_{xx}(\vec{r}) \approx 0$ and $\Delta R_{xy}(\vec{r}) \approx 0$ within experimental resolution with the tip scanning in the region between the voltage probes. This observation shows that no backscattering from one sample edge to the other can be caused by the repulsive tip induced scattering potential.

In a second series of measurements we focused on filling factors in the vicinity of $\nu = 4$ with the tip scanning between the voltage probes. At these filling factors the tip induced Hall resistance change remains zero while $\Delta R_{xx}(\vec{r})$ becomes finite and measurable. This implies that the tip causes local backscattering from one sample edge to the other. This situation is similar to selective backscattering experiments of edge channels, where gate stripes across the Hall bar have been used, with the important difference that we are able to map out the scattering probability $\Gamma(\vec{r})$ from one sample edge to the other *locally*.

Measurements at other filling factors show a rich variety of structures both in ΔR_{xx} and ΔR_{xy}. For example, at some values of ν there is filamentary structure on a length scale of 100 nm and sometimes halo structures centered around some special spots, which testifies to the high spatial resolution achievable in such experiments. Changes of the Hall resistance arise typically, when the tip is located close to or in-between Hall contacts.

3.7 Phase sensitive measurements on a four-terminal ring

M. Sigrist, A. Fuhrer, T. Ihn, and K. Ensslin, in collaboration with W. Wegscheider (Uni. Regensburg), M. Bichler (Walter-Schottky Insitute of the TU München)

Two-teminal double-slit measurements in nanostructures do not allow the determination of the relative transmission phase due to the generalized Onsager relations. It has been demonstrated that in a multi-terminal geometry the transmission phase can be directly observed. A phase-lapse for the transmission through a Coulomb blockaded quantum

dot was found in these experiments. The explanation of this observation is still controversially discussed and other experiments are lacking so far.

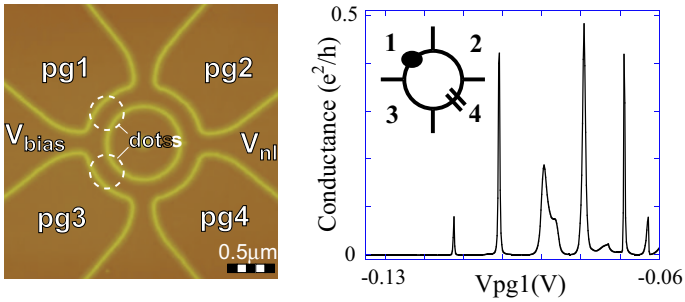

Figure 3.8: a) Ring sample defined by AFM-lithography. Two dots are formed in arm 1 and 3 for negative plunger gate voltages pg1 and pg3. b) Coulomb blockade oscillations in the conductance through dot 1 when the other arms of the ring are pinched off.

We have realized a four-terminal Aharonov-Bohm (AB) ring on a shallow Ga[Al]As heterostructure by AFM-lithography (Fig.3.8a)). Two or more quantum dots can be electrostatically induced by appropriate plunger gate voltages. While clear Coulomb oscillations are observed (Fig.3.8b)), the precise location of the charged islands is not well defined along one of the arms of the ring. For the measurements presented here, two quantum dots were induced in the ring by the plunger gates pg1 and pg3 (see Fig.3.7a)). The phase of Aharonov-Bohm oscillations as a function of magnetic field was measured at temperatures around 50 mK in a dilution refrigerator. A bias voltage V_{bias} was applied to the left contact while the contacts at the top and the bottom (I_1 and I_3) were grounded via two current-voltage converters. The relative transmission phase was determined from the non-local voltage V_{nl} measured at the right probe.

Phase shifts of the AB oscillations in V_{nl} could be detected in a regime in which the quantum dots forming in segment 1 and 3 are close to the Coulomb blockade regime and pronounced conductance peaks exist. We observe pronounced AB-oscillations in the non-local voltage. The phase shift can be directly followed. Typically, a phase of about π accumulates by sweeping through a well isolated conductance peak, similar to previous observations. Smaller or larger phase shifts are occasionally observed if neighboring conductance peaks overlap strongly.

Adding an electron to both of the dots results in a negligible phase shift as expected. If the dots are operated in a regime, where the coupling to source and drain is minimized, the visibility of the AB-oscillations in the Coulomb blockade regime goes down. In the regime presented here, the conductance between Coulomb blockade maxima is large enough to allow for the observation of clear AB-oscillations. For a gate sweep of dot 3 over several Coulomb peaks the tendency in our data is towards a stepwise increase of the phase with increasing gate voltage.

In the open regime of the dots and at high magnetic fields (about 5 T) a continuous phase increase can be found with increasing gate voltage as observed in other experiments.

3.8 Topology of the nuclear pore complex

R. Jäggi, A. Franco-Obregn, and K. Ensslin, in collaboration with P. Mühlhäusser, F. Thomas, U. Kutay (Institute of Biochemistry, ETH Zürich)

Nuclear Pores are one of the largest protein complexes present in the cell. The Nuclear Pore Complex (NPC) is comprised of some 30-50 different proteins, or nucleoporins, that are present in multiple copies. Because of its large size and high density on the nuclear envelope the NPC was one of the first biological macromolecular complexes to be examined with an Atomic Force Microscopy (AFM). Despite the wealth of structural information obtained from this approach, however, little new information was gained concerning classical nuclear transport pathways. In a classical sense, nuclear transport is mediated by transport receptor proteins that chaperone cargo through the NPC after making contacts with specific nucleoporins. Whether cargo translocation via classical pathways is accompanied by conformational changes in NPC structure is still an open question.

Imaging of nuclear envelope samples was performed with a AFM using silicon nitride cantilevers (spring constant 0.16 N/m) with oxide sharpened tips. Scanning was conducted in liquids using tapping mode. In this mode the cantilever is oscillated at a set frequency (typically 8 kHz), and the oscillation amplitude serves as a feedback signal to follow surface topology. Since the tip only intermittently touches the surface, lateral forces exerted on the sample are reduced and image resolution is increased. The oscillation amplitude (setpoint) was carefully monitored during imaging to minimize normal forces exerted by the cantilever tip.

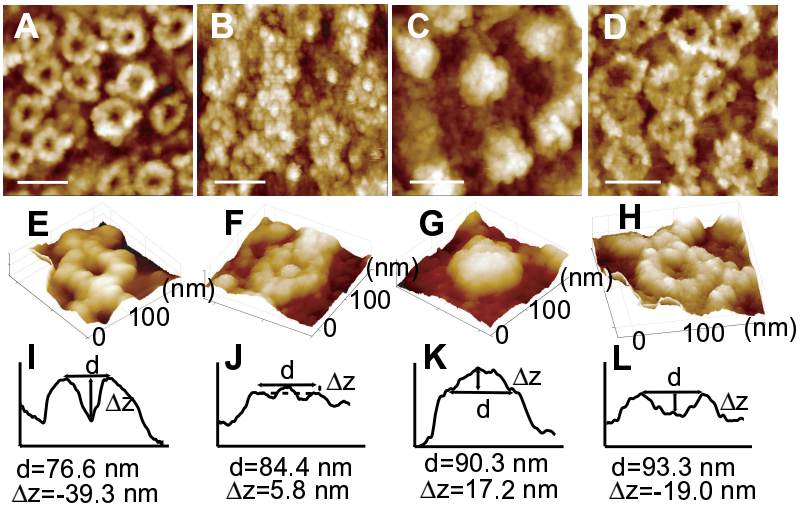

Figure 3.9: Distinct NPC topologies are clearly discerned using scanning force microscopy. Scanning force images of NPCs that were untreated (A, E, I), subjected to calcium store depletion using 10 mM EGTA for 10 minutes (B, F, J), incubated in the 45-462 importin β mutant for two minutes (C, G, K) or treated with 1,6-hexanediol for two minutes (D, H, L). All treatments were performed at 4°C. Scale bars in panels A-D represent 200 nm. Panels E-H are respective three-dimensional representations of individual NPCs. Panels I-L are cross-sectional profiles of the NPCs shown directly above; vertical and horizontal scale bars represent 20 nm. NPC diameter (d) and central channel depth (d_z) were measured. The 45-462 importin β mutant lacks functional Ran- and importin α-binding domains. Therefore, changes in NPC topology observed in C, G and K arise from mutant protein binding over the central channel region leaving the rim of the NPC clearly resolvable.

Changes in NPC topology were investigated by taking cross-sectional profiles through single NPCs. The NPC topology was characterized by measurements of diameter (d) and central pore depth (d_z) as indicated in Fig.3.9. To this end, external points on the pore rim and at the location of the central pore depression were determined and their relative distances were analyzed using an automated process. Measured data sets for depth and diameter were well described by normal Gaussian distributions. In all cases diameter and depth data are given as mean values standard error of the mean. In the figure legends the sample characteristics are given as the number of individual measurements/ different nuclei analyzed.

Importin β, one of the best-understood transport receptors, simultaneously interacts with cargo (via importin α) and FG-repeats on passage through the NPC. Ran-GTP binding is essential for dissociation of the import complex from the NPC and consequently for functional termination of the transport process. Truncating the Ran-GTP binding domain of importin β causes its irreversible binding to the NPC with subsequent inhibition of nuclear transport. Our results indicate that transport block by the 45-462 mutant of importin β results from the occupation of available FG-binding sites (Fig.3.9 C) and G)), implicating steric hindrance of further binding, rather than conformational changes in NPC structure.

Our experimental data might indicate that we are observing two closely related, and mechanistically separable forms of transport modulation through the NPC. On the one hand, tight binding of importin β mutants to FG-repeats increases the vertical aspect of the NPC in a manner that might explain the dominant negative transport block previously ascribed to these mutant transport receptors. On the other hand, amphipathic molecules might interfere with the interaction of lumenal FG-repeats thereby increasing NPC diameter and accounting for the breakdown in selectivity observed with these molecules. Our experiments thus establish an important link between different approaches to the understanding of transport through NPCs. In particular we demonstrate that topographic information obtained from AFM imaging is in accordance with scenarios deduced from purely biochemical experiments. Some of the observed features, such as increased pore diameter upon exposure to the I178D mutant require explanation beyond present biochemical models for the NPCs.

Chapter 4

Condensed matter at low temperatures

Head
Prof. Dr. H. R. Ott

Academic Staff
Dr. C. Beeli
Dr. M. Chiao
E. Felder
Dr. J.L. Gavilano
Dr. I. Landau
Prof. Dr. R. Monnier
S. Mushkolaj
B. Pedrini
D. Rau
S. Signoretti
Ch. Soltmann
Dr. A. Sologubenko
G. Wigger
M. Weller

Technical Staff
H.R. Aeschbach
P. Wägli
H. Thomas
R. Wessicken
S. Siegrist

Administrative Staff
I. Heer-Mettler
D. Amstad

Academic Guests

A. Bilusic, Institue of Physics, Zagreb, Croatia (- 15.7.2002)

Melting and freezing

Head
Prof. Dr. J. Bilgram

Academic Staff
H. Singer
O. Wittwer

Technical Staff
H.R. Aeschbach

4.1 Physical properties of hexaborides

4.1.1 ^{11}B-NMR studies of YbB_6

Sh.Mushkolaj, J. Gavilano,D. Rau, M. Chiao, and H.R. Ott

Recently, rare-earth and alkaline earth hexaborides enjoyed a new interest. Because of their simple cubic crystal structure and the relatively small number of atoms per unit cell it was believed that the physical properties of these materials may be understood using some simple arguments, basically counting the number of electrons in the unit cell. Hence, rare-earth hexaborides with divalent cations were thought to be semiconductors, whereas hexaborides with trivalent rare-earth cations were expected to be metals.

Some rare-earth hexaboride compounds, such as EuB_6, CeB_6, and SmB_6 exhibit a variety of unexpected low-temperature physical properties [1]. In YbB_6 the rare-earth ions are expected to adopt a divalent configuration, therefore this compound ought to be a nonmagnetic semiconductor.

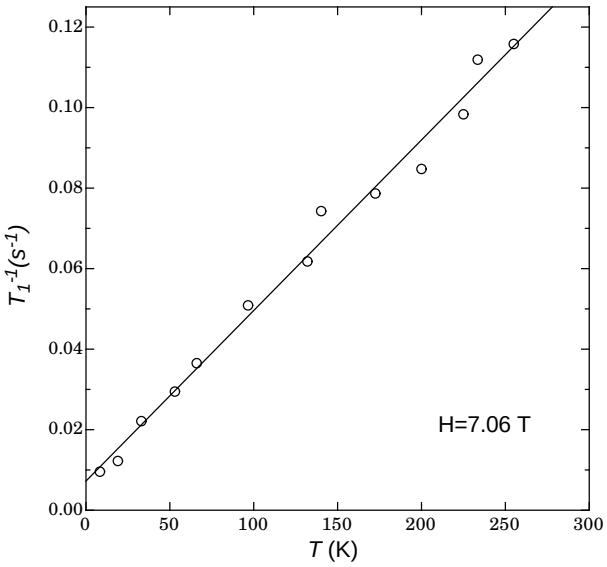

Figure 4.1: $T_1^{-1}(T)$ in ^{11}B-NMR of YbB_6 measured in an external field of 7.06 T.

We have measured the dc-susceptibility χ of YbB_6 as a function of temperature and applied magnetic field. The $\chi(T)$ data follow a Curie-Weiss-type law at temperatures above 20 K. From fitting the $\chi(T)$ data we get an effective magnetic moment of $0.1\mu_B$ per formula unit. However, contrary to Yb^{+2} ions which are non-magnetic, Yb^{+3} ions carry a moment of the order of $4\mu_B$ per ion. The experimental value of $0.1\mu_B$ implies that 2% of all the Yb ions adopt the Yb^{+3} configuration, the rest is divalent. The temperature variation of the electrical resistivity $\rho(T)$ of our material is that of a metal. It decreases with decreasing temperatures, by a factor of about 3 between room temperature and 4.2 K.

Metallic behaviour is also reflected in the results of ^{11}B-NMR measurements, which were made using a collection of single crystals of YbB_6.

Similar to $\chi(T)$ and $\rho(T)$ the spin-lattice relaxation rate $T_1^{-1}(T)$ exhibits a typical metallic (Korringa-type) behaviour as shown in Figure 4.1.

The shape of the ^{11}B-NMR spectra is characteristic for nuclear spins I=3/2 in randomly oriented grains. From the extension of the wings of the spectra we infer a quadrupolar frequency, ν_Q=$e^2qQ/2h$, of 630 kHz. From the experimentally determined ^{11}B ν_Q and using the ^{11}B nuclear electric quadrupole moment Q, we extract the value of the major principal component of the electric field-gradient at the boron sites V_{zz}=$2h\nu_Q/eQ$ = 1.54X10^{21} V/m^2.

[1] H.R. Ott et al., Physica B **281-282**, 423 (2000).

4.1.2 Pressure studies of CaB_6 and $Eu_{1-x}Ca_xB_6$

M. Chiao and H. R. Ott

The reported high temperature ferromagnetism in CaB_6 [1] has motivated many researchers to investigate this and related divalent hexaborides. Calculations of the electronic structure of CaB_6 predict a band overlap [2] while optical spectroscopy measurements indicate a full band gap of $\sim$1 eV [3]. High pressure measurements can shed light on this fundamental issue.

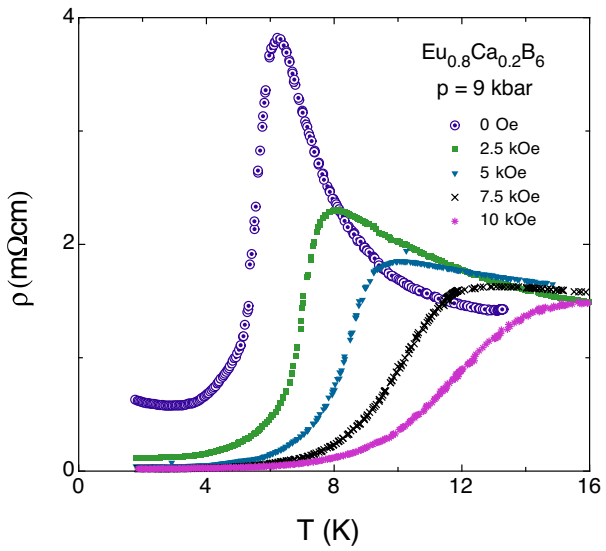

Figure 4.2: Resistivity as a function of temperature for $Eu_{0.8}C$

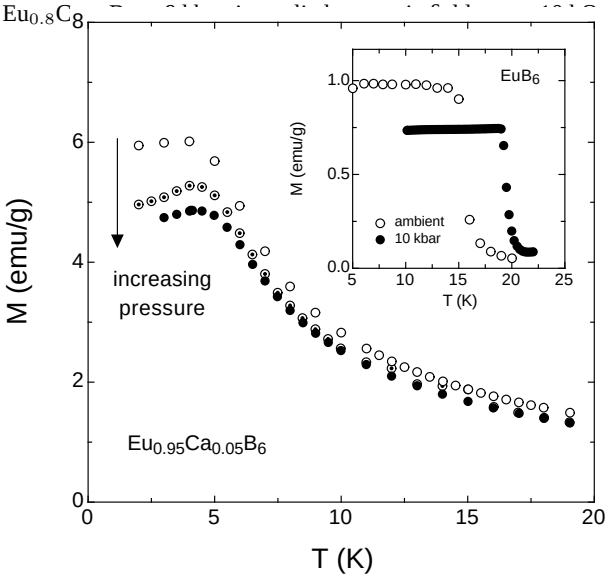

Figure 4.3: Magnetization as a function of temperature of $Eu_{0.95}Ca_{0.05}B_6$ in a field of 1 kOe, at pressures up to 8 kbar (closed circles). Inset: pure EuB_6 in a field of 50 Oe, showing a stronger pressure dependence of ordering temperature.

Numerous CaB_6 samples were characterized at ambient pressure. None were found to be ferromagnetic at any temperature, in agreement with the results of Matsubayashi and co-workers [4]. Moreover, nominally identical crystals displayed widely disparate resistivity curves over a temperature range of 300 K. One semimetallic crystal ($\rho_0 < \rho(300\text{K})$) showed a significant positive magnetoresistance and metallic behaviour under $\sim$20 kbar of pressure. Another exhibited semiconducting behaviour and neither an applied magnetic field nor pressure had any effect on the resistivity. The latter behaviour appears to be the norm. From these results we can draw the following conclusions: (1) bulk ferromagnetism is not intrinsic to CaB_6; and (2) CaB_6 is highly susceptible to the effects of defects and impurities, which is typical of semiconductors close to a metal-insulator transition.

The properties of EuB_6 crystals are less affected by crystal imperfections. The presence of Ca in $Eu_{1-x}Ca_xB_6$ primarily dilutes the local moment Eu spins. Ferromagnetic behaviour remains, though at lower temperatures than in pure EuB_6, manifested by a distinct peak in $\rho(T)$ at the Curie temperature. Application of a magnetic field suppresses the peak, much like in the manganites, suggesting the presence of domains which become aligned by a magnetic field. However, pressure changes the ordering temperature only weakly, as shown by Figure 4.2. The magnetisation is more sensitive to pressure, showing a decrease with increasing pressure (Figure 4.3).

This may be explained by the presence of antiferromagnetic (AF) correlations competing with the ferromagnetic ones. Pressure may then favour the AF exchange and create some canted AF state, with a weaker magnetization and no significant change in the ordering temperature. By applying a field, the spins would align and reduce the resistivity, corresponding to the results in Figure 4.2.

[1] D. P. Young et al, Nature **397**, 412 (1999).

[2] S. Massida et al, Z. Phys. B **102**, 83 (1997).

[3] P. Vonlanthen et al, Phys. Rev. B **62**, 10076 (2000).

[4] K. Matsubayashi et al, Nature **420**, 144 (2002).

4.1.3 Electronic transport in EuB_6 and related hexaborides

G.A. Wigger and H. R. Ott

The extraordinarily large magnetoresistance in EuB_6 is still a phenomenon that lacks a convincing explanation. Although band structure calculations have been made for that compound, they cannot be used as a basis for a detailed analysis of transport data, due to their inadequate description of exchange and correlation effects. In order to extend the data base, we measured simultaneously the transverse magnetoresistance, the Hall effect and the magnetization of

a flat EuB_6-platelet. We observed an anomalous negative Hall voltage varying linearly with the product between the magnetization and the magnetic part of the resistivity, which implies skew scattering of the conduction electrons at non-magnetic defects.

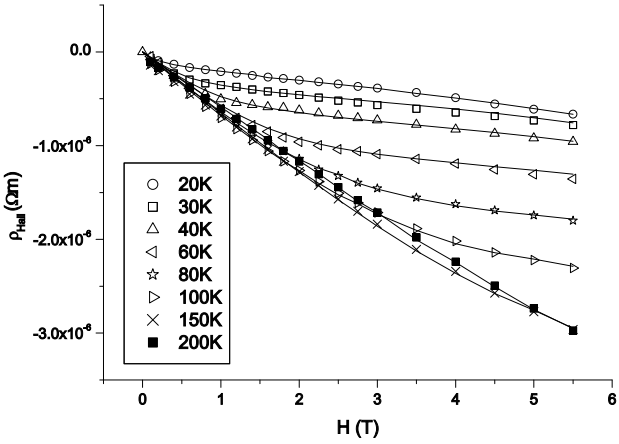

Figure 4.4: The Hall resistivity of EuB_6 at different temperatures and fields. The solid lines are consistent with a dominant skew scattering of electrons.

We continued our studies of magneto-transport properties in $Eu_{1-x}Ca_xB_6$ samples. We found, at a Eu-concentration of about 25% the steepest increase of the resistivity at low temperatures. A magnetic field of 1T reduces the zero-field residual resistivity to a value five orders of magnitude smaller. The field dependence of the resistivity reduction suggests a phase transition whose nature needs to be established by measurements of the magnetic susceptibility.

Electronic transport data were also obtained for $Eu_{1-x}Ca_xB_6$ alloys with x close to 1. The measured resistivities exhibit power-law type increases with decreasing temperature, indicating a hopping motion of the charge carriers rather than conduction via Bloch states. With these experiments, we hope to elucidate the electronic structure of hexaborides with divalent cations.

Doping EuB_6 with trivalent Sm-ions is expected to alter the concentration of itinerant charge carriers and to provide magnetic impurities in this compound. We measured the specific heat, the magnetization, the resistivity and the ac-susceptibility of $Eu_{0.94}Sm_{0.06}B_6$. All properties exhibit anomalies around 4.8 K, indicative of a phase transition at this temperature. This observation implies that Sm^{3+} affects the magnetic properties of EuB_6 much more drastically than Ca^{2+}.

4.1.4 4f-5d Excitations in europium hexaboride

R. Monnier, in Collaboration with Z.Szotek and W.Temmerman, Daresbury Laboratory

The recently measured magnetooptical spectrum of EuB_6 (S. Broderick et al., Eur. Phys. J. B**27**,3 (2002)) displays two characteristic features at 0.3 and 1.0 eV respectively. The former was interpreted as an intraband excitation, while the second was attributed to the excitation of a 4f electron to the conduction band. As a first step towards understanding the magnetooptical spectrum, we have computed an approximate energy for the second process, using the self-interaction corrected (SIC) LSD method, which has been successfully applied to the study of the valency of rare earths in the elemental metals and in the monosulfides (P.Strange et al., Nature **339**, 756 (1999). From the difference in total energy per unit cell between a calculation in which the SIC was applied to all 7 electrons of the 4f shell (divalent Eu), and one in which only 6 4f orbitals were SIC corrected (trivalent Eu) , we obtained an excitation energy of 1.06 eV,which confirms the interpretation given by Broderick et al.

4.1.5 Work function and surface relaxation in lanthanum hexaboride

R. Monnier, in collaboration with B. Delley (PSI)

Lanthanum hexaboride is a well known thermoemission cathode material, due to its low work function (W≈2.6 eV). We have computed the work function of this material, using a periodic slab geometry, in which successive slabs with a thickness of 3 unit cells and terminated on each side by a La layer, were separated by a ≈38 a.u. thick vacuum region.

In the unrelaxed (bulk) geometry, the calculated value of the work function is 3.39 eV. Allowing for geometrical relaxation increases this value to 3.76 eV, due to a strong (50 %!) reduction of the the distance between the outermost La layer and the underlying B plane, and a 42 % increase of the distance of the latter to the next (B) plane in the structure. Our findings suggest that the thermoemission process in these materials is not purely electronic, but may be assisted by another mechanism. Experimentally it was observed (Lafferty , Phys. Rev. **22**, 299 (1951)) that, concommitant to the emission of electrons, evaporation of La takes place at a rate of 1 atom per 1 million electrons, which led the author to suggest, that La atoms were diffusing from the bulk to the surface, continuously replacing the ones lost by evaporation. In order to verify that conjecture, we have started to compute the height of the activation barrier for a La atom to jump into a neighbouring cation vacancy. Our preliminary results indicate that the barrier height is of the order of 3 eV, which makes single-atom jumps highly unlikely.

4.2 Superconductivity

4.2.1 Anomalous low-temperature thermal conductivity of MgB_2

A.V. Sologubenko, J. Jun, S. M. Kazakov, J. Karpinski, H.R. Ott

MgB_2 provides a unique opportunity to study multiband effects in superconductivity. According to both theoretical calculations and various experimental results, the superconducting energy gap appears to differ substantially on different sheets of the Fermi surface with different dimensionality: the value of the gap of the two-dimensional (2D) parts at $T = 0$ K is close to $1.76 k_B T_c$, as predicted by the original weak-coupling BCS theory, but the gap associated with the 3D sheets of the Fermi surface is 3 to 4 times smaller.

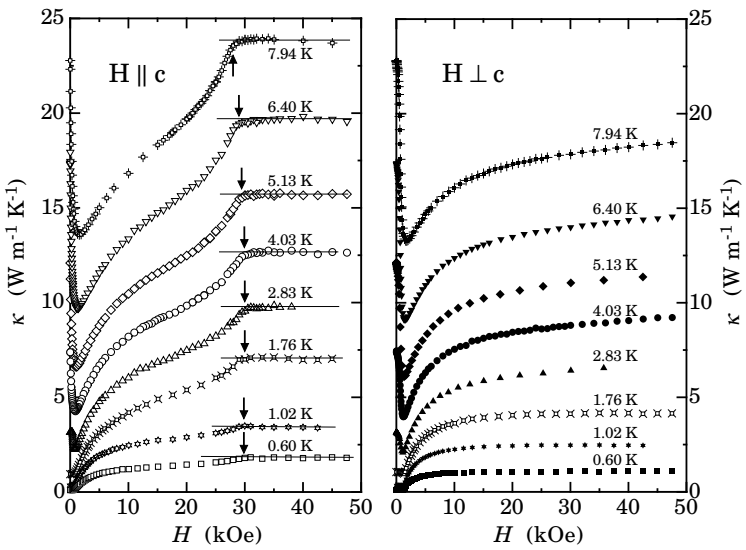

Figure 4.5: Thermal conductivity in the basal plane of MgB_2 vs H at several fixed temperatures. The arrows denote the upper critical field H_{c2} for $H \parallel c$.

We have measured the thermal conductivity κ parallel to the basal plane of the hexagonal crystal lattice of MgB_2 as a function of varying magnetic fields H temperature. In Fig. 4.5 we present several $\kappa(H)$ curves, measured at constant temperatures below 8 K for field directions both parallel and perpendicular to the c-axis. For the analysis of the data, contributions to the heat transport due to both electronic quasiparticles (κ_e) and phonons ($\kappa_{\rm ph}$) are considered. In all type-II superconductors, the quasiparticles associated with the vortices, induced by magnetic field at $T < T_c$, not only enhance the scattering of phonons and hence reduce $\kappa_{\rm ph}$, but also enhance κ_e. What is unprecedented in the curves shown in Fig. 4.5 is the very rapid increase of κ_e at relatively low fields, following the initial decrease of $\kappa_{\rm ph}$.

The field dependence of κ_e is explained in terms of a two-band model. The pairing interaction leads to a gap Δ_L in one of bands whereas Cooper-pair tunneling leads to merely induced superconductivity and a significantly smaller gap Δ_S in the second band. In terms of the two-gap model, the saturation of $\kappa_e(H)$ much below H_{c2} may be regarded as evidence for the field-induced closing of Δ_S. The heat transport via quasiparticles of the band associated with the larger gap is significant only in the vicinity of and above the upper critical field H_{c2}.

Another important observation is that below 8 K, the range of possible values of κ_e in the field-induced normal state ($H \parallel c > 30$ kOe) significantly exceeds the values calculated using the Wiedemann-Franz law (WFL) from the experimental value of the bulk electrical resistivity ρ. Moreover, $\kappa_e(T)$ does not exhibit the expected linear-in-T behavior. This violation of the WFL at low temperatures is quite unexpected because the validity of this law

normally holds for the Fermi-liquid ground state of common metals at low temperatures in the residual resistance regime. The observed deviation from the WFL, in the form of a peak-type structure of κ_e/ρ vs. T, might be the consequence of some kind of anomalous gap formation in the electronic excitation spectrum in the normal state at very low temperature.

4.2.2 Temperature dependence of the upper critical field of type-II superconductors from isothermal magnetisation data

I. L. Landau and H. R. Ott

According to the Ginzburg-Landau theory, the magnetic moment of a superconductor placed in an external magnetic field H may be written as $M(H,T) = H \cdot f(H/H_{c2})$, where H_{c2} is the upper critical field, and the function f depends only on the ratio H/H_{c2}. In other words, the temperature dependence of the magnetic moment is entirely determined by the temperature dependence of H_{c2}. This offers the possibility to obtain the normalized temperature dependence of H_{c2} by scaling the $M(H)$ curves measured at different temperatures without any *a priori* assumption for $f(H/H_{c2})$. We have applied this approach to numerous data from magnetization measurements on high-T_c superconductors which are available in the literature. Part of the results is presented in Figure 4.6. Quite surprisingly, the normalized curves of $H_{c2}(t)$ ($t = T/T_c$) turned out to be identical for all families of high-T_c materials. We note that the temperature dependencies of H_{c2} for high-T_c superconductors, obtained as a result of our analysis, are qualitatively very similar to those of conventional superconductors.

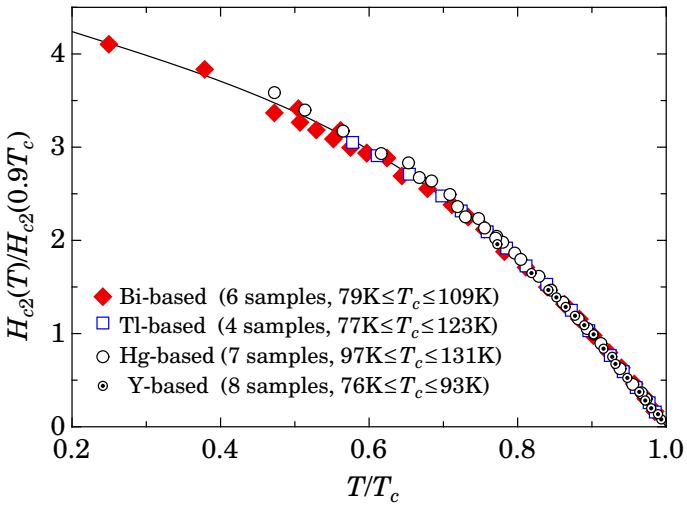

Figure 4.6: The normalized dependence of H_{c2} on T/T_c for different high T_c superconductors. For clarity, only a selection of all available data points is displayed.

4.3 Structural and physical properties of quasicrystals

4.3.1 Structural phase transitions in decagonal Al-Co-Ni quasicrystals

C. Soltmann, C. Beeli in collaboration with R. Lučk, Max-Planck-Institut fuï Metallforschung, Stuttgart, Germany

The experimental work aimed at confirming and extending former investigations on the phase transitions in Ni-rich decagonal Al-Co-Ni quasicrystals, and at providing new microscopic structural data on these materials. From earlier studies, including our own work, it is known that the low-temperature phase, the so-called type I superstructure, transforms by an order-disorder phase transition to the S1 superstructure. At even higher temperatures, the S1 decagonal superstructure transforms to the basic decagonal structure. At both phase transitions, former dilatometric data indicated a starting and end temperature of the phase transitions.

In-situ high-temperature synchrotron measurements were carried out on a polygrain sample of $Al_{71.2}Co_{12.8}Ni_{16}$ sealed into quartz capillaries. The two cell parameters were precisely determined at various temperatures. The measurements confirmed the phase transition temperatures measured by dilatometry. They also indicated that the thermal behaviour is more complex than what was known from former experiments, especially at temperatures between 400 and 700 °C. The slopes of the cell parameters (quasilattice parameter a and periodic cell parameter c) vs. temperature were found

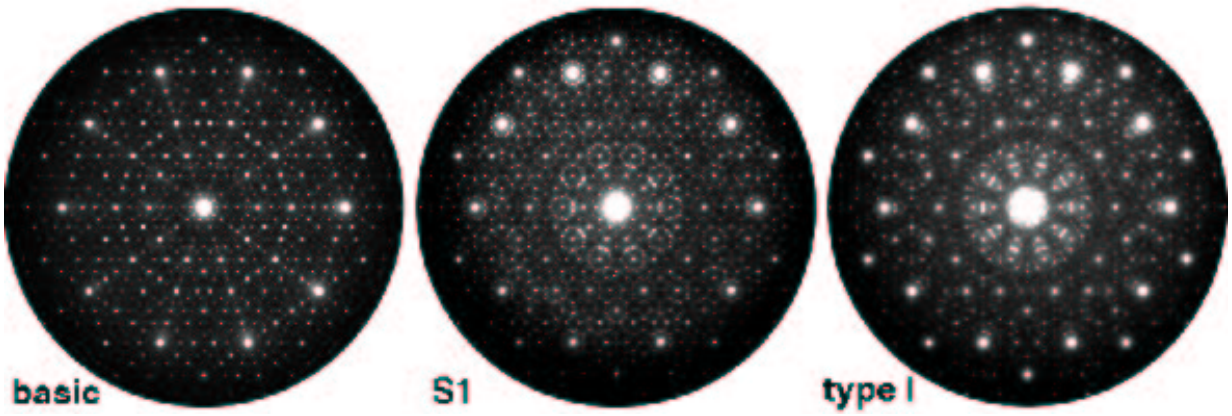

Figure 4.7: Selected area electron diffraction patterns of the three phase modifications in Ni-rich Al-Co-Ni quasicrystals.

to change discontinuously at 735 °C, and continuously at 775 °C. The first temperature is interpreted as the onset of the I-to-S1 phase transition, while the second one marks the end of the phase transition. Our new data set clarified that the I-to-S1 phase transition is a reversible second order (or higher order) phase transition, since a coexsistence of two phases has not been observed. However, the nature of the transition state between the two phase transition temperatures requires further experiments.

4.3.2 Inhomogeneous magnetism in decagonal $Al_{69.8}Pd_{12.1}Mn_{18.1}$

D. Rau,J. Gavilano,Sh.Mushkolaj,C.Beeli, and H.R. Ott

Quasicrystalline structures are characterised by a high degree of atomic order, but a lack of translational periodicity. This complicates the understanding of the electronic structure and hence of some important physical properties, such as their magnetic features. In recent years, several studies of the d-electron magnetism of Mn in icosahedral samples of Al-Pd-Mn have been motivated by the early discovery of the stable icosahedral i-Al-Pd-Mn phase. In spite of a variety of magnetic properties, depending strongly on the stoichiometric composition, all members of the Al-Pd-Mn family seem to exhibit the common feature of only a small fraction of the manganese ions carrying a magnetic moment [1,2]. In some cases this fraction even seems to decrease with decreasing temperature [2]. Theoretical studies and band-structure calculations aimed at explaining the phenomenon that only a fraction of the Mn ions carries a magnetic moment [3], and related it to the Hume-Rothery type pseudo gap in the electronic spectrum around the Fermi level.

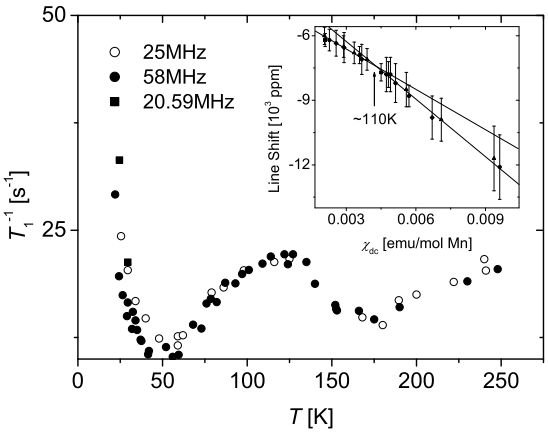

Figure 4.8: Spin-lattice relaxation rate $T_1^{-1}(T)$ for line I. The inset shows the line shift of line II plotted versus the temperature.

We measured the dc magnetic susceptibility, the ^{27}Al- and ^{55}Mn-NMR spectra, and the ^{27}Al spin-lattice relaxation rate in the decagonal quasicrystal d-$Al_{69.8}Pd_{12.1}Mn_{18.1}$. The temperature-variation of the magnetic susceptibility $\chi(T)$ and the ^{55}Mn NMR spectra reveal that only 45% of the Mn ions carry an average magnetic moment of approximately $3\mu_B$. These moments experience an average antiferromagnetic interaction, leading to a spin-glass freezing at $T_f \approx 12$K.

The ^{27}Al NMR spectra reveal two partially resolved lines. Line II is clearly much more influenced by the Mn-magnetism. We resolved the two lines by using their different spin-spin relaxation rates. We argue that the two lines are due to Al on sites in environments favoring the formation of a magnetic moment on the Mn ions (line II) and to Al in environments, where the Mn moments are quenched(line I).

Various features, such as a broad maximum in $T_1^{-1}(T)$ and a slope change in the line-shift vs. χ plot, both around 120K, suggest a gradual reduction of the number of the Mn moments with decreasing temperature, below 120K (see figure). A similar reduction of moments has been observed at lower temperatures in i-Al-Pd-Mn with a much smaller density of magnetic Mn moments[**?**].

We have not yet found an unequivocal interpretation for the broad maximum of T_1^{-1} at 120K. The same process that leads to that maximum seems to lead to a reduction of the fraction of Mn-ions that carry a magnetic moment. Neither a structural transition nor a significant change in the electronic density of states is indicated by SAED and transport measurements, respectively.

[1] M. A. Chernikov et al., Phys. Rev. B **48** (1993).

[2] J. L. Gavilano et al., Phys. Rev. B **65**, 214202 (2002).

[3] Guy Trambly de Laissardiere and Didier Mayou, Mat. Sci. Eng. **294-** **296**,621 (2000)

4.4 Physics of low-dimensional systems

4.4.1 A low-dimensional spin $S = 1/2$ system at the quantum critical limit: $Na_2V_3O_7$

J. L. Gavilano, D. Rau,S. Mushkolaj, H. R. Ott

In collaboration with P. Millet (CEMES, Toulouse), and F. Mila (University of Lausanne)

We have extended our previous measurements [1] of the physical properties of $Na_2V_3O_7$ to include magnetization, dc-susceptibility and NMR at various applied magnetic fields and very low temperatures. $Na_2V_3O_7$ is an interesting material because it may be considered to represent the physical realization of a peculiar ladder system with a periodic boundary condition in the rung direction.

Our results for the magnetization and dc-susceptibility confirmed our previous conjecture that, upon decreasing the temperature below 100 K, the number of V magnetic moments is reduced by almost an order of magnitude.

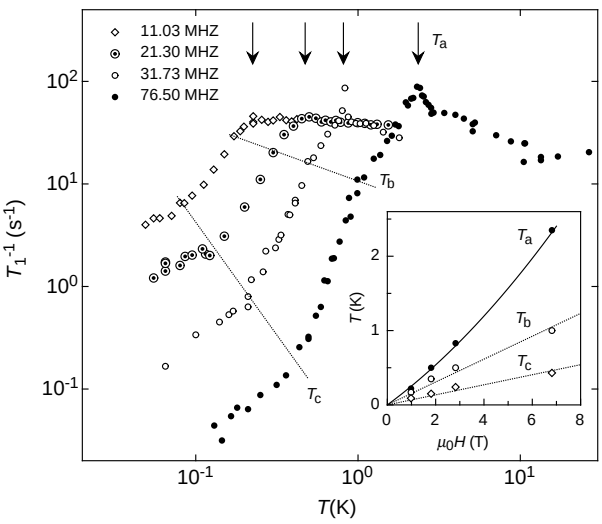

Figure 4.9: $T_1^{-1}(T)$ measured at various applied magnetic fields. Anomalies in $T_1^{-1}(T)$ are emphasized by arrows, T_a, and by two lines, T_b and T_c. Inset: Magnetic field dependence of T_a, T_b and T_c.

The ^{23}Na-NMR response of $Na_2V_3O_7$ is very peculiar. Below 30 K the NMR linewidth increases gradually with decreasing temperature by more than one order of magnitude, reaching an enhanced constant value as the temperature is reduced to below 1 K. This type of behavior usually reflects magnetic-ordering or spin-freezing phenomena. In our case, the NMR linewidth at low temperatures increases with increasing applied field, not consistent with either a simple ferro- or antiferromagnetic order.

Anomalies in the temperature dependence of the spin-lattice relaxation rate $T_1^{-1}(T)$ reveal that in the presence of modest external magnetic fields, a phase transition occurs at a field-dependent transition temperature T_a. In the ordered phase, a tiny gap forms at temperatures distinctly below T_a. In addition T_a and all the anomalies in $T_1^{-1}(T)$ shift towards $T = 0$ K with decreasing external field H. We therefore conclude that $Na_2V_3O_7$ may be considered as being very close to or at a quantum critical point at $H = 0$.

[1] J.L. Gavilano et al., Physica B, **312-313**, 622 (2002).

4.4.2 Universal behavior of spin-mediated energy transport in $S = 1/2$ chain cuprates

A.V. Sologubenko, H.R. Ott

Considerable research activity has recently been devoted to the transport properties of one-dimensional spin $S = 1/2$ systems. Theoretical work concentrated mostly on intrinsic properties of ideal systems, although transport properties of real spin-chain materials are largely determined by the influence of external perturbations. In this work we investigated experimentally the energy transport relaxation in $BaCu_2Si_2O_7$ a typical physical realisation of an isotropic 1D Heisenberg $S = 1/2$ model.

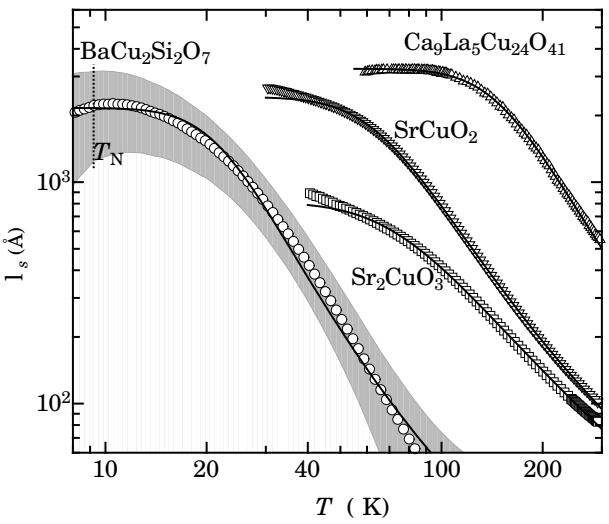

Figure 4.10: Mean free path of spin excitations in $BaCu_2Si_2O_7$ in comparison with corresponding data for the spin-chain compounds Sr_2CuO_3 and $SrCuO_2$, and the two-leg spin-ladder material $Ca_9La_5Cu_{24}O_{41}$.

The thermal conductivity $\kappa(T)$ was measured on single-crystalline samples of the $S = 1/2$ chain compound $BaCu_2Si_2O_7$ with the heat flux oriented either along or perpendicular to the chain direction. From the analysis of the anisotropy of the heat transport, the spin contribution $\kappa_s(T)$ along the chains was extracted in the temperature region between 9 and 80 K. From the values of $\kappa_s(T)$, we calculated the mean free path of the fermionic spin excitations (spinons) $\ell_s(T)$. The resulting values of $\ell_s(T)$ are shown in Fig. 4.10. The shaded area denotes the uncertainty range. In Fig. 4.10, available data for other $S = 1/2$ chain and ladder compounds are shown for comparison. It is remarkable that all $\ell_s(T)$ curves in fig. 4.10 reveal a similar trend, in particular the low-temperature saturation value is always of the order of 10^3 Å. Also the high temperature features are similar and reveal a power law type T^{-n} behavior with $n > 1$. It is important that, in spite of very different excitation spectra for spin chains and spin ladders, the corresponding extrinsic parameter $\ell_s(T)$ exhibits similar

features in both cases. This suggests that the relaxation mechanisms for spin excitations are the same in all these compounds.

The data for all compounds shown in Fig. 4.10 can be approximated (see solid lines in Fig. 4.10) using a phenomenological equation for the spinon mean free path $\ell_s^{-1}(T) = \ell_{sp}^{-1}T + \ell_{sd}^{-1}$, where the first temperature-dependent term on the right-hand side reflects the scattering of spinons by phonons, and the second and constant term is associated with the influence of magnetic defects due to non $S = 1/2$ ions on the Cu sites. Although this equation obviously captures the main features of the temperature variation $\ell_s(T)$, a rigorous quantum mechanical analysis of the influence of the spin-lattice interaction and various defects on the energy relaxation in quantum spin chains ought to be made.

4.5 Electron holography

4.5.1 Electron holography investigations on gas-phase condensed Fe nanoparticles

S. Signoretti, C. Beeli; in collaboration with E. Bonetti, L. Del Bianco, L. Pasquini and G. Matteucci, Department of Physics, University of Bologna, Italy; as well as S.-H. Liou, Department of Physics and Astronomy, University of Nebraska Lincoln, USA

We have investigated by electron holography the magnetic properties at room temperature of Fe nanoparticles prepared by Inert Gas Condensation. Samples with different mean particle size D (from 10 to 70 nm) and different Fe to oxide ratios were analyzed by complementary X-ray diffraction and conventional transmission electron microscopy. The particles adopt a core-shell structure, in which the oxide shell has a thickness of about 3 nm, independently of the core size. Electron holography experiments were made at room temperature with a Philips Tecnai F30 electron microscope, equipped with a magnetic field free Lorentz lens.

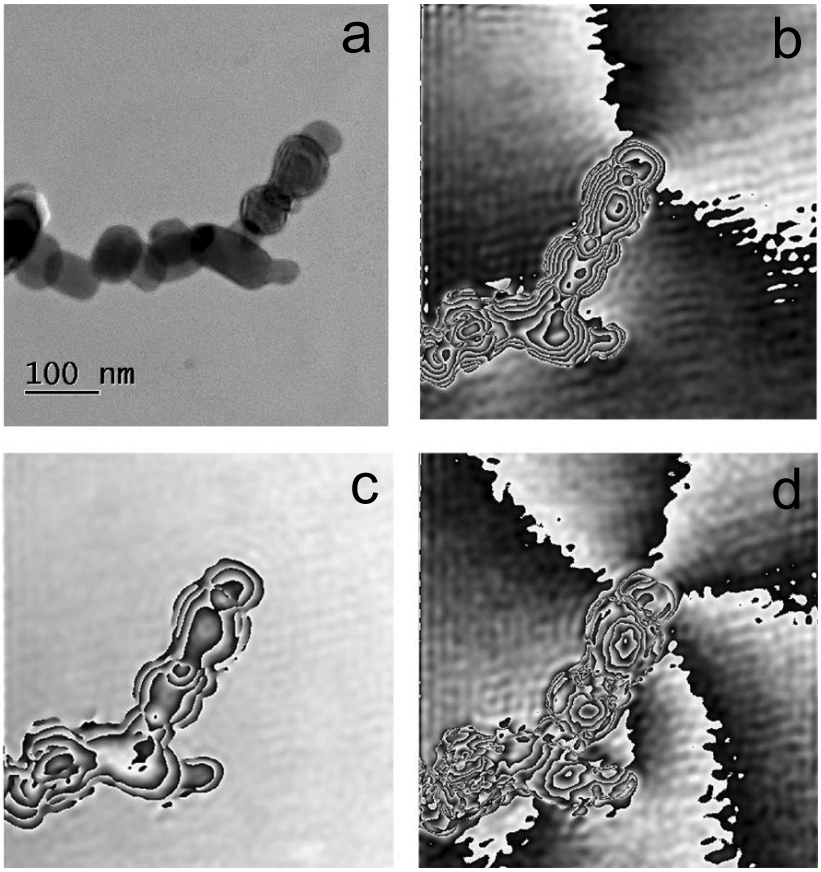

Figure 4.11: (a) TEM bright field image of a selected chain of Fe nanoparticles; (b) phase contour map (modulo $2\pi/4$); (c) phase map of thickness variations (modulo $2\pi/2$); (d) magnetic phase map (modulo $2\pi/8$).

Some results are presented in Figure 4.11. The image 4.11b represents the reconstructed phase map of the long chain of Figure 4.11a. By recording two holograms of the same chain, the second one after reversing the sample up side-down by 180 °, we can separate the thickness information (electrostatic potential) and the magnetic information (c and d respectively). The alternating black and white fringes leaking out of the sample in fig d are interpreted as the magnetic flux lines emerging from the sample. The magnetization pattern inside the chain appears extremely complex, probably because of the presence of overlapping regions between adjacent particles. Nevertheless, in some localized regions circular configurations of the flux lines are clearly visible. Such a magnetic configuration is consistent with a curling or vortex state. From the leakage flux alone we can estimate the magnetization, which is 40% of the saturation magnetization of bulk iron. This result is consistent with our assumption of a vortex-state configuration inside the particles, in which most of the stray field energy is saved at the expense of the exchange energy [Phys. Rev. B. 66, 174418 (2002)].

4.6 Morphologies of complex structures

H. Singer, I. Stalder, O. Wittwer, and J. Bilgram

4.6.1 Morphologies

We can induce different morphologies by disturbing the growing crystal. We have developed techniques to characterize the arising morphologies not only quantitatively (rough classification into dendritic, seaweed and doublon growth) but also quantitatively by the angular distribution of contour segments and morphological skeletonization of extracted contours. By means of these tools it is possible to investigate the transitions into different morphological classes.

4.6.2 Phase Field Simulations

In order to relate the results of our experiments with theoretical models we have performed numerical phase field simulations. With this method it is possible to investigate the behaviour of the solid liquid interface for different undercoolings and anisotropies of surface tensions. It is possible to reproduce qualitatively the same morphologies that we have found in our experiments. So far our simulations are performed in two dimensions, however 3D simulations, although very cost intensive in terms of computer power are in progress. Results of phase field simulations are shown in Figure 4.12.

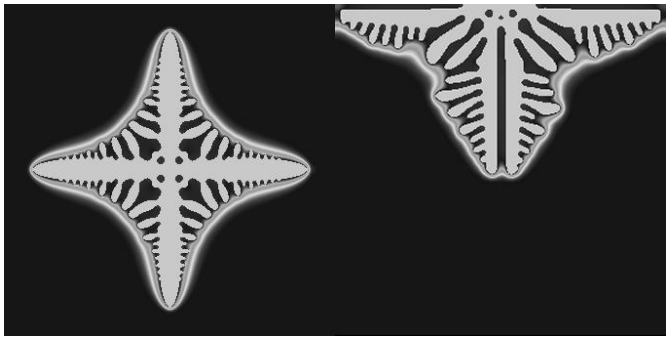

Figure 4.12: Simulation of a dendritic and a doublon structure (phase field - light gray) and superimposed the temperature field for non solid parts

4.6.3 3D Reconstruction

We investigate the growth of solidifying xenon into its undercooled melt. These experiments are three dimensional and we observe *in situ* growing crystals. We have developed sophisticated image processing algorithms to quantitatively reconstruct the three-dimensional shape of a xenon dendrite. From these reconstructions we can prove that the development of the fourfold symmetrical fins is an inherent structure formation process. A reconstructed 3D dendrite, based on experimental data, is shown in Figure 4.13.

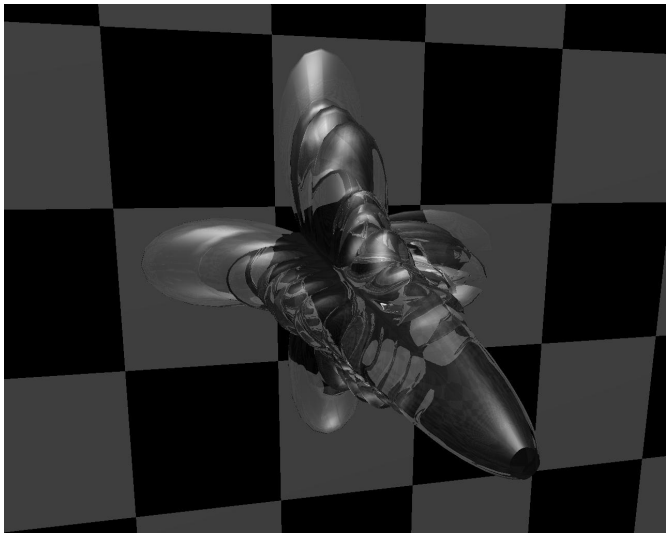

Figure 4.13: Reconstructed 3D dendrite

4.6.4 Dendrite Tip Velocity

We have performed Fourier transforms of tip velocities to investigate whether the formation of sidebranches might influence the tip velocity. No influence of sidebranches on tip velocity can be detected in Fourier transforms. An amplitude of possible tip oscillations has been estimated. Under the assumption that a possible tip oscillation only produces frequencies below 0.01 Hz (max. expected sidebranch developing rate of the investigated dendrite), the amplitude of this oscillation was determined to be less than 1.5% of v_{tip}. We have determined tip velocities during transitions from dendrite to doublon. Doublons are found to grow faster than dendrites. This seems to be in agreement with analytical results of E. Brener. Investigations of tip

velocities of growing doublon shaped crystals show an universal behaviour during tip splitting. This process consists of two phases: In a first phase, velocity decreases, then shortly after tip splitting has occurred, velocity increases to a higher value than the growth rate of an stationary growing dendrite.

4.7 Application-oriented thin film research

4.7.1 Epitaxial IV-VI narrow gap semiconductor layers for infrared devices

K. Alchalabi, K. Kellermann, D. Zimin, A.N. Tiwari and H. Zogg; www.tfp.ethz.ch

We investigate narrow gap lead chalcogenide layers like PbX, $Pb_{1-x}Sn_xX$ and $Pb_{1-x}Eu_xX$ (X=Te, Se) for applications and basic research. The layers are grown by solid source molecular beam epitaxy (MBE) onto Si(111) substrates, employing a CaF_2 buffer layer. The density of threading dislocations in these lattice- and thermal expansion mismatched layers ranges from 10^6 cm^{-2} to 10^8 cm^{-2}. Despite of these dislocation densities, devices with reasonable performances were fabricated:

- Two-dimensional Infrared Focal Plane Arrays (2d IR-FPA) have been realized on active Si-substrates containing the read-out and addressing electronics. The arrays contain 96 x 128 pixels on a 75 μm pitch and are sensitive in the 3-5 μm wavelength range. The noise current densities are dictated by the number of threading dislocations crossing the IR-active areas.

- Optically pumped mid-IR light emitters (3-6 μm wavelength range) were fabricated. As pump sources, we employed commercial low-cost high power diode lasers emitting at 0.9 μm. The structures consist of PbSe or PbTe quantum wells (QW) embedded in $Pb_{1-x}Eu_xX$ (X=Se,Te) cladding layers.

  For edge emitting lasers, the mirror facets are either cleaved (for (100) oriented IV-VI layers) or ion-milled (for (111) orientation, the natural cleavage plane for IV-VIs is (100)). Using pump sources with up to 10 W_{peak} input power, we presently obtain lasing at 4 μm wavelength up to 240K.

  For vertical emitting IR-light sources, we grow resonant cavities for wavelengths around 4 μm with Bragg mirrors on the top and bottom side. They are illuminated from the top with a 0.9 μm pump diode-laser, and emit the 4 μm light through the Si-substrate. The structures correspond to VCSELs (vertical cavity surface emitting lasers) operated at sub-threshold, the line-width is given by the quality of the cavity.

- The size distribution of self assembled PbSe quantum dots (QD) on PbTe(111) layers (grown on Si(111)) substrates can be as low as 2%. Such narrow size distributions have not been observed in any other QD system. The result is explained by non-overlapping diffusion radii for most of the dots and their nucleation occurring mainly at defects (glide steps of the quasi substrate), conditions which are not met by self-assembled quantum-dot structures in other material systems (see PRL 90, 026104, 2003).

4.7.2 Compound semiconductor thin film solar cells

M. Kaelin, D. Rudmann, D.L. Bätzner, A. Romeo, F. Kurdesau, P. K. Srivastava, F.-J. Haug, D. Abou-Ras, H. Zogg, A. N. Tiwari; www.tfp.ethz.ch

Solar cells based on polycrystalline $Cu(In,Ga)Se_2$ (called CIGS) and CdTe thin absorber layers are important for terrestrial and space applications because of the high conversion efficiency, the long term stable performance, and the high potential for clean, safe, abundant and economical generation of electricity. Thin film solar cells are grown, in

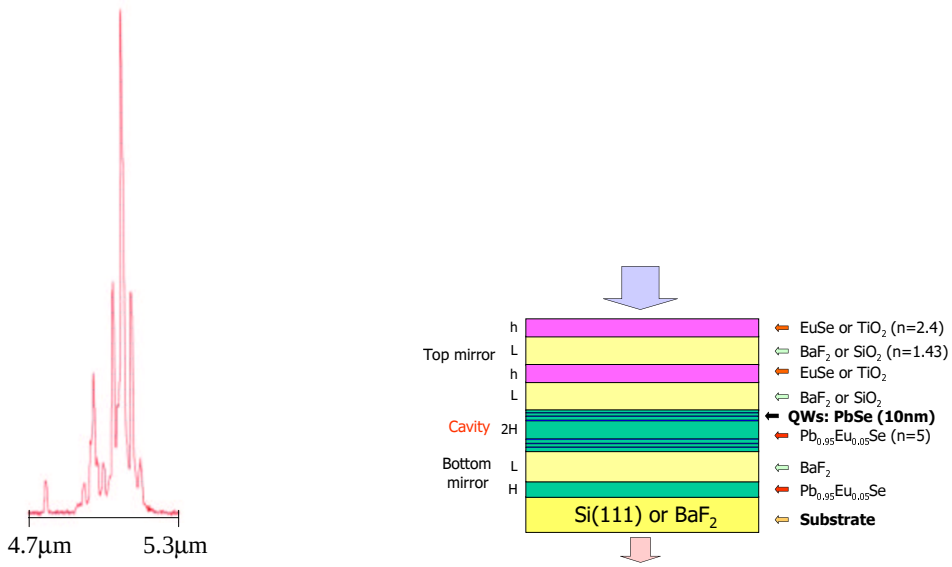

Figure 4.14: Spectrum of a multimode edge emitting MIR-laser, and structure of a resonant cavity device.

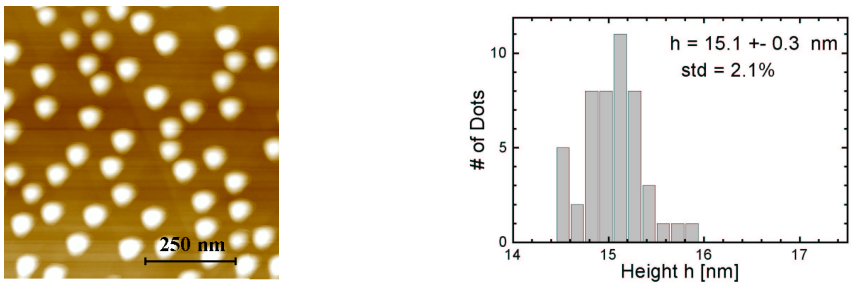

Figure 4.15: AFM image of self assembled PbSe QD and corresponding size distribution. Width is as low as 2.1%.

the form of a multi-layer stack of various materials, on a glass substrate or on a polymer film for flexible solar cells. We have developed different type of solar cells and characterized their material and device properties.

The efficiency of CIGS solar cells, consisting of ZnO:Al/ZnO/CdS/CIGS/Mo/Glass substrate in a ”substrate configuration”, was enhanced to 15.9% because of an optimization of the 3-stage growth process of the CIGS layer. The electronic properties of CIGS layers and solar cells depend on the Na-concentration and microstructure of the layer, which are influenced by deposition temperature and availability of Na during the growth (Fig. 4.16). A new method for controlled incorporation of Na was developed (applied for a patent) which is interesting for the development of flexible solar cells on polymer films. The efficiency of solar cells grown at a low deposition temperature of (450°C), on a barrier coated glass substrate, increased from 10.4% to 14.4% with this procedure.

The photovoltaic properties of CIGS solar cells depend on the properties and deposition methods of n-type wide bandgap buffer layers. The efficiency of solar cells with chemical bath deposited CdS is 13-14% while vacuum evaporated CdS cells have an efficiency of 10-11% in those specific experiments. The efficiency of solar cells with alternative buffer layers of evaporated ZnS and ZnSe are about 8.5% after light soaking. For the development of ”superstrate” and ”semi-transparent” solar cells, CIGS layers were grown on different transparent conducting oxide layers. The electronic transport mechanism and the role of band-offsets were investigated with temperature dependent I-V measurements.

We have been developing a low cost non-vacuum process for the growth of thin CIGS layers using nano-sized precursor layers. XRD measurements have confirmed a complete selenization of the precursor layer and 4% efficiency solar cells have been fabricated.

CdTe solar cells developed in our laboratory were irradiated with electrons and protons of different energies and fluences. The photovoltaic performance data was evaluated using the displacement damage dose formalism that allowed a quantitative comparison of the cell efficiency vs. the damage dose (Fig. 4.17). The radiation tolerance of CdTe solar cells is superior to Si and III-V solar cells. Voltage dependent quantum efficiency measurements provide insights on the effects caused by diffusion of impurities across the front p-n heterojunction and CdTe-metal back contact. A model, based on a light modulated barrier in CdS, is developed to explain the results.

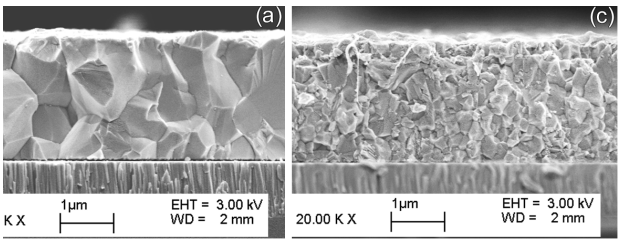

Figure 4.16: SEM of CIGS without (a) and with Na (c).

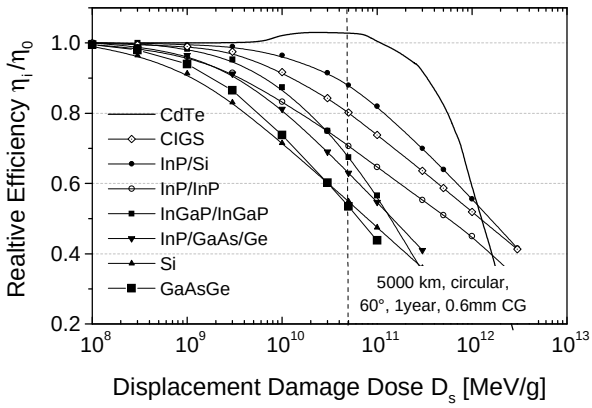

Figure 4.17: Efficiency vs. displacement damage dose comparison of different cells.

Chapter 5

Magnetism, Electron Spectroscopy

Head
Prof. Dr. D.Pescia

Academic Staff
Prof. Dr. M. Erbudak
Dr. A. Vaterlaus
Dr. U. Ramsperger
M. Buess (Ph.D student)
T. Flückiger (Ph.D. student)
R. Lüscher (Ph.D. student)
O.Portmann (Ph.D. student)

technical staff
K. Brunner
U. Maier (part time)
L. Scherrer (part time)

Academic Guest
Th. Schöb (January-March 2002)

5.1 Magnetism

5.1.1 The stripe phase of ultrathin Fe films imaged with SEMPA

O. Portmann, A. Vaterlaus, U. Maier, D.Pescia

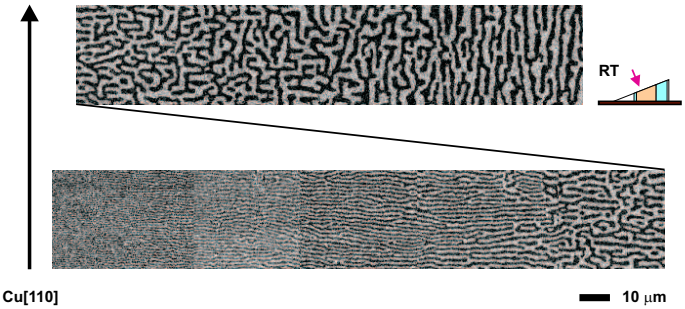

Figure 5.1: The image covers the magnetic domain patterns present in a wedge at room temperature. The film thickness decreases from right to left. Because of the thickness dependence of T_c, the effective temperature of the film **increases** from right to left, i.e. the film is brought closer to the phase transition when moving from right to left on the wedge. The stripes to the left of the labyrinth are perpendicular to the step edges that run from top to bottom. The image was taken at room temperature.

We have explored the evolution of the stripe pattern in perpendicularly magnetized ultrathin films as a function of their thickenss. For this purpose, we have prepared wedges of Fe films on Cu(100). Wedges are created by moving a shutter in front of the substrate during the evaporation process. The figure shows the sequence of phases measured on a wedge-like film at room temperature using SEMPA microscopy (Scanning Electron Micoscopy with Polarisation Analysis). The contrast is due to magnetic domains with opposite **perpendicular** magnetization. In proceeding toward the phase transition (i.e. form right to left in the figure), we measure a sequence of phases which geos beyond the stripe phase encountered at low temperatures and predicted for the ground state. In fact, we see that the low temperature stripe phase (right) transforms into a labyrinthine phase when the phase transition is approached. Closer to the transition, we observe a most peculiar and yet unexplained **re-entrance** of the stripe phase, before the paramagnetic state sets in (left in the bottom figure, where the contrast is almost vanishing). This sequence of phases has not yet been predicted, and is still under close investigation.

5.1.2 The stripe phase of ultrathin Fe films imaged at Swiss Light Source

A. Vaterlaus, Ch. Quitmann (SLS)

During an extended pilot experiment at the Surfaces - Interfaces Microscopy (SIM) beamline of the Swiss Light Source (SLS) we tried to image the magnetic domain pattern of thin Fe layers grown on Cu(001) with the Photoemission Microscope by using the X-ray circular magnetic dichroism effect (XMCD-PEEM) (R. Nakajima, J. Sthr, Y.U. Idzerda, Phys. Rev. B 59, 6421 (1999). The aim was to follow the magnetic domain pattern while approaching the Curie temperature. Fe grown on Cu(001) is magnetized perpendicularly to the plane of the layer. In this state, there are two competing interactions (dipolar- and exchange-) which induce a stripe domain pattern. When approaching the Curie temperature this stripe pattern should loose its order by following an universal succession of different patterns. This purely geometrical phase transition should have been investigated by imaging a wedge of Fe on Cu(001). Since Fe on Cu(001) is extremely sensitive to any contamination during evaporation we succeeded to produce only one sample (see the figure) with perpendicular magnetization. The figure shows a XMCD-PEEM image of the onset of magnetic order on a Fe wedge grown on Cu(001). The picture was collected during the above mentioned pilot experiment. The Fe coverage increases along the vertical axis of the image. Fe grown on Cu(001) looses its magnetic order at room temperature if its thickness exceeds 3 atomic layers (AL). Therefore the upper part of the image appears gray. This corresponds to no magnetic signal and therefore to paramagnetic iron. Some stripe domains are visible for a coverage below 3 AL and at some locations the stripe width widens up (as expected) further away from the phase transition line (horizontal). However, the expected succession of patterns could not be observed.

5.1.3 XYZ-Fine Positioning and Scanning Stage for Photoemission Microscope

U. Maier and A. Vaterlaus

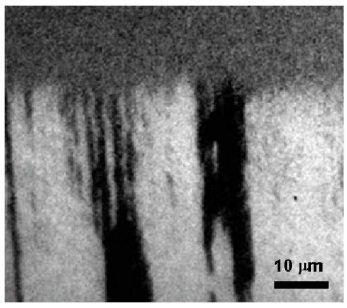

Figure 5.2: PEEM difference image of a wedge of Fe on Cu(001). The Fe coverage increases along the vertical axis of the image and the magnetic order is lost at room temperature for a coverage exceeding ≈ 3.0 ML. The thickness variation from bottom to top is about 0.24 ML. The image was collected at room temperature using a photon energy of 708.5 eV, a picture collected with right hand circular polarized light was subtracted from an image collected with left hand circular polarized light.

For the advanced photoemission beamline (APE) at ELETTRA a special positioning and scanning stage was developed. To achieve a lateral resolution of 100nm a Fresnell lens and Order Shield Aperture (OSA) have to be accurately positioned in the center of the light beam (140-1500eV). For image acquisition the lens and OSA can be scanned with a 2x1/2" EBL-3 Piezo tube scanner.

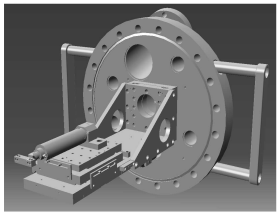

Figure 5.3: Advanced Photoemission Experiment (APE) at ELETTRA: scanning and positioningstage for Fresnel-lens

5.2 Electron Spectroscopy

5.2.1 Electronic excitations and lack of magnetic ordering in the icosahedral quasicrystal $Al_{70}Pd_{20}Mn_{10}$

T. Flückiger, R. Lüscher, and M. Erbudak in collaboration with A. R. Kortan of OFS Laboratories, Bell Labs.

In the search for the electronic origin of the peculiar magnetic behavior of the $Al_{70}Pd_{20}Mn_{10}$ quasicrystal, we have performed electron energy-loss spectroscopy measurements on a surface, oriented perpendicular to one of the threefold-symmetry directions of this icosahedral alloy. Two different surface structures, a cubic and a quasicrystalline surface phase, are induced by Ar^+ ion bombardment and annealing on the same bulk quasicrystal. Comparative measurements on these surfaces indicate that the $3p - 3d$ transition in the quasicrystal is so weak that it is reasonable to assume that quenching of the magnetic moments at almost all Mn sites in the quasicrystal occurs as a result of the filling of the $3d$ band. This is in agreement with the spectroscopic observations on the pentagonal surface where by virtue of its increased occupancy, the Mn $3d$ band moves away from E_F and leads to a lowering in the density of states at the Mn site, which has been termed as pseudo gap in quasicrystals. It has been known that the density of states at E_F is lower for the well-prepared pentagonal surface of the icosahedral phase. This lowering is then a consequence of the energy shift of the partial density of the Mn $3d$ states away from E_F compared to the other structural modifications on the quasicrystalline bulk alloy. As a results, XPS spectra from Mn core levels show enhanced line-shape asymmetry in the cubic surface structure in contrast to the quasicrystalline surface phase.

5.2.2 Debye temperature of the pentagonal surface of the icosahedral quasicrystal $Al_{70}Pd_{20}Mn_{10}$

R. Lüscher, T. Flückiger, and M. Erbudak

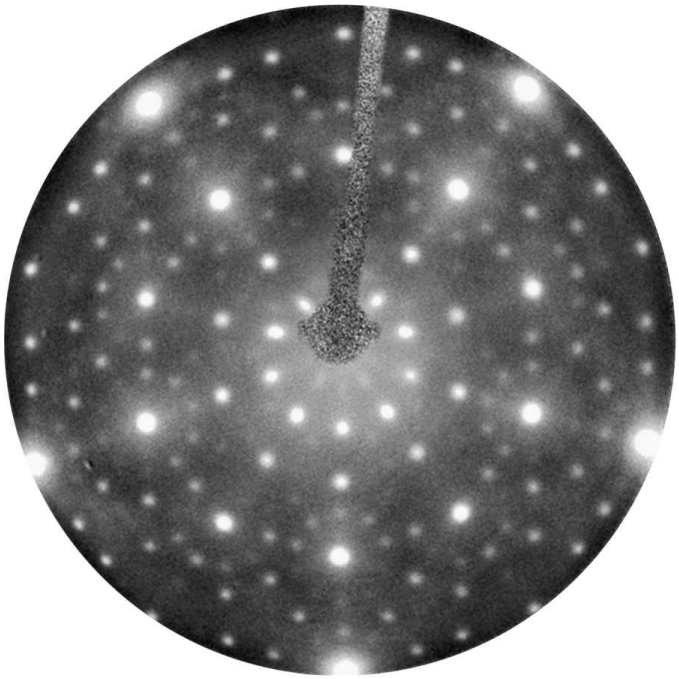

Figure 5.4: Low energy electron-diffraction pattern obtained at the pentagonal surface of Al-Pd-Mn recorded at 52 eV electron energy and near-normal incidence. The pattern serves as a probe for the quality of the surface structure.

The temperature dependence of the specular-beam intensity in low-energy electron diffraction is determined at the fivefold-symmetry surface of the icosahedral quasicrystal Al-Pd-Mn. The logarithm of the relative intensity is linear in temperature up to 570 K, suggesting the applicability of the standard Debye theory also to quasicrystalline surfaces. First, the temperature dependence of the Bragg-peak energy is measured by recording I-V spectra at different temperatures. The resulting shift to lower energies is accounted for mainly by the lattice expansion perpendicular to the surface. A value of about 1 eV is found in the temperature range considered here and included in the analysis. Indirectly, this argumentation supports the structural model of quasicrystals with a structure, which consists of planes rather than clusters. As a result of several measurements, a Debye temperature of 298 ± 7 K is found at 43 eV beam energy. This quantity is a measure for the atomic mean-square vibrational amplitude $\langle u^2 \rangle$ normal to the surface. The value associated with the pentagonal surface is very close to the bulk value of 312 K, determined in x-ray diffraction. It is common that the Debye temperature of the surface is 1.5 – 2 times lower than the corresponding bulk value. In the present case, however, $\theta_{\mathrm{D}}^{\mathrm{surface}}$ has a similar value as $\theta_{\mathrm{D}}^{\mathrm{bulk}}$. This implies that the quasicrystalline bulk closely resembles the surface from the point of view how the vibrational modes are developed. This conclusion can be reconciled with a bulk Al-Pd-Mn which is unusually rich in vacancies.

5.2.3 Structural transitions at the surface of the decagonal quasicrystal $Al_{70}Co_{15}Ni_{15}$

T. Flückiger, T. Michlmayr, C. Biely, R. Lüscher, and M. Erbudak

$Al_{70}Co_{15}Ni_{15}$ (Al-Co-Ni) is a decagonal quasicrystal. The structure of this type of quasicrystal consists of periodically stacked planes. On these planes, atoms have an aperiodic distribution with an overall tenfold symmetry. Hence, the axis normal to these planes is called the tenfold direction. The twofold-symmetry direction is perpendicular to the tenfold direction and corresponds to either a 2P axis or a 2D axis. We have performed structural and chemical investigations on the twofold-symmetry surface in real time using secondary-electron imaging (SEI) and Auger electron spectroscopy (AES), respectively. We have found that Ar-ion bombardment of an Al-Ni-Co surface results in depletion of Al due to preferential sputtering. As a consequence, a surface alloy in body-centered cubic structure (the B2 phase) develops. Annealing at 400 K stabilizes this cubic surface phase with a composition of $Al_{57}Co_{24}Ni_{19}$. The lower limit of the thickness of the surface region with a crystalline structure on the quasicrystalline bulk material is about 2 nm, which is given by the depth of sensitivity of the SEI technique. At higher annealing temperatures, Al concentration increases at the surface until the surface structure transforms back to quasicrystalline at around 650 K. We note that the replenishment of Al is limited by diffusion of Al from the bulk to the surface. Therefore, the temperature required for the formation (restoration) of the quasicrystalline phase is equal to or lower than 650 K. In this process, the bulk material acts chemically as an Al reservoir and crystallographically as a structural template on which the quasicrystalline phase is reassembled. For conventional crystals the epitaxial growth of different structures

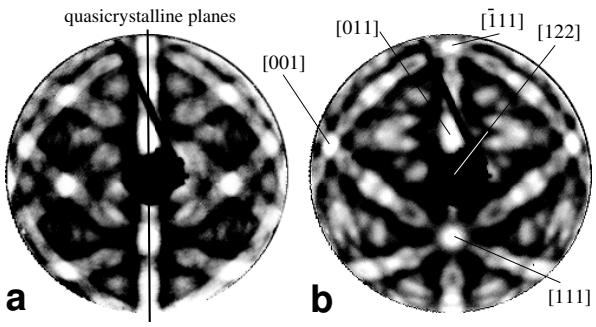

Figure 5.5: SEI patterns of a) the twofold-symmetry direction of the quasicrystalline phase and b) the cubic phase with the (122) orientation induced by sputtering the surface with Ar ions at 300 K.

assumes the coincidence (or almost coincidence) between some lattice spacings in the growing film and the substrate. In quasicrystals there is no periodicity at all but there are strong Fourier harmonics of the atomic density which means that there are corresponding lattice spacings. Hence we can suppose that the epitaxial growth of crystals on quasicrystalline substrates occurs in such a way that strong Fourier harmonics of both structures coincide in orientations and lattice spacings. Small mismatches can be accommodated via the strain relaxation or via chemical relaxation, i.e., the crystal grows with such a chemical composition, which corresponds to minimum structural mismatch. We determine the symmetry elements in the structure of both the well-ordered quasicrystalline Al-Co-Ni surface and the cubic phase in order to assess how the two unequal structures fit together. The SEI pattern from the quasicrystal displays bright spots and bright bands of enhanced electron intensity. These show twofold symmetry, as expected. There is a bright band in the middle of the pattern corresponding to dense atomic layers normal to the tenfold-symmetry axis. We distinguish additional bright patches on this band resulting from dense atomic rows along the 2P and 2D axes, also arranged in tenfold symmetry. The analogues SEI pattern from the B2 phase contains a bright band, too, corresponding to crystalline (011) planes. On this band we distinguish [111], [122], and [011] directions, with [122] coinciding with the surface normal. The direction perpendicular to the bright band is [011], which is parallel to the tenfold-symmetry axis of the quasicrystal. The angular difference between the crystalline and quasicrystalline features is 0.74° (35.26 - 36°) which is difficult to detect in SEI.

5.2.4 Structure of Gd_2O_3 films on GaAs(100) and GaN(0001)

T. Flückiger, Y. Weisskopf, R. Lüscher, and M. Erbudak in collaboration with M. Hong and A. R. Kortan of OFS Laboratories, Bell Labs.

Atomically thin films of Gd_2O_3, heteroepitaxially grown on III-V semiconductor surfaces by electron-beam evaporation, find novel applications in electronic device industry owing to their unprecedented properties as surface-passivation layers. It was found that Gd_2O_3 grows on GaAs(100) in the bcc-derived α-Mn_2O_3 structure exposing its (110) surface. Here, we report that the structure of the 2.5-nm thick film disorders upon mild sputtering with 1000 eV-Ar+ ions for 10 s. Subsequent annealing of the sample at about 700 K restores the crystalline structure, however, displaying fourfold-symmetry. Analysis of core-level shifts determined by x-ray photoemission spectroscopy shows that the chemical state of all four components change upon sputtering and change further upon annealing. This indicates that sputtering breaks all chemical bonds and destroys the Gd_2O_3-GaAs interface; annealing restores a partially different chemical state of the atoms in a near-surface region signalling some degree of intermixing of the atomic components. Gd_2O_3 films grown on GaN(111), on the other hand, are stabilized by the substrate in the high-temperature hexagonal phase exposing thereby their sixfold-symmetric surface. Patterns recorded during sequential sputtering reveal that there exists a high degree of rotational alignment of crystallographic features at the Gd_2O_3-GaN interface even though there is a large lattice mismatch between the film and the substrate.

Chapter 6

Publikationen

Y. Acremann, A. Kashuba, M. Buess, D. Pescia, C.H. Back
Magnetic spatial non-uniformities on the picosecond timescale
Mat. J.Magn. Magn., 293, 346-350 (2002)

G. Agostinelli, D.L. Bätzner, M. Burgelman
An alternative model for V, G and T dependence of CdTe solar cells IV characteristics
Conference Record of the 29th IEEE Photovoltaic Specialist Conference, New Orleans 744-747 (2002)

H. Anderhub, D. Baetzner, S. Baumgartner, A. Biland, C. Camps, M. Capell, V. Commichau, L. Djambazov, Y.-J. Fanchiang, G. Fluegge
The Prototype Synchrotron Radiation Detector (PSRD)
Nuclear Instruments and Methods in Physics Research Section A 478 1-2 123-124, (2002)

M. Angst, R. Puzniak, A. Wisniewski, J. Jun, S.M. Kazakov, J. Karpinski, J. Roos, H. Keller
Temperature and Field Dependence of the Anisotropy of MgB_2
Phys, Rev.Lett. **88** 167004 (2002)

M. Angst, S.M. Kazakov, J. Karpinski, A. Wisniewski, R. Puzniak, M. Baran
Critical currents and order-disorder phase transition in the vortex states of$YBa_2Cu_4O_8$ with chemically introduced disorder
Phys. Rev.B **65**, 094518/1-11 (2002)

D.L. Bätzner, A. Romeo, M. Döbeli, K. Weinert, H. Zogg, A.N. Tiwari
High energy irradiation properties of CdTe/CdS Solar cells
Conference Record of the 29th IEEE Photovoltaic Specialist Conference, New Orleans 982-985 (2002)

R. Bilyalov, C.S. Solanki, J. Poortmans, O. Richard, H. Bender, M. Kummer, and H. von Känel
Crystalline silicon thin films with porous Si backside reflector
Thin Solid Films 403-404, 170 (2002)

R. Bilyalov, C.S. Solanki, J. Poortmans, O. Richard, M. Kummer, and H. von Känel
Crystalline silicon thin films with porous Si backside reflector
Solar Energy Materials and Solar Cells **72**, 221 (2002)

E. Bonetti, L. Del Bianco, L. Pasquini, G. Matteucci, C. Beeli, and S. Signoretti
Electron holography investigation of nanocrystalline iron particles
Physica Status Solidi (a) **180**, 459 (2002)

Ch. Bosshard, R. Spreiter, L. Degiorgi and P. Günter
Infrared and Raman spectroscopy of the organic crystal DAST:Polarization dependence and contribution of molecular vibrations to the linear electro-optic effect
Phys. Rev. **B66**, 205107 (2002)

S. Broderick, B. Ruzicka, L. Degiorgi, H.R. Ott, J.L. Sarrao and Z. Fisk
Scaling between magnetization and Drude weight in EuB_6
Phys. Rev. **B65**, 121102(R) (2002)

S. Broderick, L. Degiorgi, H.R. Ott, J.L. Sarrao, and Z. Fisk
Giant magneto-optical response of ferromagnetic EuB_6
Eur. Phys. J. B **27**, 3-6 (2002)

M. Chiao, C. Pfleiderer, S.R. Julian, G.G. Lonzarich, R.S. Perry, A.P. Mackenzie, and Y. Maeno
Effect of pressure on metamagnetic $Sr_3Ru_2O_7$
Physica B **312-313**, 698 (2002)

L. Degiorgi, S. Broderick, H.R. Ott, J.L. Sarrao and Z. Fisk
The ferromagnetic phase transition in EuB_6: optical evidence for quasiparticle undressing
Physica **B312-313**, 327 (2002)

L. Del Bianco, D. Foriani, A.M. Testa, E. Bonetti, and S. Signoretti
Magneto-thermal behavior of nanoscale Fe/FeOxide granular system
Phys. Rev. B **66**: 174418 (2002)

L. Diehl, G. Dehlinger, H. Sigg, U. Gennser, D. Grützmacher, E. Müller, J. Faist, K. Ensslin, I. Sagnes, Y. Campidelli, O. Kermarrec, and D. Bensahel
Intersubband quantum cascades in the Si /SiGe material system
Physica E **13**, 829 (2002)

S.V. Dordevic, D.N. Basov, A. Slebarski, M.B. Maple and L. Degiorgi
Electronic structure and charge dynamics of the Heusler alloy Fe_2TiSn probed by infrared and optical spectroscopy
Phys. Rev. **B66**, 075122 (2002)

A. Dorn, A. Fuhrer, M. Sigrist, T. Ihn, T. Heinzel, K. Ensslin, W. Wegscheider, and M. Bichler
Electronic properties of antidot lattices fabricated by atomic force lithography
Appl. Phys. Lett. **80**, 252 (2002)/ cond-mat/0108520

A. Dorn, A. Fuhrer, T. Ihn, T. Heinzel, K. Ensslin, W. Wegscheider, and M. Bichler
Magnetotransport through AFM-defined antidot arrays
Physica E **13**, 719 (2002)

D. Dvorsek, V. Kabanov, J. Demsar, J. Karpinski, S.M. Kazakov, D. Mihailivic
Femtosecond quasiparticle relaxation dynamics and probe polarization anisotropy in $Y(Ba_{1-x}Sr_x)_2Cu_4O_8$
Phys. Rev.B **66**, 020510 (2002)

M.R. Eskildsen, M. Kugler, S. Tanaka, J. Jun, S.M. Kazakov, J. Karpinski, O. Fischer
Vortex Imaging in the pi-Band of Magnesium Diboride
Physical Review Letters **89** 187003 (2002)

Z. Fisk, H.R. Ott, V. Barzykin, L.P. Gor'kov
The emerging picture of ferromagnetism in the divalent hexaborides
Physica B **312-313**, 808-810 (2002)

T. Flückiger, M. Erbudak, A. Hensch, Y. Weisskopf, M. Hong, A.R. Kortan
Structure of Gd_203 films epitaxially grown on GaAs (100) and GaN(0001) surfaces
Anal. Surf. Inter., 34, 441 (2002)

A. Fuhrer, A. Dorn, S. Lüscher, T. Heinzel, K. Ensslin, W. Wegscheider, and M. Bichler
Electronic Properties of nanostructures defined in Ga[Al]As heterostructures by local oxidation
Invited Review article, Superl. & Microstr. **31**, 19 (2002)

Fuhrer A. , S. Lüscher, T. Ihn, T. Heinzel, K. Ensslin, W. Wegscheider, and M. Bichler
Energy spectra of quantum rings
Microelectr. Eng. **63**, 47 (2002)

J.L. Gavilano, D. Rau, Sh. Mushkolaj, H.R. Ott, J. Dolinsek, K. Urban
Anomalous NMR response of quasicrystalline icosahedral $Al_{72.4}Pd_{20.5}Mn_{7.1}$ at low temperatures
Phys. Rev. B **65**, 214202 (2002)

J.L. Gavilano, D. Rau, Sh. Mushkolaj, H.R. Ott, P. Millet, F. Mila
DC-susceptibility and NMR response of a low-dimensional quantum magnet: $Na_2V_3O_7$
Physica B **312-313**, 622-623 (2002)

J.L. Gavilano, Sh. Mushkolaj, D. Rau, H.R. Ott, A. Bianchi, D.P. Young, Z. Fisk
^{11}B-NMR in $CaBa_6$
Physica B **312-313**, 813-814 (2002)

K. Giannò, A.V. Sologubenko, H.R. Ott, A.D. Bianchi and Z. Fisk
Low-temperature thermoelectric power of CaB_6
J. Phys.: Condens. Matter **14**, 1035-1043 (2002)

R.S. Gonnelli, D. Daghero, G.A. Ummarino, V.A. Stepanov, J. Jun, S.M. Kazakov, J. Karpinski
Direct evidence of two-band superconductivity in MgB_2 single crystals by by directional point-contact spectroscopy in magnetic field
Physical Review Letters **89** 247004 (2002)

O. Grimm, H. Anderhub, J.R. Bates, D. Bätzner, S. Baumgartner, A. Biland, C. Camps, M. Capell, V. Commichau, L. Djambazov, Y.-J. Fanchiang
Design and construction of the prototype synchrotron radiation detector
Nuclear Instruments and Methods in Physics Research Section A 491 (1-2) 98-112, (2002)

F.-J. Haug, H. Zogg, A. N. Tiwari
11% efficiency CIGS superstrate solar cells without sodium precursor
Proc. 29th IEEE Photovoltaic Specialist Conference, New Orleans, USA, 728-731, (2002)

T. Heinzel, R. Jäggi, M. v. Waldkirch, E. Ribeiro, K. Ensslin, S.E. Ulloa, G. Medeiros-Ribeiro, and P. M. Petroff

Transport signatures for correlated disorder in self-ordering of self-assembled InAs quantum dots on GaAs
Physica **E** 12, 591 (2002)

Z. Hu, S.-L. Drechsler, J. MaIek, H. Rosner, R. Neudert, M. Knupfer, M.S. Golden, J. Fink, J. Karpinski, G. Kaindl, C. Hellwig, Ch. Jung
Doped holes in edge-shared CuO_2 chains and the dynamic spectral weight transfer in X-ray absorption spectroscopy
Europhysics Letters **59** (1), 135-141 (2002)

T. Ihn, J. Rychen, K. Ensslin, W. Wegscheider, and M. Bichler
Tunneling between edge channels in the quantum Hall regime manipulated with a a scanning force microscope
Microelectr. Eng. **63**, 81 (2002)

T. Ihn, J. Rychen, T. Cilento, R. Held, K. Ensslin, W. Wegscheider, and M. Bichler
Scanning gate measurements on a quantum wire
Physica **E** 12, 691 (2002)

T. Ihn, J. Rychen, T. Vancura, T. Cilento, R. Held, K. Ensslin, W. Wegscheider, and M. Bichler
Local spectroscopy of edge channels in the quantum Hall regime with local probe techniques
Physica E **13**, 671 (2002)

M. Krisch, R.A. Brand, M. Chernikov and H.R. Ott
Phonons in the icosahedral i-AlPdMn studied by inelastic X-ray scattering
Phys. Rev. B. **65**, 134201 (2002)

M. Kummer, C. Rosenblad, A. Dommann, T. Hackbarth, G. Höck, M. Zeuner, E. Müller, and H. von Känel
Low energy plasma enhanced chemical vapor deposition
Mat. Sci. Eng. B **89**, 288 (2002)

Landau I.L. and H.R. Ott
Model of the mixed state of type-II superconductors in high magnetic fields
J. Phys.: Condens. Matter **14**, L313-L318 (2002)

Landau I.L. and H.R. Ott
Temperature dependence of the upper critical field of type-II superconductors from isothermal magnetization data: Application to high-temperature superconductors
Phys. Rev. B **66**, 144506 (2002)

I.L. Landau, H.R. Ott
Vortex motion in high-temperature superconductors
Phys. Rev. B **65**, 064511 (2002)

S. Lindemann, T. Ihn, S. Bieri, T. Heinzel, K. Ensslin, G. Hackenbroich, K. Maranowski, and A. C. Gossard
Bouncing states in quantum dots
Phys. Rev. B **66**, 161312 (2002)

S. Lindemann, T. Ihn, T. Heinzel, W. Zwerger, K. Ensslin, K. Maranowski, and A. C. Gossard
Stability of spin states in quantum dots
Phys. Rev. B **66**, 195314 (2002)

S. Lindemann, M. Bänninger, T. Ihn, T. Heinzel, S. E. Ulloa, K. Ensslin, K. Maranowski, and A. C. Gossard
Lateral superlattices on parabolic quantum wells
Phys. Rev. B **66**, 165317 (2002)

S. Lindemann, T. Ihn, T. Heinzel, K. Ensslin, K. Maranowski, and A. C. Gossard
From two-dimensional to three-dimensional quantum dots
Physica E **13**, 638 (2002)

S. Lüscher, A. Fuhrer, R. Held, T. Heinzel, K. Ensslin, W. Wegscheider, and M. Bichler
Quantum wires and quantum dots defined by lithography with an atomic force microscope
Microelec. Journal **33**, 319 (2002)

T. Mack, T. Hackbarth, U. Seiler, H.-J. Herzog, H. von Känel, M. Kummer, J. Ramm, and R. Sauer
Si/SiGe FETs grown by MBE on a LEPECVD frown virtual substrate
Mat. Sci. Eng. B **89**, 368 (2002)

M. Mali, J. Roos, H, Keller, J. Karpinski und K. Conder
Oxygen isotope effect of the plane-copper NQR frequency in $YBa_2Cu_4O_8$
Phys.Rev. B **65** (18) 184518 (2002)

F. Marabelli, A. Rastelli, A. Valsesia, and H. von Känel
Opitcal characterization of self-assembled Ge dots on silicon
Mat. Res. Soc. Symp. Proc. 696, N7.5.1 (2002)

A.V. Mironov, S.M. Kazakov, J. Jun, J. Karpinski
$MgNB_9$, new magnesium nitroboride
Acta Cryst. C **58** (2002)

A. NabiaIek, B. Kundys, Yu. Bukhantsev, S. Visiliev, A. Wisniewski, J. Jun, S.M. Kazakov, J. Karpinski, H. Szymczak
Magnetostriction in superconducting MgB_2
Physica B **319** 286-292 (2002)

M.K.K Nakaema, M.J.S.P Brasil, F. Iikawa, E. Ribeiro, T. Heinzel, K. Ensslin, G. Medeiros-Ribeiro, P.M. Petroff and J.A Brum
Micro-photoluminescence of self-assembled quantum dots in the presence of an electron gas
Physica E **12**, 872 (2002)

Ott H.R.
Ferromagnetic metals, an old problem revisited
Physica B **318**, 77-81 (2002)

L. Perfetti, S. Mitrovic, G. Margaritondo, M. Grioni, L. Forro, L. Degiorgi and H. Hoechst
Mobile small polarons and the Peierls transition in the quasi-one-dimensional conductor $K_{0.3}MoO_3$
Phys. Rev. **B66**, 075107 (2002)

G.K. Perkins, J. Moore, Y. Boguslavski, L.F. Cohen, J. Jun, S.M. Kazakov, J. Karpinski, A.D. Caplin
Superconducting critical fields and anisotropy of a MgB_2 single crystal
Techn. Sup. Sci., 15 1156 (2002)

A. Perucchi, L. Degiorgi, J. Jun, M. Angst, J. Karpinski
Magneto-optical reflectivity of superconducting MgB_2 single crystals
Phys.Rev.Lett. **89** 097001 (2002)

K. Przybilla, W. Berkhahn, H. Burtscher, D. Dahmann, U. Matter, P. Rietschel
Monitoring diesel particulates in working areas with photoelectric aerosol sensor
Gefahrstoffe-Reinhaltung der Luft, **62**, 279-284 (2002)

K. Przybilla, Z. Qian, U. Matter, H. Burtscher
Ultarfine particle emissions of residential oilburners: Influence of burner type, fuel, and additives
Combustion Science and Technology **174**, 49-66 (2002)

P. Raiteri, D.B. Migas, L. Miglio, A. Rastelli, and H. von Känel
Critical role of the surface reconstruction in the stability of (105) Ge pyramids on Si(001)
Phys. Rev. Lett. **88**, 256103 (2002)

A. Rastelli, E. Müller, and H. von Känel
Shape preservation of Ge/Si(001) islands during Si-capping
Appl. Phys. Lett. **80**, 1438 (2002)

A. Rastelli, M. Kummer, and H. von Känel
Shape evolution of Ge domes on Si(001) during Si capping
Physica E **13**, 1008 (2002)

A. Rastelli, M. Kummer, and H. von Känel
Shape transitions of Ge islands on Si(001)
Mat. Res. Soc. Symp. Proc. 696, N5.4.1 (2002)

A. Rastelli and H. von Känel
Surface evolution of faceted islands
Surface Science **515**, L493 (2002)

D.Rubio Temprano, J.Mesot, S.Janssen, K.Conder, A.Furrer, A.Sokolov, V.Trounov, S.M. Kazakov, J.Karpinski, H.Mutka, K.A.Müller
Isotope effects on the pseudogap in high-temperature superconductors
Appl.Phys. A 74, s1630-s1634 (2002)

L. Savini, E. Bonetti, L. Del Bianco, L. Pasquini, S. Signoretti, P. Allia, M. Coisson, J. Moya, V. Selvaggino, P. Tiberto, and F. Vinai
Observation of magnetoresistance in core-shell Fe-FeOxide systems
Journal Appl. Phys. **91**, 1806 (2002)

A. Schenck, D. Andreica, F.N. Gygax, H.R. Ott
Extreme quantum behavior of positive muons in $CeAl_2$ below 1 K
Phys. Rev. B **65**, 024444 (2002)

V. Senz, T. Ihn, T. Heinzel, K. Ensslin, G. Dehlinger, D. Grützmacher, U. Gennser, E. H. Hwang, and S. DasSarma
Comparison of experimental and calculated resistance in p-SiGe over a wide temperature range
Physica E **13**, 723 (2002)

K. Siegmann, K. Sattler, H.C. Siegmann
Cluster physics at high temperature: carbon formation in combustion
J. of El. Spectroscopy and Related Phenomena, **126**, 191 (2002)

A.V. Sologubenko, J. Jun, S.M. Kazakov, J. Karpinski, and H.R. Ott
Temperature dependence and anisotropy of the bulk upper critical field H_{c2} of MgB_2
Phys. Rev. B, **65**, 180505(R) (2002)

A.V. Sologubenko, J. Jun, S.M. Kazakov, J. Karpinski and H.R. Ott
Thermal conductivity of single crystalline MgB_2
Phys. Rev. B **66** 014504 (2002)

Ch. Soltmannm, C. Beeli, R. Lück, and P. Wägli
High-temperature powder diffraction study of reversible phase transitions in decanogal Al-Co-Ni quasicrystals
HASYLAB Annual Report (2002)

Soltmannm Ch.and C. Beeli
Analysis of the long-range order in two-dimensional non-periodic structures
ICEM-15, Durban, South Africa, 995 (2002)

U. Staub, G.I.Meijer, R.Allenspach, G.Bednorz, J.Karpinski, S.M.Kazakov, L.Paolasini, F.d'Acapito
Direct observation of charge order in $NdNiO_3$
Phys.Rev.Lett. **88**, 126402 (2002)

M. Terheggen, H. Heinrich, G. Kostorz, F.-J. Haug, H. Zogg, A.N. Tiwari
Ga2O3 Segregation in Cu(In,Ga)Se2/ZnO Superstrate Solar Cells and its Impact on their Photovoltaic Properties
Thin Solid Films 403-404 212-215 (2002)

J. Tersoff, B.J. Spencer, A. Rastelli, and H. von Känel
Barrierless formation and faceting of SiGe islands on Si(001)
Phys. Rev. Lett. **89**, 196104 (2002)

T. Uchihashi, U. Ramsperger
Electron Conduction through quasi-one-dimensional indium wires on silicon
Lett. Appl. Phys., 80, 4169 (2002)

H. Von Känel, M. Kummer, G. Isella, E. Müller, and T. Hackbarth
Very high hole mobilities in modulation-doped Ge quantum wells grown by low-energy plasma enhanced chemical vapor deposition
Appl. Phys. Lett. **80**, 2922 (2002)

P. Vonlanthen, K.B. Tanaka, A. Goto, W.G. Clark, P. Millet, J.Y. Henry, J.L. Gavilano, H.R. Ott, F. Mila, C. Berthier, M. Horvatic, Y. Tokunaga, P. Kuhns, A.P. Reyes, W.G. Moulton
High-magnetic-field NMR studies of $LiVGe_2O_6$: A quasi-one-dimensional spin S = 1 system
Phys. Rev. B **65**, 214413 (2002)

W. Weber, S. Riesen, C.H. Back, A. Shorikov, V. Anisimov, H.C. Siegmann
Spin Motion of electrons during reflection from a ferromagnetic surface
Phys. Rev. B **66**, R100405 (2002)

G.A. Wigger, Ch. Wälti, and H.R. Ott, A.D. Bianchi, and Y. Fisk
Magnetization-dependent electronic transport in Eu-based hexaborides
Phys. Rev. B **66**: 212410 (2002)

D.P. Young, Z. Fisk, J.D. Thompson, H.R. Ott, S.B. Oseroff, and R.G. Goodrich
Magnetic properties - Parasitic ferromagnetism in a hexaboride? Reply
Nature **420**, 144 (2002)

M. Zehetmayer, M. Eisterer, J. Jun, S. M. Kazakov, J. Karpinski, A. Wisniewski, and H. W. Weber
Mixed-state properties of superconducting MgB_2 single crystals
Phys.Rev.B **66**, 052505 (2002)

M. Zehetmayer. F.M. Sauerzopf, H.W. Weber, J. Karpinski, M. Murakami
Comparative study of sequentional neutron irradiation and annealing effects in superconducting $YBa_2Cu_3O_{7-x}$, $Y_2Ba_4Cu_8O_{16}$ and $NdBa_2Cu_3O_{7-x}$ single crystals
Physica C **383** (2002) 232-240

S. Zherlitsyn, B. Wolf, B. Lüthi, M. Lang, P. Hinze, E. Uhrig, W. Assmus, H.R. Ott, D.P. Young, and Z. Fisk
Elastic properties of ferromagnetic EuB_6
Eur. Phys. J. B **22**, 327-333 (2002)

D. Zimin, K. Alchalabi, H. Zogg
Heteroepitaxial PbTe-on-Si pn-junction IR-sensors: Correlations between material and device properties
Physica E **13**, pp. 1220-1223 (2002)

Chapter 7

Vorträge

(* = eingeladen)

Agostinelli G.
An alternative model for V, G and T dependence of CdTe solar cells IV characteristics
29th IEEE Photovoltaic Specialist, New Orleans, USA, 22.05.2002

Agostinelli G.
A theoretical model for the front region of CdTe solar cells
EMRS-Spring Meeting, Strasbourg, France, 19.06.2002

Alchalabi K.
Photovoltaische Bleichalkogenid-auf-Silizium Infrarotsensoren-Arrays
32. IR-Kolloquium, Freiburg i. Br., Germany, 23.04.2002

Alchalabi K.
A 2-d Monolithic PbTe-on-Active-Si Infrared Focal Plane Array for Thermal Imaging
MIOMD-V, 5th Int Conf. on Mid-Infrared Optoelectronic Materials and Devices, Annapolis MD, USA, 08.09.2002

Alchalabi K.
Optically pumped lead-chalcogenide IR-emitters
ISCS 2002, 29th International Symposium on Compound Semiconductors, Lausanne, Switzerland, 08.10.2002

Alchalabi K.
Self Assembled PbSe Quantum Dots with Almost Equal Sizes Grown by MBE on PbTe/Si(111)
MRS Fall 2002, materials research society fall meeting, Boston, USA, 03.12.2002

* Angst M.
Critical currents and order-disorder transition in the vortex states of $\mathrm{Yba}_{2-x}\mathrm{Sr}_x\mathrm{Cu}_4\mathrm{O}_8$
Workshop on Cuprate Superconductors, Physik-Institut der Universität Zürich, 06.02.2002

Angst M.
Evidence for a Temperature and Field Dependence of the Anisotropy of MgB_2
Meeting of the Swiss Physical Society, Lausanne, Switzerland, 1.3.2002

* Angst M.
The Anisotropy of MgB_2
Seminar in Festkörperphysik, Physik-Institut der Universität Zürich, 17.4.2002

* Angst M.
The Anisotropy of MgB_2
Solid State Physics Seminar, ETH, 02.05.2002

Angst M.
Disorder-induced phase transition of vortex matter in MgB_2
Boromag Workshop on Superconductivity in Magnesium Diboride and Related Materials, Genoa, Italy, 18.06.2002

* Angst M.
Anisotropy and phase diagram of MgB_2 by torque magnetometry
Seminar über Festkörperphysik, Forschungszentrum Karlsruhe und Universität Karlsruhe, Germany, 25.11.2002

* Batlogg B.
Abenteuer Zukunft- wieviel Technik braucht der Mensch?
Oberlech Seminar, Austria, 10.01.2002

* Batlogg B.
Organische Halbleiter- neue Physik und Grundlage neuer Technologien
Tag der Physik, Universität Regensburg, Germany, 08.02.2002

* Batlogg B.
Charge dynamics in organic solids
Solid State Physics Seminar, MIT, Cambridge MA, USA, 11.02.2002

* Batlogg B.
Electrons in organic molecular crystals
Physics Colloquium, Boston College, Boston, USA, 13.02.2002

* Batlogg B.
Organic molecular crystals
Harris Lecture, MIT, Cambridge MA, USA, 14.02.2002

* Batlogg B.
Electron dynamics in organic solids
Intl. Winterschool on New Developments in Solid State Physics, Mauterndorf, Austria 26.02.2002

* Batlogg B.
Superconductivity in organic materials
Tutorial Lecture, March Meeting of the Amer. Phys. Society, Indianapolis, USA, 17.03.2002

* Batlogg B.
Charge dynamics in organic molecular crystals
EOS Meeting, Engelberg, Switzerland, 25.03.2002

* Batlogg B.
Field effect in orgainc crystals
European Physical Society, Brighton, United Kingdom, 09.04.2002

* Batlogg B.
Organic molecular crystals
European COST Meeting, Brighton, United Kingdom, 11.04.2002

* Batlogg B.
Electrons in organic crystals
Kolloquium Universität Dresden, Germany, 16.04.2002

* Batlogg B.
Organic molecular crystals
Münchner Physik Kolloquium, Germany, 22.04.2002

* Batlogg B.
Organische Materialien in Wissenschaft und Technik
Festkolloquium, Universität Bayreuth, Germany, 23.04.2002

* Batlogg B.
Technology and Nanotechnology
SALSA Strategies and Advances in Atomic Level Spectroscopy and Analysis Guadeloupe, France, 05.05.2002

* Batlogg B.
Charge dynamics and phonons in organic molecular crystals
Hawaii, USA, 24.05.2002

* Batlogg B.
Electronic transport in organic materials
Seminar, Institut für Neuroinformatik, Universität Zürich, Switzerland, 14.06.2002

Batlogg B.
Plastik Elektronik
Tag der offenen Türe, Physikdepartement ETH Zürich, Schweiz, 15.06.2002

* Batlogg B.
Electron-phonon interaction in organic molecular crystals
Intl. Conf. on electron-phonon effects in nanosystems, Montauk, USA, 25.09.2002

Bätzner D.L.
High energy irradiation properties of CdTe/CdS Solar cells
29th IEEE Photovoltaic Specialist, New Orleans, USA, 22.05.2002

Bätzner D.L.
Study of spatially resolved impurity diffusion in CdTe solar cells using voltage dependent quantum efficiency measurement
EMRS-Spring Meeting, Strasbourg, France, 19.06.2002

Baumgartner A.
Tuning Fork based SPM sensors for Low Temperature Operation
NCCR-Meeting, Pontresina, Switzerland, 04.09.2002

* Beeli C.
Electron holography of magnetic structures, AML
National Inst. For Materials Science, Tsukuba, Japan, 15.02.2002

* Beeli C.
Internal surface morphology in quasicrystals and the relation to the Laplace equation
Division of Applied Physics Graduate School of Engineering, Hokkaido University, Japan, 19.02.2002

Beeli C.
Analysis of the long-range order in two-dimensional non-periodic structures
International Congress on Electron Microscopy (ICEM), Durban, South Africa, 04.09.2002

Beeli C.
Quantitative Characterization of MFM Tips by Electron Holography
International Congress on Electron Microscopy (ICEM), Durban, South Africa, 04.09.2002

* Bergemann Ch.
Metallische Oxide - Fermi-Flaechen stark korrelierter Elektronen
Physikalisches Kolloquium, Univ. des Saarlandes, Germany, 02.05.2002

* Bergemann Ch.
Fermi Surfaces of Metallic Oxides
Gruppenseminar (Abt. Keimer), MPI Stuttgart, Germany, 31.05.2002

* Bergemann Ch.
Fermi Surfaces of Metallic Oxides
Low Temperature Physics Seminar, Cavendish Laboratory, University of Cambridge, United Kingdom, 05.06.2002

* Bergemann Ch.
Fermi Surfaces of Metallic Oxides
Special Seminar, Clarendon Laboratory, University of Oxford, United Kingdom, 10.06.2002

Bergemann Ch.
The Normal State Fermi Liquid in the Unconventional SuperconductorSr_2RuO_4
International Conference on Strongly Correlated Electron Systems, Krakau, Poland 11.07.2002

* Bergemann Ch.
Fermi Surfaces of Metallic Oxides and Low-Dimensional Systems
Special Seminar, Department of Chemistry, UBC Vancouver, Canada, 11.09.2002

* Bergemann Ch.
Fermi Surfaces of Metallic Oxides
Gemeinsames Seminar des Forschungszentrums Karlsruhe und der Universität Karlsruhe über Festkörperphysik, Germany, 28.10.2002

* Bergemann Ch.
Fermi Surfaces and Electron Masses in Metallic Oxides
Seminar des SFB ”Kooperative Phänomene im Festkörper”, Universität Augsburg, Germany, 05.11.2002

* Bergemann Ch.
Fermi Surfaces and Quasiparticle Masses in Metallic Oxides
Solid State Seminar, University of St. Andrews, 04.12.2002

* Bilgram J.
Solidification far from equilibrium – morphologies of xenon crystals
MPI Komplexe Systeme, Dresden, Germany, 15.07.2002

Broderick S.
Magneto-Optics of Ferromagnet EuB_6: Giant Kerr Rotation
Summer School on Condensed Matter Research, Zuoz, Switzerland, 10.08.2002

Buess M.
Ultrafast generation of magnetic fields in a Schottky diode
ICMFS 2002, Kyoto, Japan, 07.03.02

* Buess M.
Ultrafast generation of magnetic fields in a Schottky diode
2nd Lion Symposium, PSI Villigen, Switzerland, 08.04.02

Buess M.
Ultrafast generation of magnetic fields in a Schottky diode
Intermag 2002, Amsterdam, The Netherlands, 29.04.02

* Chiao M.
Magnetism on the verge of breakdown
Seminar, Department of Materials and Metallurgy, University of Cambridge, United Kingdom, 07.03.2002

Chiao M.
Chemical and pressure tuning of magnetic order in EU_(1-x)Ca_xB_6
Strongly Correlated Electron Systems Conference, Krakow, Poland, 12.07.02

* Chiao M.
Magnetism on the verge of breakdown
Colloquium, Department of Phyics, University of British Columbia, Vancouver, Canada, 30.09.02

* Degiorgi L.
Optics in correlated systems
Colloquium at Technical University of Braunschweig, Braunschweig, Germany, 08.01.2002

* Degiorgi L.
Light and Matter
Solid State Physics Seminar at University of Neuchatel, Neuchatel, Switzerland, 14.01.2002

* Degiorgi L.
Magneto-optical study of the ferromagnet EuB_6 and the superconducting MgB_2
NEDO-Meeting, Buergenstock Lucerne, Switzerland, 30.01.2002

* Degiorgi L.
The synchrotron IR program at the SLS facility
Workshop on Synchrotron-Based Infrared and X-Ray Microscopies, Grenoble, France, 05.04.2002

Degiorgi L.
Magneto-optical study of metallic ferromagnets: the intriguing case of EuB_6
19th General Conference of the EPS Condensed Matter Division, Brighton, United Kingdom, 07.04.2002

* Degiorgi L.
Light and Matter
Solid State Physics Seminar, University of Geneva, Geneva, Switzerland, 26.04.2002

* Degiorgi L.
Optical properties of low dimensional correlated systems
International Conference on Frontiers in Condensed Matter Physics, Groningen, The Netherlands, 13.06.2002

* Degiorgi L.
Charge dynamics of carbon nanotubes
International Conference on Science and Technology of Synthetic Metals (ICSM02), Shanghai, China, 04.07.2002

* Degiorgi L.
Optics of strongly correlated systems
Workshop on Realistic Theories of Correlated Electron Materials, University of California Santa Barbara, USA, 03.09.2002

* Degiorgi L.
Optical properties of correlated systems
2nd Hvar workshop on Strongly Correlated Electrons, Hvar, Croatia, 04.10.2002

* Degiorgi L.
Ferromagnetism and superconductivity in boride systems
International Conference on the Low Energy Electrodynamics in Solids (LEES02), Montauk Long Island NY, USA, 17.10.2002

* Degiorgi L.
Light and Matter
Colloquium at University of Groningen, Groningen, The Netherlands, 28.11.2002

Dorn A.
Ballistic Electron Transport through open Squares
MQC2, Neapel, Italy, 06.06.2002

Dorn A.
Ballistic Electron Transport through open Squares
ICPS - Int. Conf. on the Physics of Semiconductors Edinburgh, Scottland, 01.08.2002

Ellenberger C.
Tunable g-Factor in Parabolic Quantum Wells
NCCR-Meeting, Pontresina, Switzerland, 04.09.2002

* Ensslin K.
Controlling charge, spin and geometry in semiconductor nanostructures
Physics colloquium, University of Linz, Austria, 10.01.2002

* Ensslin K.
Is there a metallic phase in two dimensions
Solid State Physics colloquium, University of Linz, Austria, 10.01.2002

* Ensslin K.
Semiconductor Nanostructures
Lecture series, EPFL, Lausanne, Switzerland, 01.02.2002

* Ensslin K.
Nuclear pores, quantum rings and other nanostructures
Mini-symposium “Joining Forces – New Chemistry-, Informatics- and Engineering based approaches to study biological processes, ETH Zürich, Switzerland, 22.03.2002

* Ensslin K.
Schalten mit einzelnen Elektronen
Lecture for Senioren-Universität Zürich, Switzerland, 22.05.2002

* Ensslin K.
Spin states in quantum rings
Seminar, Princeton University, USA, 24.05.2002

* Ensslin K.
Electron transport through phase-coherently coupled cavities
Workshop on the two-dimensional metal-insulator-problem, NEC Research Institute, Princeton, USA, 25.05.2002

* Ensslin K.
Spin effects in quantum rings and quantum dots
III International workshop on macroscopic quantum coherence and computing (MQC^2), Naples, Italy, 04.06.2002

* Ensslin K.
Manipulating Charge, Spin and Geometry in Semiconductor Nanostructures
XXXI International School on the Physics of Semiconducting Compounds, Jaszowiec, Poland, 12.06.2002

Ensslin K.
Elektrizität
Lecture with Experiments, Open day of the Physics Department ETH Zürich, Switzerland, 15.06.2002

* Ensslin K.
Electrical control of spin coherence in semiconductor nanostructures
International Conference on Superlattices, Nanostroctures and Nanodevices, Toulouse, France, 23.07.2002

* Ensslin K.
Spin and orbital effects in quantum rings
ERATO Workshop on Mesoscopic Correlations in Nanostructures, Delft, The Netherlands, 27.07.2002

* Ensslin K.
Energy spectra and spin states of quantum rings fabricated by AFM lithography
International Workshop on Nanostructure & Nano-electronics’02, Tsukuba, Japan, 10.09.2002

* Ensslin K.
Spin effects in quantum dots
Seminar, University of Tokyo, Japan, 12.09.2002

Ensslin K.
Spin states in quantum dots
Joint workshop on Nanoscience, NCCR – CFN (Karlsruhe), Emmendingen, Germany, 08.10.2002

* Ensslin K.
Manipulating charge and spin in semiconductor nanostructures
SFB workshop on Quantum Materials, Hamburg, Germany, 09.10.2002

* Ensslin K.
Spin Effects in Quantum Dots and Rings
Mesoscopic Electronics COST P5 Workshop,Catania, Sicily, Italy, 18.10.2002

* Ensslin K.
Orbital and Spin Effects in Quantum Rings
International Workshop on Multifunctional Materials, 29.10.2002, Pucon, Chile

* Ensslin K.
Spin effects in quantum dots
Workshop on „Electrons in zero-dimensional conductors: Beyond the single-particle picture“, Dresden, Germany, 17.11.2002

* Erbudak M.
Structural investigations using electron scattering
Seminar Yeditepe University, Istanbul, Turkey, 08.05.02

* Erbudak M.
Strukturbestimmung mittels rückgestreuter Elektronen
Physikkolloqium Universität Saarbrücken, Germany, 21.05.02

* Erbudak M.
Surface structure investigations using LEED
Chemistry Dept., UC San Diego, USA, 02.07.02

* Erbudak M.
Cynematic vs. dynamic analysis of LEED data
Chemistry Dept., UC San Diego, USA, 10.07.02

* Erbudak M
Spot profile analysis in LEED
Chemistry Dept., UC San Diego, USA, 11.07.02

Flückiger T.
Disappearance of magnetic moments in the Al-Pd-Mn quasicrystal
Annual Meeting SPS, Lausanne, Switzerland, 28.02.02

* Flückiger T.
The quasicrystal Al-Pd-Mn
Seminar EMPA Dübendorf, Switzerland, 06.06.02

Flückiger T.
Electronic structure and magnetic moments at the threefold-symmetry surface of the quasicrystal Al-Pd-Mn
NANO-7/ECOSS 21, Malmö, Sweden 28. 06. 02

Flückiger T.
Structural transitions at the surface of a decagonal quasicrystal Al-Co-Ni
ICSFS-11, Marseille, France, 12.07.02

Fuhrer A.
Energy Spectra of Quantum Rings
EPS-CMMD 2002, Brighton, United Kingdom, 09.04.2002

* Fuhrer A.
Spin Effects in Quantum Rings
PAPS Tagung Würzburg University, Würzburg, Germany, 24.07.02

Fuhrer A.
Angular Momentum and Spin Effects in Quantum Rings
ICPS - Int. Conf. on the Physics of Semiconductors Edinburgh, Scottland, 31.07.2002

* Fuhrer A.
Rings, Spins und Kondo. A quantum ring in the Coulomb Blockade regime
Seminar Max-Planck-Institut, Stuttgart, Germany, 25.11.2002

* Fuhrer A.
Rings, Spins und Kondo. A quantum ring in the Coulomb Blockade regime
Group seminar Prof. Werner Wegscheider, Regensburg University, Regensburg, Germany, 09.12.2002

* Gavilano J.
Seminar on NMR Studies of Some Hexaboride Compounds
University of Tokushima, Tokushima, Japan, 19.08.2002

Gavilano J.
11NMR studies of YB6
23er International Conference on Low Temperature Physics Hiroshima, Japan, 23.08.2002

Gavilano J.
NMR studies of N2V307
23er International Conference on Low Temperature Physics, Hiroshima, Japan, 26.08.2002

Haug F.-J.
11% efficiency CIGS superstrate solar cells without sodium precursor
29th IEEE Photovoltaic Specialist, New Orleans, USA, 22.05.2002

Haug F.-J.
Light soaking effects in CIGS superstrate solar cells
EMRS-Spring Meeting, Strasbourg, France, 19.06.2002

Hochstrasser M.
Spin Resolved Photoemission of Surface States of W(110)-(1X1)H
10th User’s Meeting at ELETTRA Trieste, Italy, 29.10.2002

* Ihn T.
Marvellous things in marvellous rings: energy spectra, spins and persistent currents
12th International Winterschool on New Developments in Solid State Physics, Low-dimensional systems: from 2D to molecules, Mauterndorf, Austria, 28.02.2002

Ihn T.
Spin states of quantum rings in the Coulomb blockade regime
15th Interational Conference on high magnetic fields in semiconductor physics, Oxford, United Kingdom, 05.08.2002

* Ihn T.
Quantum rings in the Coulomb blockade regime: a system with exceptionally transparent and well tunable properties
Workshop on Electrons in zero-dimensional conductors: beyond the single-particle picture, Max-Planck Institut, Dresden, Germany 19.11.2002

Ihn T.
Quantum ring structures: a wealth of quantum physics
Festkörperseminar der ETH Zürich, Switzerland, 19.12.2002

Kaelin M.
CIS and CIGS Layers from Selenized Nanoparticle Precursors
EMRS-Spring Meeting, Strasbourg, France, 19.06.2002

Kaelin M.
Nanomaterials for high efficiency and low cost Cu(In,Ga)Se_2 thin film solar cells
Workshop on Nanoscience, Twannberg, Switzerland, 01.10.2002

Kaelin M.
Nanopartikel für Solarzellen und optische Schichten
TopNano21 Third Annual Meeting, Kursaal Berne, Switzerland, 01.10.2002

Karpinski J.
Single crystals of MgB_2, high pressure growth and properties,
19th EPS Condensed Matter Division Brighton, United Kingdom, 07.04.2002

* Karpinski J.
MgB_2 single crystals – high pressure growth and unusual properties
INTAS Meeting, Universiteit Antwerpen, Belgium, 24.05.2002

* Karpinski J.
Unusual properties of MgB_2 single crystals
International Conference on Superconductivity, CMR & Related Materials Giens, France, 01.06.2002

* Karpinski J.
MgB_2 single crystals: unusual properties and high pressure growth
BOROMAG International workshop on superconductivity in Magnesium Diboride and related materials, 2002 Genoa, Italy, 17.06.2002

* Karpinski J.
MgB_2 Single Crystals: High Pressure Growth and Unusual Properties
Third International Workshop on Magnetism and Superconductivity of Advanced Materials, Ladek Zdroj, Poland,

14.07.2002

* Karpinski J.
High Pressure Single Crystal Growth of New Superconductor $MgB_{2,}$
40th European High-Pressure Research Group Meeting, Edinburgh, Scottland, 04.09.2002

* Karpinski J.
MgB_2 single crystals, high pressure growth and anisotropic properties
Dept. Condensed Matter Physics (DPMC), Geneva, Switzerland, 05.11.2002

Kellermann K.
Optisch gepumpte Bleichalkogenid Infrarotemitter auf Si-Substraten
32. IR-Kolloquium, Freiburg i. Br., Germany, 23.04.2002

Kellermann K.
Optically pumped lead-chalcogenide IR-emitters
MIOMD-V, 5th Int Conf. on Mid-Infrared Optoelectronic Materials and Devices, Annapolis MD, 08.09.2002

Kicin S.
Local screening and depletion behaviour of a 2-dimensional electron gas at 300 mk
12th International Winterschool on New Development in Solid State Physics, Maunterndorf, Austria, 26.02.2002

Kurdesau, F.
Chemical bath deposited CdS nanolayers for $Cu(In,Ga)Se_2$ solar cells
Workshop on Nanoscience, Twannberg, Switzerland, 01.10.2002

* Landau I.L.
Alternative approach to the vortex matter in high-Tc superconductors
Seminar Institute for Physical Problems, Russian Academy of Sciences, Moscow, Russia, 13.03.2002

* Landau I.L.
Some remarks on vortex matter in high-Tc superconductors
NATO ARW Vortex Dynamics in High Temperature Superconductors, Tashkent, Uzbekistan, 19.05.02

Lindemann S.
Spin effects in quantum dots
12th International Winterschool on New Developments in Solid State Physics, Low-dimensional systems: from 2D to molecules, Mauterndorf, Austria, 28.02.2002

Lindemann S.
Spin effects in quantum dots
ICPS - Int. Conf. on the Physics of Semiconductors Edinburgh, Scottland, 30.07.2002

Lüscher R.
Debye temperature of the pentagonal surface of the quasicrystal Al-Pd-Mn
NANO-7/ECOSS 21, Malmö, Sweden, 28. 06. 02

Lüscher R.
Hardening the quasicrystalline surface of Al-Pd-Mn by Al deposition
SSP-9, Trest Castle, Czech Republic, 06.09.02

Michlmayr T.
Structural transfromations at the surface of decagonal quasicrystal Al-Co-Ni
Annual Meeting SPS, Lausanne, Switzerland, 28.02.02

* Monnier R.
The mysterious magnetism of the divalent hexaborides
Séminaire de théorie de la matière condensée, Université de Fribourg, Switzerland, 07.06.02

* Monnier R.
The mysterious magnetism of the divalent hexaborides
Symposium in honor of the 60th Birthday of Prof. H. Eschrig, IFW Dresden, Germany, 03.07.02

* Ott H.R.
Unkonventionelle Supraleitung
Physikalisches Kolloquium Berlin, Germany, 10.01.2002

* Ott H.R.
Magnetism in Hexaborides
Seminar Cavendish Laboratory, Cambridge, United Kingdom, 14.02.2002

* Ott H.R.
New NMR results on hexaborides
NEDO workshop, Bürgenstock, Switzerland, 30.03.2003

* Ott H.R.
Thermal conductivity of single crystalline MgB2
NEDO workshop, Bürgenstock, Switzerland, 31.03.2002

* Ott H.R.
Ferromagnetism of Hexaborides
International Workshop des EU Programms FERLIN, Bled, Slovenia 24.05.2002

* Ott H.R.
Thermal Conductivity of MgB2
Seminar, Low Temperature Laboratory, HUT, Finland, 31.05.2002

* Ott H.R.
Energy transport in low dimensional spin systems
Physikalisches Kolloquium, EPFL, Switzerland, 03.06.2002

* Ott H.R.
Experimental Identification of Two-Band Superconductivity
International Workshop on Mechanisms of Superconductivity, Yalta, Ukraine, 10.09.2002

* Ott H.R.
Energy transport by spin excitations in spin chains and ladders
International Workshop, Geneva, Switzerland, 29.11.2002

Perucchi A.
Magneto-optical Reflectivity of MgB_2
International Conference on ’Frontiers in Condensed Matter Physics: Electronic Structure and Properties, Groningen,

The Netherlands, 14.06.2002

* Pescia D.
Time resolved magnetic microscopy
Annual Meeting SPS, Lausanne, Switzerland, 01.03.2002

* Pescia D.
Thin film magnetism in the picosecond time scale
March Meeting of APS, Indianapolis, USA 18.03.2002

* Pescia D.
Boundary conditions in precessional motion
Workshop, Ultrafast Phenomena by Synchrotron Radiation, Trieste, Italy, 29.10.2002

* Pescia D.
Ist Experimentalphysik noch sexy?
Diplomfeier Dept. Mathematik und Physik, ETH Zürich, Schweiz, 3.05.2002

Pescia D.
Studium und Berufsaussichten
Infotage 2002 für Maturanden und Maturandinnen, 11.9.2002

Pioda A.
Electron transport through an array of coherently coupled interacting cavities
ICPS - Int. Conf. on the Physics of Semiconductors Edinburgh, Scottland, 30.07.2002

Portmann O.
Imaging a reentrant phase transition in ultrathin films
March Meeting of APS, Indianapolis, USA, 21.03.02

Portmann O.
Imaging a Reentrant Phase Transition: Magnetic Domain Patterns in Ultrathin Fe Films on Cu(001)
Seminar at University of California, Berkeley, USA, 29.03.02

Romeo A.
Development of High Efficiency Flexible CdTe Solar Cells
PV in Europe from PV Technology to Energy Solutions, Conference and Exhibition, Palazzo dei Congressi, Rome, Italy, 08.10.2002

Rudmann D.
Effects of NaF coevaporation on structural properties of CIGS thin films
EMRS-Spring Meeting, Strasbourg, France, 19.06.2002

Senz V.
Transport through a percolation network
ICPS - Int. Conf. on the Physics of Semiconductors Edinburgh, Scottland, 30.07.2002

Signoretti S.
Electron holography of gas-phase condensed Fe nanoparticles
Summer School on Condensed Matter Research, Zuoz, Switzerland, 13.08.2002

Signoretti S.
Electron Holography of Gas-phase Condensed Fe Nanoparticles
International Workshop on Electronic Transport in Magnetic Nanogranular Systems, Torino, Italy, 27.09.2002

Signoretti S.
Seminar, Electron Holography of Magnetic Nanostructured Materials
Autumn School on Electron Microscopy, Berlin, Germany, 28.09.2002

Singer H.
Morphological Transitions of Xenon Crystals in Three Dimensions
3. Kinetik Seminar der DGKK, Dresden, Germany, 15.02.2002

Singer H.
Morphological Transitions of Xenon Crystals in Three Dimensions
Workshop on Computational Physics of Transport and Interface Dynamics, Max-Plack-Institut für Physik komplexer Systeme, Dresden, Germany,20.02.2002

Singer H.
Morphological Transitions of Xenon Crystals in Three Dimensions
DPG, Regensburg, Germany, 13.03.2002

Singer H.
Morphological Transitions of Xenon Crystals in Three Dimensions
APS Spring Meeting, Indianapolis, USA, 19.03.2002

Singer H.
Morphological Transitions of Xenon Crystals in Three Dimensions
Dynamics Days Europe 2002, Heidelberg, Germany, 17.07.2002

Singer H.
Quantitative Description of Growth Morphologies of Xenon Crystals in 3 Dimensions
ACCG-14, Seattle, USA, 08.08.2002

Singer H.
Characteristic Parameters of Xenon Dendrites
ACCG-14, Seattle, USA, 08.08.2002

Singer H.
Description Quantitative de la Morphologie de Croissance des Cristaux de Xénon en 3 Dimensions
JMC-8, Marseille, France, 29.08.2002

Singer H.
Morphological Transitions of Xenon Crystals in 3D
International Center for Mechanical Sciences CISM, Phase Change with Convection: Modelling and Validation, Udine, Italy, 04.09.2002

Sologubenko A.V.
Thermal conductivity of single crystalline MgB2: Multigap superconductivity and critical fields
The 19th General Conference of the Condensed Matter Division of the European Physical Society, Brighton, United Kingdom, 11.04.2002

Sologubenko A.V.
Anisotropy of energy transport and spin-phonon interaction in S=1/2 chain cuprate BaCu2Si2O7
The 23rd International Conference on Low Temperature Physics, Hiroshima, Japan, 26.08.2002

Sologubenko A.V.
Anomalous low-temperature thermal conductivity of MgB2
The 23rd International Conference on Low Temperature Physics, Hiroshima, Japan, 26.08.2002

Soltmann C.
Thermal expansion of decagonal Al-Co-Ni quasicrystals at higher temperatures
Hasylab annual user meeting, Hamburg, Germany, 21.01.2002

Terheggen M.
Transmission electron microscopy of diffusion induced structural and chemical changes in CdTe solar cells
EMRS-Spring Meeting, Strasbourg, France, 19.06.2002

* Tiwari A. N.
Lightweight and flexible solar cells for terrestrial and space applications
Solar Power Generation and Flexible Materials Workshop, Cambridge, United Kingdom, 21.03.2002

* Tiwari A. N.
Research and development issues in CdTe solar cells
PV-Net Workshop, Ispra, Italy, 29.05.2002

Vancura T.
Local Screening and Depletion Behaviour of a 2-Dimensional Electron Gas at 300mK
EPS-CMMD 2002, Brighton, United Kingdom, 10.04.2002

Vancura T.
Scanning Probe-Based Local Spectroscopy of Semiconductor Heterostructures Below 300mK
ICPS - Int. Conf. on the Physics of Semiconductors Edinburgh, Scottland, 30.07.2002

* Vaterlaus A.
Magnetic Imaging
Journal Club Physics Department ETH Zurich, Switzerland, 26.06.02

* Vaterlaus A.
Magnetic Nanostructures
3rd SLS User Meeting, PSI Villigen, Switzerland, 26.09.02

* Von Känel H.
Semiconductor heterostructures grown at high rates for microelectronic and photovoltaic applications
Pirelli Labs, Milano, Italy, 30.01.2002

* Von Känel H.
Epitaxial growth by low-energy plasma-enhanced chemical vapor deposition (LEPECVD)
Seminar at CSCS, Manno, Switzerland, 23.07.2002

* Von Känel H.
Shape evolution of SiGe islands on Si(001)
Seminar at Jet Propulsion Laboratory, Pasadena, USA, 17.09.2002

* Wachter P.
Die Entdeckung einer Supraflüssigkeit in kondensierter exzitonischer Phase im Festkörper
Kolloquium der 3 Berliner Universitäten (Humboldt U., Freie U., Techn. U.) und Uni Potsdam im ,,Magnus Haus“ zu Berlin, Berlin, Germany 11. 04. 2002

* Wachter P.
A superfluid in a condensed excitonic phase
Seminar für Festkörperphysik, ETH Zürich, Schweiz, 25. 04. 2002

* Wachter P.
Magnetism and electronic structure of actinide chalcogenides
European Conf. of the Physics of Magnetism, Poznan, Poland, 04. 07.2002

* Wachter P.
Magnetism and electronic structure of Pu, PuSe and PuTe
Symposium on 50th anniversary of the first 5f-electron ferromagnet discoveryTrzebiatowski Institute, Wroclaw, Poland, 06. 07. 2002

* Wachter P.
Electronic structure of PuSe
6th Prague Colloquium on f-electron systems. Prague, Czech Republic, 09. 07. 2002

* Wachter P.
A superfluid in a condensed excitonic state in intermediate valent $TmSe_{0.45}Te_{0.55}$
Int. Conf. Strongly Correlated Electron Systems SCES, Krakow, Poland, 12.07.2002

Wittwer O.
Dendrites and Seaweed of Xenon
Dynamics Days Europe 2002, Heidelberg, Germany, 16.07.2002

Zimin D.
Self assemled semiconductor IVVI quantum dots with extremely narrow size distribution,
Workshop on Nanoscience, Twannberg, Switzerland, 01.10.2002

Zimin D.
Self assembled PbSe quantum dots with almost equal sizes on PbTe/Si(111)
ISCS 2002, 29th International Symposium on Compound Semiconductors, Lausanne, Switzerland, 08.10.2002

Zogg H.
Two-dimensional monolithic lead chalcogenide infrared sensor array on silicon read-out chip
New Developments in Radiation Detectors, 9th European Symposium on Semiconductor Detectors, Schloss Elmau, Germany, 24.06.2002